

Interplay among gravitational waves, dark matter and collider signals in the singlet scalar extended type-II seesaw model

Purusottam Ghosh,^a Tathagata Ghosh^{b,c} and Subhojit Roy^{b,c}

^a*School Of Physical Sciences, Indian Association for the Cultivation of Science, 2A and 2B, Raja S.C. Mullick Road, Kolkata 700032, India*

^b*Harish-Chandra Research Institute, A CI of Homi Bhabha National Institute, Chhatnag Road, Jhansi, Prayagraj (Allahabad) 211019, India*

^c*Regional Centre for Accelerator-based Particle Physics, Harish-Chandra Research Institute, Prayagraj (Allahabad) 211019, India*

E-mail: pghoshiitg@gmail.com, tathagata@hri.res.in,
subhojitroy@hri.res.in

ABSTRACT: We study the prospect of simultaneous explanation of the dark matter (DM), neutrino mass and baryon asymmetry of the Universe puzzles in the Z_3 -symmetric complex singlet scalar extended type-II seesaw model. The complex singlet scalar plays the role of DM. Analyzing the thermal history of the model, we identify the region of the parameter space that can generate a first-order electroweak phase transition (FOEWPT) in the early Universe, and the resulting stochastic gravitational waves (GW) can be detected at future space/ground-based GW experiments. We systematically study the effect of the $SU(2)$ triplet and the dark singlet scalars in the modification of the scalar potential in favour of a FOEWPT. Light triplet-like scalars favor a FOEWPT and we focus on the region of parameter space of the type-II seesaw part of this model such that light triplet-like scalars escape the strong bounds on their masses from their canonical searches at the Large Hadron Collider (LHC). However, it is found that the LHC precision study of the Standard Model (SM) Higgs decay in the di-photon channel has already excluded most of this region of parameter space of FOEWPT caused by the alteration of the shape of the SM Higgs potential as a consequence of large interactions with the triplet sector. On the other hand, the latest spin-independent DM direct detection constraints from XENON-1T and PANDA-4T eliminate a significant amount of parameter space that changes the SM Higgs potential in favor of a FOEWPT mostly from the dark sector and it is only possible for significantly underabundant DM scenarios. We find that the absence of new physics at the HL-LHC and/or various DM experiments in future would severely limit the prospects of detecting GW at future GW experiments and exclude the possibility of electroweak baryogenesis in this model.

KEYWORDS: Beyond Standard Model, Cosmology of Theories beyond the Standard Model, Electroweak Phase transition, Gravitational wave, Dark Matter

Contents

1	Introduction	2
2	The theoretical framework	4
2.1	The Model	4
2.2	The Dark Matter	8
2.3	Study of EWPT and the production of GWs	11
2.3.1	Effective Higgs potential at finite-temperature	11
2.3.2	Production of stochastic GWs from FOPT	13
3	Theoretical and experimental constraints	17
3.1	Theoretical constraints	18
3.1.1	Vacuum stability	18
3.1.2	Perturbativity	18
3.1.3	Partial wave unitarity	18
3.2	Phenomenological constraints	19
3.2.1	Neutrino Oscillation data	19
3.2.2	Flavor constraints	20
3.2.3	Electroweak precision observables	20
3.2.4	DM constraints	21
3.2.5	LHC constraints	21
4	Choice of parameter space	24
4.1	Implications from Higgs searches	24
4.2	Implications from DM searches	25
5	Results	26
5.1	DM Parameter space	26
5.2	Implications of the triplet sector parameters on SFOEWPT	30
5.2.1	Production of GW and the interplay with LHC	33
5.2.2	Benchmark scenarios (Set-I)	35
5.3	FOPT from the dark sector	39
5.3.1	Correlations among the DM observables and a FOPT	40
5.3.2	Benchmark scenario (Set-II)	42
6	Summary and conclusion	46
A	Tree-level tadpole relations	49
B	Set of UV-finite counterterm coefficients	49

C Daisy resummation improved thermal field-dependent masses	49
D Feynman diagrams for DM annihilation	51

1 Introduction

The discovery of the Higgs Boson at the Large Hadron Collider (LHC) around 125 GeV [1, 2] was a breakthrough moment in our understanding of the laws of nature, completing the particle lists anticipated by the Standard Model (SM). However, various shortcomings coming from different experimental observations can not be explained in the SM. The nature of dark matter, the finding of matter-antimatter asymmetry and the masses of the neutrinos are the three most pressing open questions about the present-day Universe.

The SM predicts that particles and anti-particles formed in equal numbers in the early Universe would have destroyed each other without leaving any leftover matter today. In order to generate a baryon asymmetry of any model, the following three Sakharov requirements [3] need to satisfy: (i) baryon number violation (\not{B}), (ii) C and CP violations (\not{C} , \not{CP}) and (iii) departure from thermal equilibrium. The sphalerons transitions fulfil the baryon number violation requirements in the SM, whereas the electroweak interactions provide C and CP violations. The electroweak phase transition (EWPT) in the SM is a smooth cross-over type. Therefore Sakharov’s third criterion, that the system has to go out of equilibrium, is not satisfied. In addition, the quantity of C and CP -violation in the SM is insufficient to account for the observed baryon asymmetry in the Universe (BAU). Going beyond the SM (BSM), specifically, the addition of new scalars, can modify the scalar potential in such a way that a first-order electroweak phase transition (FOEWPT) can occur in the early Universe, which is one of the essential conditions to generate BAU via the electroweak baryogenesis (EWBG) mechanism [4–7].

At the same time, several astrophysical and cosmological data, including rotation curves of galaxies, bullet clusters, gravitational lensing and the anisotropy of the cosmic microwave background (CMB) [8], provide strong motivation for the presence of dark matter (DM) in the Universe. By analysing the anisotropies in the CMB data [8], WMAP [9] and PLANCK [10] experiments find that around a quarter of the Universe is composed of non-baryonic, non-luminous matter that interacts through gravity. Apart from its abundance, which is precisely measured by the PLANCK experiment to be $\Omega_{\text{DM}}h^2 = 0.120 \pm 0.001$ [10], the nature of DM and its non-gravitational interactions are still unknown to us. Depending on its interaction strength with visible sectors, DM may be formed by various mechanisms in the early Universe. Despite several null findings from various experiments, the weakly interacting massive particle (WIMP) remains one of the most popular candidates for DM due to its detection possibility in direct and indirect searches.

On the other hand, the evidence of neutrino oscillations has opened up a new era in particle physics, emphasising the necessity for a small neutrino mass and consequently offering

evidence for phenomena beyond the SM [11, 12]. Among the various extensions of SM, popular mechanisms to generate small neutrino masses are via the seesaw mechanism, such as type-I seesaw [13–15], type-II seesaw [16–23], and so on, which are the UV realizations of the dimension five Weinberg operator [24]. This article focuses on the type-II seesaw model, in which a triplet scalar(Δ) with the hypercharge $Y = 2$ is added to SM, in contrast to other seesaw models, since it permits higher Yukawa coupling concurrently with a light seesaw scale even below TeV. Neutrinos get masses after the EWSB when the neutral component of the triplet acquires an induced vacuum expectation value (v_{ev}). The model is further extended by a complex singlet (S) with a global discrete Z_3 symmetry which makes S as a stable DM particle. The interaction between the SM Higgs doublet with the complex triplet can modify the Higgs potential in such a way that a strong first-order electroweak phase transition (SFOEWPT) occurs in the early Universe and serve as a possible candidate for explaining BAU via EWBG and recently it has been studied in reference [25]. Similarly, the interaction between the complex singlet field and the SM Higgs doublet can again change the shape of the potential in favour of a SFOEWPT. Thus, such a choice of model can solve all three shortcomings mentioned above in one framework.

Note that the non-observation of DM in direct search experiments has placed a severe constraint on the simplest WIMP-like DM scenarios in which the same interaction drives the relic density and direct detection cross-section of DM. For instance, DM direct searches impose stringent limits on the parameter space of the simplest SM Higgs portal scalar DM scenario [26, 27]. However, the scenario can drastically change in the presence of new DM annihilation channels and evade those constraints. In this model, DM annihilation due to the presence of portal interaction of DM with the triplet sector and the Z_3 -symmetry induced DM semi-annihilation channel allow a significant amount of permissible parameter space for DM that satisfies the observed DM density constraint from the PLANCK experiment, the direct detection limits from XENON-1T and PANDAX-4T, and the indirect search bounds from FERMI-LAT and MAGIC. Recently, this model has been studied in the context of explaining the excess of electron-positron flux from AMS-02 [28], DAMPE [29] and Fermi-LAT [30] collaborations in reference [31].

During the first-order phase transition (FOPT) through the nucleation of bubbles could generate stochastic gravitational waves (GW) in the early Universe [32–39]. Such a GW signal can be detected in the future-proposed various ground-based and space-borne experiments, viz., LISA [40], ALIA [41], Taiji [42], TianQin [43], aLigo+ [44], Big Bang Observer (BBO) [45] and Ultimate(U)-DECIGO [46]. These studies get more attention after recent observation of GW from LIGO and VIRGO [47–50]. Note that there is no production of GW at the electroweak scale as the EWPT is of a cross-over type in the SM. Therefore, any observation of such a stochastic GW would likely provide a clue of physics beyond the SM. Thus, certain regions of the parameter space of the present model can be probed via various future GW experiments due to the production of the GW spectrum as a result of a FOEWPT in the scalar potential.

The primary purpose of this work is to study the interplay among the three sectors mentioned above, i.e. the production of gravitational waves resulting from FOEWPT, DM

and LHC physics, to probe this model. We perform a dedicated scan of the motivated region of the parameter space. We work out and incorporate all the theoretical constraints, such as boundedness of the scalar potential from below, electroweak vacuum stability at zero temperature, perturbativity, perturbative unitarity, as well as the relevant experimental constraints coming from the neutrino sector, flavor sector, electroweak precision study, dark sector and the heavy Higgs searches at the LHC. We allow minimal mixing between SM-like Higgs and the triplet-like neutral scalar to comply with the Higgs signal strength bounds. We further study the dependencies of the decay width of the SM Higgs into a photon pair on the model parameters. We then discuss the overall phenomenology of a complex scalar DM in the presence of the scalar triplet and the SM doublet and the novel effect of Z_3 -symmetry induced semi-annihilation processes. We split the study of the FOEWPT of this model into two parts. We begin by examining the favourable region of the parameter space for FOEWPT in the parameter space of the triplet sector and then go on to the dark sector. We find the correlations between the detection prospects of the produced GW at the future proposed GW detectors as a result of the FOEWPT caused by the modification of the shape of the SM Higgs potential as a consequence of large interactions of the SM Higgs doublet with the triplet sector and the precision study of SM-like Higgs boson. We also analyse the connection between a large DM direct detection spin-independent (DMDDSI) cross-section and a FOEWPT due to significant interaction between DM and the SM Higgs doublet. To illustrate such correlations, we present a few benchmark points in this work and discuss the pattern of the phase transitions in the early Universe, the detection prospects at various GW detectors, the signal-to-noise ratio (SNR) for LISA and the detection prospects at the HL-LHC and future DM direct-detection experiments.

The article is organized as follows: In section 2, we briefly discuss the theoretical framework of the model, including the interactions Lagrangian, the WIMP DM production mechanism and its possible detection prospects, the study of EWPT and the production of GW. The relevant theoretical and experimental constraints on the model parameters are summarized in section 3. The motivated region of parameter space for this study has been discussed in section 4. In section 5 we present the results of this work. Finally, summarize the outcome of our discussion in section 6. Various tadpole relations, field-dependent masses of scalar and fermionic degree of freedoms with thermal correlations (daisy coefficients) and various Feynman diagrams for DM annihilation are presented in the appendix.

2 The theoretical framework

2.1 The Model

As discussed above, despite many successes of the SM, it can not explain the smallness of neutrino masses, the observed matter-antimatter asymmetry and accommodate a particle DM candidate among other things. To address these three issues, we consider a model by introducing an additional discrete Z_3 symmetry and enlarging the particle content of the model by adding a $SU(2)_L$ scalar triplet, Δ , with hypercharge, $Y = 2$, and a complex scalar singlet, S , which transforms non-trivially under Z_3 [31]. The quantum numbers of the BSM

scalars in our model along with the SM Higgs doublet under the extended gauge group $SU(3)_C \times SU(2)_L \times U(1)_Y \times Z_3$ are tabulated in Table 1.

Fields		$\underbrace{SU(3)_C \otimes SU(2)_L \otimes U(1)_Y}_{\text{SM}} \otimes Z_3$			
Complex Scalar DM	$S = \frac{1}{\sqrt{2}}(h_s + ia_s)$	1	1	0	$e^{i\frac{2\pi}{3}}$
Scalar Triplet	$\Delta = \begin{pmatrix} \frac{\Delta^+}{\sqrt{2}} & \Delta^{++} \\ \frac{1}{\sqrt{2}}(h_t + ia_t) & -\frac{\Delta^+}{\sqrt{2}} \end{pmatrix}$	1	3	2	1
Higgs doublet	$H = \begin{pmatrix} G^+ \\ \frac{1}{\sqrt{2}}(h_d + ia_d) \end{pmatrix}$	1	2	1	1

Table 1. Charge assignments of the scalar fields in the model under the gauge group $\mathcal{G} \equiv \mathcal{G}_{\text{SM}} \otimes Z_3$ where $\mathcal{G}_{\text{SM}} \equiv SU(3)_C \otimes SU(2)_L \otimes U(1)_Y$. Hypercharge (Y) of the field is obtained by using the relation: $Q = I_3 + \frac{Y}{2}$, where I_3 is the third component of isospin and Q is the electromagnetic charge.

The part of the Lagrangian relevant for our study in this paper is given below:

$$\mathcal{L} \supset (D^\mu H)^\dagger (D_\mu H) + \text{Tr} \left[(D^\mu \Delta)^\dagger (D_\mu \Delta) \right] - V(\Delta, H) + \mathcal{L}^{\text{Yukawa}} + \mathcal{L}^{\text{DM}}, \quad (2.1)$$

where

$$\begin{aligned} D_\mu H &= \left(\partial_\mu - ig_2 \frac{\sigma^a}{2} W_\mu^a - ig_1 \frac{Y_H}{2} B_\mu \right) H, \\ D_\mu \Delta &= \partial_\mu \Delta - ig_2 \left[\frac{\sigma^a}{2} W_\mu^a, \Delta \right] - ig_1 \frac{Y_\Delta}{2} B_\mu \Delta. \end{aligned} \quad (2.2)$$

The most general scalar potential involving the SM Higgs doublet and the scalar triplet can be written as [31, 51]:

$$\begin{aligned} V(H, \Delta) &= -\mu_H^2 (H^\dagger H) + \lambda_H (H^\dagger H)^2 \\ &+ \mu_\Delta^2 \text{Tr} [\Delta^\dagger \Delta] + \lambda_1 (H^\dagger H) \text{Tr} [\Delta^\dagger \Delta] + \lambda_2 \left(\text{Tr} [\Delta^\dagger \Delta] \right)^2 \\ &+ \lambda_3 \text{Tr} \left[\left(\Delta^\dagger \Delta \right)^2 \right] + \lambda_4 \left(H^\dagger \Delta \Delta^\dagger H \right) + \left[\mu \left(H^T i \sigma^2 \Delta^\dagger H \right) + h.c. \right]. \end{aligned} \quad (2.3)$$

Please note that in the above potential $\mu_\Delta^2 > 0$ and the Higgs triplet can not trigger any spontaneous symmetry breaking (SSB). So, similar to the SM, the electroweak symmetry breaking (EWSB) happens when the doublet, H , develops a vacuum expectation value (VEV), $\langle H \rangle = v_d / \sqrt{2}$. However, the presence of the cubic term $H^T i \sigma^2 \Delta^\dagger H$ induces a non-vanishing VEV for the triplet, $\langle \Delta \rangle = v_t / \sqrt{2}$, after the EWSB. Then the scalar fields, H and Δ can be represented as:

$$H = \begin{pmatrix} G^+ \\ \frac{h_d + v_d + ia_d}{\sqrt{2}} \end{pmatrix}, \quad \Delta = \begin{pmatrix} \frac{\Delta^+}{\sqrt{2}} & \Delta^{++} \\ \frac{h_t + v_t + ia_t}{\sqrt{2}} & -\frac{\Delta^+}{\sqrt{2}} \end{pmatrix}. \quad (2.4)$$

Note that $\sqrt{v_d^2 + 2v_t^2} = v = 246$ GeV and in the alignment limit $v_t \ll v_d$. Minimizing the scalar potential at the vacuums (v_d and v_t), the bare masses of the scalar potential can be

expressed in terms of other free parameters and can obtain the following conditions:

$$\begin{aligned}\mu_H^2 &= -\frac{2M_\Delta^2 v_t^2}{v_d^2} + \frac{1}{2}v_t^2(\lambda_1 + \lambda_4) + \lambda_H v_d^2 \\ \mu_\Delta^2 &= M_\Delta^2 - v_t^2(\lambda_2 + \lambda_3) - \frac{1}{2}v_d^2(\lambda_1 + \lambda_4) \quad \text{with} \quad M_\Delta^2 = \frac{\mu v_d^2}{\sqrt{2}v_t}.\end{aligned}\quad (2.5)$$

The field composition of $V(H, \Delta)$: The two CP even states (h_d and h_t) are mixed up after the EWSB and give rise to two physical eigenstates (h^0 , H^0) under the orthogonal transformation. The physical and interaction states are related as,

$$h^0 = h_d \cos \theta_t + h_t \sin \theta_t, \quad H^0 = -h_d \sin \theta_t + h_t \cos \theta_t \quad (2.6)$$

where θ_t is the mixing angle defined by

$$\tan 2\theta_t = \frac{\sqrt{2}\mu v_d - (\lambda_1 + \lambda_4)v_d v_t}{M_\Delta^2 - \frac{1}{4}\lambda_H v_d^2 + (\lambda_2 + \lambda_3)v_t^2}. \quad (2.7)$$

The corresponding mass eigenvalues of these physical eigenstates are given by

$$\begin{aligned}m_{h^0}^2 &= (M_\Delta^2 + 2v_t^2(\lambda_2 + \lambda_3)) \sin^2 \theta_t + 2\lambda_H v_d^2 \cos^2 \theta_t - \frac{v_t \sin 2\theta_t (2M_\Delta^2 - v_d^2(\lambda_1 + \lambda_4))}{v_d} \\ m_{H^0}^2 &= (M_\Delta^2 + 2v_t^2(\lambda_2 + \lambda_3)) \cos^2 \theta_t + 2\lambda_H v_d^2 \sin^2 \theta_t + \frac{v_t \sin 2\theta_t (2M_\Delta^2 - v_d^2(\lambda_1 + \lambda_4))}{v_d}.\end{aligned}\quad (2.8)$$

With the mass hierarchy $m_{h^0} < m_{H^0}$, the lighter state, h^0 acts like the SM higgs with mass, $m_{h^0} = 125$ GeV.

Similarly, the mixing between two CP odd states (a_d , a_t) leads to one massless Goldstone mode which is associated with the gauge boson Z in the SM and one massive pseudo scalar, A^0 and its mass (m_{A^0}) is given by,

$$m_{A^0}^2 = \frac{M_\Delta^2 (4v_t^2 + v_d^2)}{v_d^2}. \quad (2.9)$$

In the singly charged scalar sector, the orthogonal rotation of G^\pm and Δ^\pm fields lead to one massless Goldstone state absorbed by the longitudinal components of the SM gauge boson W^\pm and one massive charged scalar eigenstate, H^\pm . The mass of H^\pm is given by,

$$m_{H^\pm}^2 = \frac{(2v_t^2 + v_d^2) (4M_\Delta^2 - \lambda_4 v_d^2)}{4v_d^2}. \quad (2.10)$$

The doubly charged scalar ($H^{\pm\pm} \equiv \Delta^{\pm\pm}$) mass is given by,

$$m_{H^{\pm\pm}}^2 = M_\Delta^2 - \lambda_3 v_t^2 - \frac{\lambda_4 v_d^2}{2}. \quad (2.11)$$

Therefore the scalar potential, $V(H, \Delta)$ contains seven massive physical states: two CP even states (h^0 , H^0), one CP odd state (A^0), two singly charged scalar (H^\pm) and two doubly

charged scalar ($H^{\pm\pm}$). The scalar potential, $V(H, \Delta)$ has seven independent free parameters as

$$\{M_\Delta, v_t, \lambda_H(\simeq 0.129), \lambda_1, \lambda_2, \lambda_3, \lambda_4\} \quad (2.12)$$

whereas the physical masses and mixing angle can be represented in terms of free parameters using above equations.

In the limiting case, $v_t^2/v_d^2 \ll 1$, some interesting mass relations are followed by:

$$(m_{H^{\pm\pm}}^2 - m_{H^\pm}^2) \approx -\frac{\lambda_4 v_d^2}{4}; \quad (m_{H^\pm}^2 - m_{A^0}^2) \approx -\frac{\lambda_4 v_d^2}{4}; \quad m_{H^0} \approx m_{A^0} \approx M_\Delta. \quad (2.13)$$

Depending on the sign of the quartic coupling, λ_4 , there are two types of mass hierarchy among different components of the triplet scalar:

- when λ_4 is negative: $m_{H^{\pm\pm}} > m_{H^\pm} > m_{H^0, A^0}$,
- when λ_4 is positive: $m_{H^{\pm\pm}} < m_{H^\pm} < m_{H^0, A^0}$.

In this work, we particularly focus on the first scenario where λ_4 is negative. The mass difference between $H^{\pm\pm}$ and H^\pm defined here by Δm as: $\Delta m = m_{H^{\pm\pm}} - m_{H^\pm}$.

Neutrino masses: The Yukawa Lagrangian involving the SM lepton doublets (L) and scalar triplet (Δ) to generate neutrino masses can be written as [52],

$$-\mathcal{L}^{\text{Yukawa}} = (y_L)_{\alpha\beta} \bar{L}_\alpha^c i\sigma^2 \Delta L_\beta + h.c. \quad (2.14)$$

where y_L is a 3×3 symmetric complex matrix. The heavy triplet scalar helps to generate neutrino masses via the familiar type-II seesaw mechanism. Neutrino masses are generated once the neutral triplet scalar gets induced non-zero vev v_t . The light neutrino mass in the flavor basis is given by [52]

$$(m_\nu)_{\alpha\beta} = \sqrt{2}(y_L)_{\alpha\beta} v_t, \quad (2.15)$$

where $\{\alpha, \beta\}$ be the flavour indices and m_ν be the 3×3 light neutrino mass matrix. In order to obtain the physical neutrino masses, the mass matrix, m_ν can be diagonalised using the Pontecorvo-Maki-Nakagawa-Sakata (PMNS) matrix, U_{PMNS} , as

$$U_{\text{PMNS}}^T m_\nu U_{\text{PMNS}} = \text{diag}(m_1, m_2, m_3), \quad (2.16)$$

where

$$U_{\text{PMNS}} = \begin{pmatrix} c_{12}c_{13} & s_{12}c_{13} & s_{13}e^{-i\delta} \\ -c_{23}s_{12} - s_{23}s_{13}c_{12}e^{i\delta} & c_{23}c_{12} - s_{23}s_{13}s_{12}e^{i\delta} & s_{23}c_{13} \\ s_{23}s_{12} - c_{23}s_{13}c_{12}e^{i\delta} & -s_{23}c_{12} - c_{23}s_{13}s_{12}e^{i\delta} & c_{23}c_{13} \end{pmatrix} \begin{pmatrix} 1 & 0 & 0 \\ 0 & e^{i\alpha_2} & 0 \\ 0 & 0 & e^{i\alpha_3} \end{pmatrix}. \quad (2.17)$$

m_i ($i = 1, 2, 3$) is the eigenvalue of the light neutrino mass eigenstate ν_i . Here $c_{ij} = \cos \theta_{ij}$ and $s_{ij} = \sin \theta_{ij}$ (with $i, j = 1, 2, 3$ and $i \neq j$) are three mixing angles (with $0 \leq \theta_{ij} \leq \pi/2$) in neutrino sector and δ denotes the Dirac CP-phase (with $0 \leq \delta \leq 2\pi$) responsible for CP

violation in neutrino oscillations. The parameters of neutrino oscillations are related to the mass-squared differences defined as $\Delta m_{sol}^2 \equiv \Delta m_{21}^2 = m_2^2 - m_1^2$, $\Delta m_{atm}^2 \equiv \Delta m_{31}^2 = m_3^2 - m_1^2$ for $m_3 > m_2 > m_1$ (Normal Hierarchy (NH)) and $\Delta m_{atm}^2 \equiv \Delta m_{32}^2 = m_3^2 - m_2^2$ for $m_2 > m_1 > m_3$ (Inverted Hierarchy (IH)) as well as with the three mixing angles (θ_{ij}).

The DM Lagrangian: The Z_3 symmetry invariant Lagrangian for the scalar singlet, S which act as a stable DM candidate, can be written as [31]

$$\mathcal{L}^{\text{DM}} = \frac{1}{2} |\partial_\mu S|^2 - V^{\text{DM}},$$

where V^{DM} is the scalar potential involving the DM, S . The scalar potential reads

$$\begin{aligned} V^{\text{DM}} = & \mu_S^2 |S|^2 + \lambda_S |S|^4 + \frac{\mu_3}{3!} (S^3 + S^{*3}) \\ & + \lambda_{SH} H^\dagger H (S^* S) + \lambda_{S\Delta} \text{Tr} [\Delta^\dagger \Delta] (S^* S) \quad . \end{aligned} \quad (2.18)$$

The Z_3 symmetry is intact in the dark sector at low temperatures (after EWSB). Therefore complex scalar field, S can be a stable dark matter particle under the so-called freeze-out mechanism. After EWSB the mass of the DM turns out to be:

$$m_S^2 = \mu_S^2 + \frac{1}{2} \lambda_{SH} v_d^2 + \frac{1}{2} \lambda_{S\Delta} v_t^2 \equiv m_{\text{DM}}^2 . \quad (2.19)$$

The free parameters involved in the dark sector are following

$$\{ m_S (\equiv m_{\text{DM}}), \mu_3, \lambda_{SH}, \lambda_{S\Delta}, \lambda_S \}. \quad (2.20)$$

In the following subsection, we examine in detail how the aforementioned free parameters play a role in the phenomenology of DM.

2.2 The Dark Matter

In this subsection, we discuss the phenomenology of the scalar DM of this model in the presence of the scalar triplet and the SM scalar doublet. The singlet-like DM interacts with the doublet (H) and the triplet (Δ) sectors of the model through the scalar portal interactions $\lambda_{SH} (S^* S) (H^\dagger H)$ and $\lambda_{S\Delta} (S^* S) \text{Tr} [\Delta^\dagger \Delta]$, respectively. These interactions are essential for the DM annihilation in the early Universe. At the same time, the cubic term ($\mu_3 (S^3 + S^{*3})$) in the dark scalar potential has a novel feature of DM semi-annihilation. At the early time of the Universe, DM is in thermal equilibrium with the bath particles via the portal interactions as well as the cubic interactions in the dark sector. During that period of time, the interaction rate between DM and thermal bath particles (TBPs) ($\Gamma_{\text{DM-TBP}} = n_S \langle \sigma v_{S \rightarrow \text{TBPs}} \rangle$) dominates over the Hubble expansion rate (\mathcal{H}). With the expansion of the Universe, DM freezes out from the thermal bath when $\Gamma_{\text{DM-TBP}} < \mathcal{H}$ yielding the DM density of the current Universe. This phenomenon is often referred to as the WIMP miracle [53]. In this setup, the number density of DM is mainly governed by several number changing processes which are classified as:

$$\text{DM annihilation : } (i) S S^* \rightarrow \text{SM SM}$$

$$(ii) \ S S^* \rightarrow X \ Y; \quad \{X, Y\} = \{H^0, A^0, H^\pm, H^{\pm\pm}\}$$

$$\text{DM semi-annihilation :} \quad S S \rightarrow S \ \xi; \quad \{\xi\} = \{h^0, H^0\},$$

where the Feynman diagrams of these number changing processes of DM are shown in figures 16, 17 and 18, respectively, in appendix D. The evolution of DM number density (n_S) in terms of more convenient variables, such as the co-moving number density ($Y_S = \frac{n_S}{s}$) and dimensionless parameter $x = \frac{m_S}{T}$, is described by the Boltzmann equation (BEQ) in the following form [31, 54]:

$$\begin{aligned} \frac{dY_S}{dx} = & -\frac{s \langle\sigma v\rangle_{S S \rightarrow SM \ SM}}{\mathcal{H} x} (Y_S^2 - Y_S^{eq2}) \Theta(m_S - m_{SM}) \\ & -\frac{s}{\mathcal{H} x} \sum_{X,Y} \langle\sigma v\rangle_{S S \rightarrow X \ Y} (Y_S^2 - Y_X^{eq} Y_Y^{eq}) \Theta(2m_S - m_X - m_Y) \\ & -\frac{1}{2} \frac{s \langle\sigma v\rangle_{S S \rightarrow SSM}}{\mathcal{H} x} (Y_S^2 - Y_S Y_S^{eq}) \Theta(m_S - m_{SM}). \end{aligned} \quad (2.21)$$

Depending on the mass hierarchies among the dark matter and various scalars of this model, different number changing processes start to contribute to DM number density. This fact has been illustrated in the BEQ using the theta function (Θ). The co-moving equilibrium density of i th particle is defined as: $Y_i^{eq} = \frac{45}{4\pi^4} \frac{g_i}{g_{*s}} \left(\frac{m_i}{T}\right)^2 K_2\left[\frac{m_i}{T}\right]$ where g_i is the degree of freedom of the i -th species and g_{*s} is the internal relativistic degree of freedom associated with entropy. K_2 is the modified Bessel function of the second kind. The entropy density and Hubble expansion rates are defined as: $s = g_{*s} \frac{2\pi^2}{45} T^3$ and $\mathcal{H} = \sqrt{\frac{\pi^2 g_*}{90}} \frac{1}{M_{\text{Pl}}} T^2$, respectively with $g_* = 106.7$ and $M_{\text{Pl}} = 2.4 \times 10^{18}$ GeV. $\langle\sigma v\rangle_{SS \rightarrow ij}$ is the thermal average cross-section of the corresponding number changing process: $SS \rightarrow ij$ [53]. Solving the above BEQ, today's DM relic density is given by [53],

$$\Omega_S h^2 = 2.752 \times 10^8 \left(\frac{m_S}{\text{GeV}}\right) Y_S(x \rightarrow \infty). \quad (2.22)$$

The DM abundance ($\Omega_S h^2$) followed from equations 2.21 and 2.22 depends on the following independent free parameters which are entered in thermal average cross sections:

$$\begin{aligned} \{m_S, \mu_3, \lambda_{SH}, \lambda_{S\Delta}\} & \quad \text{from dark sector,} \\ \{\lambda_1, \lambda_2, \lambda_3, \lambda_4\} & \quad \text{from scalar triplet sector.} \end{aligned} \quad (2.23)$$

The dark sector self coupling, λ_S does not affect the computation of the relic density. We will discuss the role of the above parameters on DM density in section 5.1. Note that, the present day DM relic density is constrained from the Planck observation [10] which will be discussed in the subsection 3.2.4.

There are several attempts have been made to detect DM in laboratory experiments. Direct detection is one of them where incoming DM flux scatters with the nuclei in the target crystals and the recoil of the target nuclei can be searched for a DM signal. The effective spin-independent DM-Nucleon scattering cross-section ($\sigma_{\text{DI}}^{\text{SI}}$) mediated via t -channel CP -even

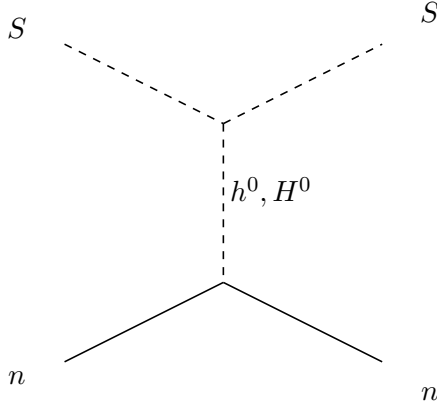


Figure 1. Feynman diagram for spin-independent DM-nucleon scattering process for the scalar DM.

scalars (h^0 and H^0) exchange diagrams, read as ($q \rightarrow 0$):

$$\sigma_{\text{DD}}^{\text{SI}} = \left(\frac{\Omega_S h^2}{\Omega_{\text{DM}} h^2} \right) \left(\frac{1}{4\pi} \left(\frac{f_n \mu_n}{m_S} \right)^2 \left(\frac{m_n}{v_d} \right)^2 \left[\frac{\lambda_{D1}}{m_{h^0}^2} + \frac{\lambda_{D2}}{m_{H^0}^2} \right]^2 \right), \quad (2.24)$$

where $\left(\Omega_S h^2 / \Omega_{\text{DM}} h^2 \right) \equiv \xi_{\text{DM}}$ is the fractional DM density. The coupling λ_{D1} and λ_{D2} are defined as

$$\begin{aligned} \lambda_{D1} &= \left(\lambda_{SH} v_d \cos \theta_t + \lambda_{S\Delta} v_t \sin \theta_t \right) \cos \theta_t \xrightarrow{\theta_t \rightarrow 0} \simeq \lambda_{SH} v_d \\ \lambda_{D2} &= \left(-\lambda_{SH} v_d \sin \theta_t + \lambda_{S\Delta} v_t \cos \theta_t \right) \sin \theta_t \xrightarrow{\theta_t \rightarrow 0} \simeq 0 \end{aligned} \quad (2.25)$$

The reduced mass of DM-nucleon system is defined by μ_n ($= \frac{m_S m_n}{m_S + m_n}$) with $m_n = 0.946$ GeV and the nucleon form factor $f_n = 0.28$ [55]. For the limiting case: $\theta_t \rightarrow 0$, $\sigma_{\text{DD}}^{\text{SI}}$ solely depends on the the Higgs portal DM coupling, λ_{SH} and the DM mass, m_S . The null results from the various DM direct search experiments such as XENON-1T [56] and PANDA-4T [57] put a strong constraint on DMDD cross-sections which can be further expressed in terms of the model parameters.

At the same time, DM can also be detected at various indirect search experiments such as the space-based telescopes, Fermi Large Area Telescope (Fermi-LAT) [30] and the ground-based telescopes, Major Atmospheric Gamma-ray Imaging Cherenkov (MAGIC) [58]. These experiments are looking for the gamma-ray flux which is produced via the production of the SM particles either through DM annihilation or via decay in the local Universe. The photons which are emitted from WIMP-like DM lie in the gamma-ray regime and behave as ideal messengers of DM indirect detection. The total gamma-ray flux due to DM annihilation into the SM charge pairs ($\psi\bar{\psi}$) in a specific energy range is given by [58]

$$\Phi_{\psi\bar{\psi}} = \frac{1}{4\pi} \frac{\langle \sigma v \rangle_{SS \rightarrow \psi\bar{\psi}}}{2m_S^2} \int_{E_{\text{min}}}^{E_{\text{max}}} \frac{dN_\gamma}{dE_\gamma} dE_\gamma \underbrace{\int dx \rho_S^2(r(b, l, x))}_J, \quad (2.26)$$

where $\psi := \{\mu^-, \tau^-, b, W^-\}$. The J factor contains the astrophysical information about the DM distribution in the galaxy and $\frac{dN_\gamma}{dE_\gamma}$ is the energy spectrum of incoming photons from DM annihilation. Measuring the gamma-ray flux and using the standard astrophysical inputs, the indirect search experiments put limits on the thermal average cross-section of DM annihilation into different SM charge pairs like $\mu^-\mu^+$, $\tau^-\tau^+$, $b\bar{b}$, W^-W^+ . In order to compare the experimental bound with the theoretically estimated thermal average cross-section of the corresponding DM annihilation channel, one can express the above equation 2.26 as:

$$\langle\sigma v\rangle_{SS\rightarrow\psi\bar{\psi}}^{\text{eff}} = (\Omega_S/\Omega_{\text{DM}})^2 \langle\sigma v\rangle_{SS\rightarrow\psi\bar{\psi}} = \xi_{\text{DM}}^2 \langle\sigma v\rangle_{SS\rightarrow\psi\bar{\psi}}. \quad (2.27)$$

Here the thermal average cross-sections for indirect detection are scaled with the fractional DM density as ξ_{DM}^2 . In this setup the thermal average annihilation cross-sections, $\langle\sigma v\rangle_{SS\rightarrow\psi\bar{\psi}}$ are mostly dominated by s -channel SM Higgs (h^0) exchange diagram and varies as $\propto \lambda_{SH}^2/m_S^2$ (for $\sin\theta_t \rightarrow 0$). Non-observation of any DM signal in such indirect detection experiments put a constraint on the thermal average cross-section of DM annihilation into different SM charge pairs. Those constraints are further expressed in terms of the model parameters.

So far, we have talked about the analytical form of DM abundance, SI direct-detection cross-section and indirect detection cross-section which will help to understand the numerical results. For the numerical analysis, we have used publicly available numerical packages. We first implemented the model in `FeynRules` [59] and then the outputs are fed into `micrOMEGAs` [60] to obtain DM abundance, $\Omega_S h^2$ and direct and indirect detection cross-section.

2.3 Study of EWPT and the production of GWs

In this section, we discuss the theoretical formulation of EWPT in our model and examine the possibility of the EWPT being a strong first-order one, which in turn may facilitate EWBG ¹. We also outline the production of stochastic GW from FOPT.

2.3.1 Effective Higgs potential at finite-temperature

The tree-level scalar potential of the model (see equation 2.3) relevant for the study of EWPT, in terms of the CP -even Higgs fields $\{h_d, h_t \text{ and } h_s\}$, can be written as

$$\begin{aligned} V_0(h_d, h_t, h_s) = & \frac{1}{4}(\lambda_H h_d^4 + (\lambda_2 + \lambda_3)h_t^4 + \lambda_S h_s^4 + (\lambda_1 + \lambda_4)h_d^2 h_t^2 + \lambda_{SH} h_d^2 h_s^2 + \lambda_{S\Delta} h_t^2 h_s^2) \\ & + \frac{\mu_3}{6\sqrt{2}} h_s^3 - \frac{\mu}{\sqrt{2}} h_d^2 h_t - \frac{\mu_H^2}{2} h_d^2 + \frac{\mu_\Delta^2}{2} h_t^2 + \frac{\mu_S^2}{2} h_s^2. \end{aligned} \quad (2.28)$$

The vacuum expectation values ($vevs$) of the scalar fields are assumed to be real at all temperatures. As we have discussed earlier that at $T = 0$, the minima of the scalar potential is $\langle h_d \rangle \equiv v_d$, $\langle h_t \rangle \equiv v_t$ and $\langle h_s \rangle \equiv 0$ where $v = \sqrt{v_d^2 + v_t^2} = 246$ GeV. The zero temperature tree-level potential (as described in equation 2.28) gets quantum corrections from all fields

¹Although in our present analysis, we assume that no spontaneous or explicit \mathcal{CP} occurs in the Higgs sector, we leave the EWBG calculation for a future study, taking appropriate \mathcal{CP} into account.

that couple to h_d , h_t and h_s . These corrections can be written in terms of the well-known Coleman-Weinberg (CW) [61] one-loop potential in the following form:

$$V_{\text{CW}}(h_d, h_t, h_s, T = 0) = \sum_i (-1)^{2s_i} n_i \frac{m_i^4(h_d, h_t, h_s)}{64\pi^2} \left[\ln \frac{m_i^2(h_d, h_t, h_s)}{Q^2} - C_i \right] , \quad (2.29)$$

where ‘ Q ’ is the renormalization scale which we set at $Q = 246$ GeV . The sum i runs over all particles in the model. The constants C_i depend on the choice of the renormalization scheme. In this work, we consider $\overline{\text{MS}}$ on-shell scheme, whereby for the transverse polarizations of the gauge bosons $C_i = \frac{1}{2}$ and for their longitudinal polarizations and for all other particles (scalars and fermions) $C_i = \frac{3}{2}$, i.e., $C_{W^\pm, Z} = 5/6$ and for other species $C_i = 3/2$. Here, m_i is the field-dependent mass of the i -th species (see Appendix C for the details), and n_i and s_i are their associated number of degrees of freedom and spin, respectively. The number of degrees of freedom of all the fields in the model relevant for equation 2.29 is given below:

$$n_{h_d, h_t, h_s, a_d, a_t, a_s, G^0} = 1, \quad n_{H_\Delta^\pm, H_\Delta^{\pm\pm}, G^\pm} = 2, \quad n_Z = 3, \quad n_{W^\pm} = 6, \quad n_t = 12 . \quad (2.30)$$

In this work, we work in the Landau gauge as the ghost bosons decouple in this gauge and we do not need to consider them in our calculation.

Note that the location of the electroweak minimum in the field space for the tree-level potential is shifted by the one-loop CW potential. Thus, suitable counter-terms need to add to the effective potential to ensure that the minimum of the effective potential coincides with that of the tree-level potential in the $\overline{\text{MS}}$ renormalization scheme. The added counter-terms to the potential are parameterized as,

$$V_{\text{CT}} = \delta_{\mu_H^2} h_d^2 + \delta_{\mu_\Delta^2} h_t^2 + \delta_{\lambda_H} h_d^4 + \delta_{\lambda_2} h_t^4 + \delta_{\lambda_{S\Delta}} h_d^2 h_t^2 + \delta_{\lambda_{SH}} h_d^2 h_s^2 , \quad (2.31)$$

Various coefficients in V_{CT} (of equation 2.31) can be found from the on-shell renormalization conditions at zero temperature:

$$\frac{\partial(V_{\text{CW}} + V_{\text{CT}})}{\partial\phi_i} = 0 , \quad \frac{\partial^2(V_{\text{CW}} + V_{\text{CT}})}{\partial\phi_i \partial\phi_i} = 0 , \quad (2.32)$$

where $\phi_i, \phi_j = \{h_d, h_t, h_s\}$. All the derivatives are taken at the true EW minima, i.e., $h_d = v_d$, $h_t = v_t$ and $h_s = 0$. The various coefficients of the counter-term potentials are presented in the appendix B. Note that, in the Landau gauge that we opt for this work, the masses of the Goldstone modes vanish at the physical minimum. As a result, when physical masses and coupling coefficients are estimated from derivatives of the loop-corrected effective potential, it leads to divergences [62, 63] and it can be handled by using an infrared regulator by changing the masses of the Goldstone modes, $m_G^2 \rightarrow m_G^2 + \mu_{\text{IR}}^2$. In this work, we adopt the approach which is considered in reference [64, 65] i.e., for numerical calculation it is sufficient to set $\mu_{\text{IR}}^2 = 1 \text{ GeV}^2$.

At finite-temperatures, the effective potential receives additional corrections and that at the one-loop level are given by [66–68]

$$V_{\text{th}}(h_d, h_t, h_s, T) = \frac{T^4}{2\pi^2} \sum_i n_i J_{B,F} \left(\frac{m_i^2(h_d, h_t, h_s)}{T^2} \right) , \quad (2.33)$$

where n_i are the numbers of degrees of freedom for particles as discussed earlier. The thermal functions $J_{B(F)}$ are for bosonic (fermionic) particles defined as

$$J_{B/F}(y^2) = \pm \text{Re} \int_0^\infty x^2 \ln \left(1 \mp \exp^{-\sqrt{x^2+y^2}} \right) dx, \quad (2.34)$$

where the lower (upper) sign corresponds to fermions (bosons), $\beta \equiv 1/T$ and the sum includes all the particles as described in equation 2.29.

Note that, at high temperature the treatment of the perturbative expansion of the effective potential no longer remain valid. The quadratically divergent contributions from the so-called non-zero Matsubara modes need to be re-summed through the insertion of thermal masses in the one-loop propagator. The corrections are only to the Matsubara zero-modes, i.e., to the longitudinal polarization states of the vector bosons and to all the scalars. Since the thermal contributions to the transverse modes are suppressed due to gauge symmetry [69]. To make the expansion reliable, we adopt the well-known Parwani method [70] and we denote the thermally improved field-dependent masses as M_i^2 , where $M_i^2 = \text{eigenvalues}[m_i^2 + \Pi(T^2)]$ where $\Pi(T^2) = c_{ij}T^2$ and c_{ij} 's are the so-called daisy coefficients. Note that the gauge symmetries plus the discrete Z_3 -symmetry of the present model set the off-diagonal terms of the $\Pi(T^2)$ matrix to zero. Thus, the Daisy coefficients are listed in equations C.2. Including the Coleman-Weinberg and the thermal corrections, the temperature-dependent effective potential at one-loop order is given by

$$V_{\text{eff}}(T) = V_0 + V_{\text{CW}}(M_i^2) + V_{\text{CT}} + V_{\text{th}}(M_i^2, T). \quad (2.35)$$

The EWPT may now be investigated using this potential, with the minima of the potential being tracked as a function of temperature. Note that the total one-loop effective potential (equation 2.35) carries explicit gauge dependence. Since, the important quantities of the study of phase transitions such as the locations of the extrema of $V_{\text{eff}}(T)$, as well as the ratio $\phi_c(T_c)/T_c$, both are gauge-dependent [66, 71–80].² The problem of defining a gauge-independent version of the one-loop effective potential that incorporates the entire bosonic thermal contribution remains unsolved and is outside the scope of this study. In addition, the one-loop effective potential of equation 2.35 explicitly depends on the choice of the renormalization scale (Q), which might have a more significant impact than the gauge uncertainty [81].

The production of the stochastic GWs from FOPTs will be discussed in the next subsection. Later, we shall use this to identify a suitable region of parameter space of the model that can be investigated using various future GWs experiments.

2.3.2 Production of stochastic GWs from FOPT

In this Z_3 -symmetric singlet scalar extended type-II seesaw model, multi-step FOPTs may occur in the early Universe, potentially generating a stochastic background of GW. The amplitude of this stochastic background, in contrast to GW from a binary system, is a

²Using the Nielsen identities [71, 72], we can get gauge-independent variables of the effective potential.

random quantity that is unpolarized, isotropic and has a Gaussian distribution [82]. As a result, the two-point correlation function can characterize this, and it is proportional to the power spectral density $\Omega_{\text{GW}}h^2$. The ‘‘cross-correlation’’ method between two or more detectors can be used to detect this kind of stochastic GW [83–87].

To determine the GW signals arising from FOPTs and evaluate their evolution with temperature we require the knowledge of the following set of portal parameters: $T_n, \alpha, \beta/H_n, v_w$. Here, the bubble nucleation temperature, T_n , is the approximate time at which one bubble per Hubble volume forms due to a phase transition. A dimensionless quantity, ‘ α ’, is defined as the ratio of the energy released from the phase transition to the total radiation energy density at the time when the phase transition is complete. Thus, it relates to the energy budget of the FOPT and is given by [88]

$$\alpha = \frac{\rho_{\text{vac}}}{\rho_{\text{rad}}^*} = \frac{1}{\rho_{\text{rad}}^*} \left[T \frac{\partial \Delta V(T)}{\partial T} - \Delta V(T) \right] \Bigg|_{T_*}, \quad (2.36)$$

where $T_* = T|_{t_*}$. t_* is the time when the FOPT completes. In the absence of substantial reheating effects, $T_* \simeq T_n$. The total radiation energy density of the plasma background is $\rho_{\text{rad}}^* = g_* \pi^2 T_*^4/30$, where g_* is the number of relativistic degrees of freedom at $T = T_*$. In this work, we consider $g_* \sim 100$. The difference between the potential energies at the false and the true minima is denoted by $\Delta V(T) = V_{\text{false}}(T) - V_{\text{true}}(T)$. The other two parameters are the parameter β , which roughly indicates the inverse time duration of the phase transition, and the parameter v_w , which is the bubble wall velocity.

The tunnelling probability from the false vacuum to the true vacuum per unit time per unit volume is given by [89]

$$\Gamma(T) \simeq T^4 \left(\frac{S_3(T)}{2\pi T} \right)^{3/2} e^{-S_3(T)/T}, \quad (2.37)$$

where the Euclidean action $S_3(T)$ of the background field (ϕ), in the spherical polar coordinate, is given by

$$S_3(T) = 4\pi \int dr r^2 \left[\frac{1}{2} \left(\partial_r \vec{\phi} \right)^2 + V_{\text{eff}} \right], \quad (2.38)$$

with V_{eff} being the finite temperature total effective potential defined in equation 2.35, and $\vec{\phi}$ denoting the three components vev of the scalar fields. The condition for the formation of a bubble of critical size can be found by extremizing this Euclidean action. For this study, we use the publicly available toolbox **CosmoTransitions** [90] to find bounce solutions of the above Euclidean action. It uses a path deformation method and this computation is the most technically challenging part. The bubble nucleation rate (Γ) per unit volume at temperature T is given by $\frac{\Gamma(T)}{V} \propto T^4 e^{-S_3/T}$. The nucleation temperature is usually determined by solving the following equation of the nucleation rate,

$$\int_{T_n}^{\infty} \frac{dT}{T} \frac{\Gamma(T)}{H(T)^4} \simeq 1. \quad (2.39)$$

This equation states that the nucleation probability of a single bubble within one horizon volume is approximately 1, and it reduces to the condition $S_3(T)/T \approx 140$, solving which one can obtain the nucleation temperature T_n [32]. This is the highest temperature for which $S_3/T \lesssim 140$. For all $T > 0$, if $S_3/T > 140$, the corresponding transition to the true vacuum or nucleation of bubbles of critical size of the broken phase does not happen. This occurs because either the barrier between the two local minima is too high or the distance between them is too large in the field space, resulting in a low tunnelling probability. For $T < T_c$, if this condition is not fulfilled, the system would remain trapped at the metastable or false minimum. Thus, in spite of the presence of a deeper minima of the potential at the zero temperature the Universe remains at the false minima. This phenomenon suggests that, rather than just establishing the existence of a critical temperature for a FOEWPT, it is more important to investigate the successful nucleation of a bubble of the broken electroweak phase.

The inverse time duration of the phase transition, β , is obtained from the relation

$$\beta = -\left.\frac{dS_3}{dt}\right|_{t_*} \simeq \frac{\dot{\Gamma}}{\Gamma} = H_* T_* \left.\frac{d(S_3/T)}{dT}\right|_{T_*}, \quad (2.40)$$

where H_* is the Hubble rate at T_* . For a strong GW signal, the ratio needs to be low which implies a relatively slow phase transition.

Having defined the portal we need to know two more parameters to calculate the GW power spectrum coming from a FOPT in the early Universe. When a phase transition occurs in a thermal plasma, the released energy is shared between the plasma’s kinetic energy, which causes a bulk motion of the fluid in the plasma resulting in GW, and heating the plasma. The quantity κ_v is the fraction of latent heat energy converted into the bulk motion of the fluid, which takes the form [88, 91]

$$\kappa_v \simeq \left[\frac{\alpha}{0.73 + 0.083\sqrt{\alpha} + \alpha} \right]. \quad (2.41)$$

Finally, we need to know κ_{turb} , which is a fraction of κ_v that is used to generate Magneto-Hydrodynamic-Turbulence (MHD) in the plasma. The value of κ_{turb} is unknown but it is expected that $\kappa_{\text{turb}} \approx (5 \sim 10) \kappa_v$ [92], and we consider this fractional value to be 0.1 in all our GW calculations. Now we have all the relevant parameters at our disposal, using which we can calculate the GW energy density spectrum.

It is generally accepted that during a cosmological FOPT, the GW can be produced by three distinct processes: bubble wall collisions, long-standing sound waves in the plasma, and MHD turbulence. For bubble collisions, the GW is generated by the stress-energy tensor located at the wall, and the mechanism is referred to as the “envelope approximation”³. However, for a phase transition proceeding in a thermal plasma, bubble collisions’ contribution

³In fact, the “Envelope approximation” is actually two approximations. In the first approximation, the expanding bubble’s stress-energy tensor is believed to be non-zero only in an infinitesimally thin shell on the bubble surfaces. In the second approximation, when two bubbles interact, it is assumed that this stress-energy tensor vanishes instantly, leaving just the ‘envelopes’ of the bubbles to interact [35, 93–95].

to the total GW energy density is believed to be negligible [96]. On the other hand, the bulk motion of the plasma gives rise to velocity perturbations in it, resulting in the generation of sound waves in a medium made up of relativistic particles. The sound waves receive the majority of the energy released during the phase transition [92, 97–99]. This relatively long-living acoustic production of GW is often regarded as the most dominant one ⁴. Percolation may also cause turbulence in the plasma, particularly MHD turbulence since the plasma is completely ionized. This corresponds to the third source [101–106] of GW production. Thus, summing the contributions of the above two processes (i.e. only the contributions from the sound wave and the MHD turbulence) one obtains the overall GW intensity $\Omega_{\text{GW}}h^2$ from the SFOPT for a given frequency f ,

$$\Omega_{\text{GW}}h^2 \simeq \Omega_{\text{sw}}h^2 + \Omega_{\text{turb}}h^2, \quad (2.42)$$

where $h \approx 0.673$ [107].

The contribution to the total GW power spectrum from the sound waves, $\Omega_{\text{sw}}h^2$, in equation 2.42 can be modelled by the following fit formula [112]

$$\Omega_{\text{sw}}h^2 = 2.65 \times 10^{-6} \Upsilon(\tau_{\text{SW}}) \left(\frac{\beta}{H_\star}\right)^{-1} v_w \left(\frac{\kappa_v \alpha}{1 + \alpha}\right)^2 \left(\frac{g_\star}{100}\right)^{-\frac{1}{3}} \left(\frac{f}{f_{\text{sw}}}\right)^3 \left[\frac{7}{4 + 3 \left(\frac{f}{f_{\text{sw}}}\right)^2} \right]^{\frac{7}{2}}, \quad (2.43)$$

where T_\star is the temperature just after the end of GW production and H_\star is the Hubble rate at that time. For this analysis, we consider the approximation that $T_\star \approx T_n$. The present day peak frequency f_{sw} for the sound wave contribution is

$$f_{\text{sw}} = 1.9 \times 10^{-5} \text{ Hz} \left(\frac{1}{v_w}\right) \left(\frac{\beta}{H_\star}\right) \left(\frac{T_n}{100 \text{ GeV}}\right) \left(\frac{g_\star}{100}\right)^{\frac{1}{6}}. \quad (2.44)$$

It has been shown in recent studies [108, 109] that sound waves have a finite lifetime, which causes $\Omega_{\text{sw}}h^2$ to be suppressed. The multiplication factor $\Upsilon(\tau_{\text{SW}})$ is considered in equation 2.43 to take this suppression into account.

$$\Upsilon(\tau_{\text{SW}}) = 1 - \frac{1}{\sqrt{1 + 2\tau_{\text{sw}}H_\star}}. \quad (2.45)$$

Here, the lifetime τ_{sw} is considered as the time scale when the turbulence develops, approximately given by [110, 111]:

$$\tau_{\text{sw}} \sim \frac{R_\star}{\bar{U}_f}, \quad (2.46)$$

⁴Here, we are presuming that a bubble expanding in plasma can achieve a relativistic terminal velocity. The energy in the scalar field is negligible in this situation and the most significant contributions to the signal are predicted to come from the fluid's bulk motion in the form of sound waves and/or MHD. This is the non-runaway bubble in a plasma (NP) scenario [83, 100].

where R_* is the mean bubble separation, and \bar{U}_f is the root-mean-squared (RMS) fluid velocity. R_* is related to the duration of the phase transition parameter, β , through the relation $R_* = (8\pi)^{1/3} v_w / \beta$ [108, 112]. On the other hand, from hydrodynamic analyses, references [34, 112] has shown that the RMS fluid velocity is given by, $\bar{U}_f = \sqrt{3\kappa_v \alpha / 4}$. At $\tau_{\text{sw}} \rightarrow \infty$, $\Upsilon(\tau_{\text{SW}})$ approaches the asymptotic value 1.

In contrast, the contribution $\Omega_{\text{turb}} h^2$ from the MHD turbulence in equation 2.42 can be modeled by [83]

$$\Omega_{\text{turb}} h^2 = 3.35 \times 10^{-4} \left(\frac{H_*}{\beta} \right) \left(\frac{\kappa_{\text{turb}} \alpha}{1 + \alpha} \right)^{\frac{3}{2}} \left(\frac{100}{g_s} \right)^{\frac{1}{3}} v_w \frac{(f/f_{\text{turb}})^3}{[1 + (f/f_{\text{turb}})]^{\frac{11}{3}} (1 + 8\pi f/h_*)}, \quad (2.47)$$

where turbulence produced GW spectrum present day peak frequency f_{turb} is given by,

$$f_{\text{turb}} = 2.7 \times 10^{-2} \text{ mHz} \frac{1}{v_w} \left(\frac{\beta}{H_*} \right) \left(\frac{T_*}{100 \text{ GeV}} \right) \left(\frac{g_s}{100} \right)^{\frac{1}{6}}, \quad (2.48)$$

with the parameter

$$h_* = 16.5 \times 10^{-6} \text{ Hz} \left(\frac{T_n}{100 \text{ GeV}} \right) \left(\frac{g_*}{100} \right)^{\frac{1}{6}}. \quad (2.49)$$

Before ending our discussion on the framework of GW production from FOPT in the early Universe, a few words are necessary on EWBG. For the early Universe to undergo a successful EWBG via SFOEWPT, one of the parameters discussed in this subsection, the bubble wall velocity (v_w), needs to play an important role. From the preceding GW calculation, it is clear that a larger v_w is required for a stronger GW production, but to achieve the observed matter anti-matter asymmetry a small subsonic v_w is needed. Consequently, a significantly large v_w , which can generate detectable GW signals, is detrimental to the process of producing the observed baryon asymmetry. However, recent studies recognise that v_w may not be the velocity that enters EWBG calculation. This is due to the non-trivial plasma velocity profile surrounding the bubble wall [113]. This will require an in-depth analysis of the effect of particle transport near the wall and we leave it for a future study. For the current work, we assume that expanding bubbles reach a relativistic terminal velocity in the plasma, i.e., $v_w \simeq 1$.

3 Theoretical and experimental constraints

Having set up the framework for our study, we discuss various theoretical and phenomenological constraints on the model parameters that are used in our analysis. While from the theoretical side, we consider the limits coming from EW vacuum stability at zero temperature, perturbativity and partial wave unitarity, the phenomenological discussion includes bounds coming from EW precision observables, neutrino oscillation and other low-energy flavor constraints, DM experiments, and neutral as well as charged Higgs boson searches at the LHC. Although some of the above constraints on this model are recently discussed in reference [31]. Nevertheless, we outline them for the sake completeness of our paper. Such a discussion is useful to determine the targeted region of parameter space for our work.

3.1 Theoretical constraints

In this subsection, we highlight some of the key theoretical constraints on our model parameter space.

3.1.1 Vacuum stability

The scalar potential of the model requires to have a stable vacuum. In other words, it means that at large field values the potential is bounded from below so that the scalar fields do not run away. At large field values, the quadratic and cubic terms in the scalar potential can be neglected in comparison to the quartic term to determine the stability conditions of the scalar potential. Using the copositivity conditions of vacuum stability, as outlined in references [31, 114], we obtain the following relations for our model:

$$\begin{aligned}
\lambda_H &\geq 0, \quad \lambda_S \geq 0, \\
\lambda_2 + \lambda_3 &\geq 0, \quad \lambda_2 + \frac{\lambda_3}{2} \geq 0, \\
\lambda_1 + 2\sqrt{\lambda_H(\lambda_2 + \lambda_3)} &\geq 0, \quad (\lambda_1 + \lambda_4) + 2\sqrt{\lambda_H(\lambda_2 + \lambda_3)} \geq 0, \\
(2\lambda_1 + \lambda_4) + 4\sqrt{\lambda_H(\lambda_2 + \frac{\lambda_3}{2})} &\geq 0, \quad (\lambda_2 + \lambda_3) + \sqrt{(\lambda_2 + \lambda_3)(\lambda_2 + \frac{\lambda_3}{2})} \geq 0, \\
\lambda_{SH} + 2\sqrt{\lambda_S\lambda_H} &\geq 0, \quad \lambda_{S\Delta} + 2\sqrt{\lambda_S(\lambda_2 + \lambda_3)} \geq 0, \\
\lambda_{S\Delta} + 2\sqrt{\lambda_S(\lambda_2 + \frac{\lambda_3}{2})} &\geq 0. \tag{3.1}
\end{aligned}$$

It is also important to note that a stable global minimum sets an upper bound on the dark scalar cubic coupling, μ_3 as $\mu_3/m_S \lesssim 2\sqrt{\lambda_S}$ [54, 115]. For $\lambda_S = 1$, this relation becomes $\mu_3 \lesssim 2m_S$.

3.1.2 Perturbativity

In order to ensure the validity of standard perturbation theory where the one-loop level correction to coupling should be smaller than the tree-level couplings. The quartic and the Yukawa couplings of the interaction Lagrangian should obey the following upper bounds [31, 116] as:

$$\begin{aligned}
|\lambda_H| &\lesssim \frac{2\pi}{3}, \\
|\lambda_1| &\lesssim 4\pi, \quad |\lambda_2| \lesssim 2\pi, \quad |\lambda_3| \lesssim 2\sqrt{2}\pi, \quad |\lambda_4| \lesssim 4\pi, \\
|\lambda_1 + \lambda_4| &\lesssim 4\pi, \quad |\lambda_2 + \lambda_3| \lesssim \frac{2\pi}{3}, \quad |\lambda_1 + \frac{\lambda_4}{2}| \lesssim 4\pi, \quad |\lambda_2 + \frac{\lambda_3}{2}| \lesssim \pi, \\
|\lambda_S| &\lesssim \pi, \quad |\lambda_{SH}| \lesssim 4\pi, \quad |\lambda_{S\Delta}| \lesssim 4\pi \\
&\text{and } |y_L| \lesssim \sqrt{4\pi}. \tag{3.2}
\end{aligned}$$

3.1.3 Partial wave unitarity

The quartic couplings of the scalar potential also be constrained from tree level unitarity of the theory, coming from all possible $2 \rightarrow 2$ scattering amplitudes which will form the S matrix [31, 51, 117]. The eigenvalues of the S matrix are bounded from above as:

$$\begin{aligned}
|\lambda_H| &\leq 4\pi, & |\lambda_1| &\leq 8\pi, & |\lambda_2| &\leq 4\pi, \\
|\lambda_{SH}| &\leq 8\pi, & |\lambda_{S\Delta}| &\leq 8\pi, \\
|\lambda_2 + \lambda_3| &\leq 4\pi, & |\lambda_1 + \lambda_4| &\leq 8\pi, \\
\left|\lambda_1 - \frac{\lambda_4}{2}\right| &\leq 8\pi, & \left|\lambda_1 + \frac{3\lambda_4}{2}\right| &\leq 8\pi, \\
|x_{1,2,3}| &\leq 8\pi,
\end{aligned} \tag{3.3}$$

where $x_{1,2,3}$ are the roots of the following polynomial equation:

$$\begin{aligned}
&24\lambda_1^2\lambda_S + 24\lambda_1\lambda_4\lambda_S - 12\lambda_1\lambda_{S\Delta}\lambda_{SH} - 192\lambda_2\lambda_H\lambda_S + 16\lambda_2\lambda_{SH}^2 - 144\lambda_3\lambda_H\lambda_S + 12\lambda_3\lambda_{SH}^2 + 6\lambda_4^2\lambda_S \\
&- 6\lambda_4\lambda_{S\Delta}\lambda_{SH} + 18\lambda_H\lambda_{S\Delta}^2 + x \left(-12\lambda_1^2 - 12\lambda_1\lambda_4 + 96\lambda_2\lambda_H + 32\lambda_2\lambda_S + 72\lambda_3\lambda_H + 24\lambda_3\lambda_S - 3\lambda_4^2 \right. \\
&\left. + 24\lambda_H\lambda_S - 3\lambda_{S\Delta}^2 - 2\lambda_{SH}^2 \right) + x^2(-16\lambda_2 - 12\lambda_3 - 12\lambda_H - 4\lambda_S) + 2x^3 = 0
\end{aligned} \tag{3.4}$$

3.2 Phenomenological constraints

Next, we turn our attention to the phenomenological constraints on our model parameter space in this subsection.

3.2.1 Neutrino Oscillation data

Explaining the smallness of neutrino masses is one of the key motivations of the model under consideration. Hence, we briefly mention the constraints imposed on the model parameter space coming from neutrino oscillation data. Neutrino oscillation experiments provide bounds on neutrino sector parameters such as mass-squared differences and the mixing angles [118]. The 3σ allowed ranges for these observables depend slightly on the ordering of neutrino masses. Below we list the latest limits from a global fit [118], for the normal ordering (inverted ordering) of neutrino masses

$$\begin{aligned}
\Delta m_{21}^2 &\in [6.82 - 8.04] \times 10^{-5} \text{eV}^2, \\
\Delta m_{3\ell}^2 &\in [2.431 - 2.598] \left([-2.583, -2.412] \right) \times 10^{-3} \text{eV}^2, \\
\sin^2 \theta_{12} &\in [0.269 - 0.343], \\
\sin^2 \theta_{23} &\in [0.407 - 0.618] \left([0.411 - 0.621] \right), \\
\sin^2 \theta_{13} &\in [0.02034 - 0.02430] \left([0.02053 - 0.02436] \right), \\
\delta_{\text{CP}} &\in [107 - 403]^\circ \left([192 - 360]^\circ \right).
\end{aligned} \tag{3.5}$$

Only one set of 3σ allowed values are quoted above for Δm_{21}^2 and $\sin^2 \theta_{12}$ since these two observables are insensitive to the mass ordering of neutrinos. In addition, cosmological observations put an upper bound on the sum of neutrino masses, $\sum_{i=1}^3 m_i < 0.12 \text{ eV}$ [119].

3.2.2 Flavor constraints

The Yukawa interactions of the Higgs triplet with the SM lepton doublets, which generate the non-zero neutrino masses, can also induce charged lepton flavor violating (cLFV) processes. The cLFV processes can arise both at tree-level (e.g. $\ell_\alpha \rightarrow \ell_\beta \ell_\gamma \ell_\delta$) or loop-level (e.g. $\ell_\alpha \rightarrow \ell_\beta \gamma$), where $\alpha, \beta, \gamma, \delta$ are flavor indices. The bounds from the cLFV processes can be quite stringent, and the two channels that impose the strongest limits are muon decay to $3e$ and $e\gamma$ [120]. The branching fractions (BF) of these two important processes are given by [121–124]

$$\begin{aligned} \text{Br}(\mu^- \rightarrow e^+ e^- e^-) &= \frac{|(y_L)_{ee}^\dagger (y_L)_{\mu e}|^2}{4 G_F^2 m_{H^{\pm\pm}}^4}, \\ \text{Br}(\mu^- \rightarrow e^- \gamma) &= \frac{\alpha |\sum_{i=1}^3 (y_L)_{ei}^\dagger (y_L)_{\mu i}|^2}{192 \pi G_F^2} \left(\frac{1}{m_{H^\pm}^2} + \frac{8}{m_{H^{\pm\pm}}^2} \right)^2, \end{aligned}$$

where $(y_L)_{\alpha\beta} = \frac{\sqrt{2} m_{\alpha\beta}^\nu}{v_t}$. The experimental upper limits for $\text{Br}(\mu^- \rightarrow e^+ e^- e^-)$ and $\text{Br}(\mu^- \rightarrow e^- \gamma)$ are 1.0×10^{-12} [125] and 4.2×10^{-13} [126], respectively. Using them we can compute the following lower bounds on v_t as a function of $m_{H^{\pm\pm}}$

$$v_t \gtrsim 0.78\text{--}1.5 \text{ (} 0.69\text{--}2.3) \times 10^{-9} \text{ GeV} \times \left(\frac{1 \text{ TeV}}{m_{H^{\pm\pm}}} \right)$$

for the normal (inverted) ordering of neutrino masses.

3.2.3 Electroweak precision observables

Since the CP -even neutral scalar of the triplet develops an induced vev in this model, it can lead to a deviation of the oblique T parameter from the SM prediction at the tree level itself. In addition, a mass-splitting, Δm , between the components of the triplet can further shift the oblique parameters S , T and U at one-loop level from the SM predictions [127, 128]. The tree-level masses of W and Z bosons within this model get altered, which leads to the following expression of the EW ρ parameter

$$\rho = \frac{m_W^2}{m_Z^2 \cos^2 \theta_W} = \frac{v_d^2 + 2v_t^2}{v_d^2 + 4v_t^2} \simeq 1 - \frac{2v_t^2}{v_d^2}, \quad (3.6)$$

where $v_d = \sqrt{v^2 - 2v_t^2}$ with $v = 246$ GeV. ρ is connected to the T parameter at the tree level by $T_{\text{tree}} \simeq -2v_t^2/v_d^2/\alpha = (1 - \rho)/\alpha$. It is needless to say that the above relations hold only under the assumption $v_t \ll v_d$. This assumption is a natural choice in type-II seesaw motivated models since the triplet vev generates neutrino masses. A tiny v_t will allow us to fit neutrino masses and mixings with small Yukawa couplings satisfying all flavor constraints. The current measurement of the EW observables constrain the ρ -parameter as : $\rho = 1.00038 \pm 0.00020$ [129], which translates into a bound $v_t \leq 2.6$ GeV at 3σ level.

Now, assuming $v_t \ll v_d$, we incorporate the limits from the three EW oblique parameters S , T and U on Δm . In this paper, we exclusively consider $v_t \ll 1$ GeV, and in this regime,

the correction to the T parameter is dominated by 1-loop level contributions compared to the small tree level correction shown above. References [127, 128] show that oblique parameters constrain Δm to be below 40 GeV for a large range of $m_{H^{\pm\pm}}$ values.

3.2.4 DM constraints

Besides neutrino masses, another objective of the model used in this paper is to explain the observed DM relic density of the Universe. In Section 2.2 we provided the analytical formulae necessary to calculate the DM abundance, $\Omega_S h^2$, and $\sigma_{\text{DD}}^{\text{SI}}$ within this model. Here, we discuss how we study the DM phenomenology of the model numerically. First, we generated the model files using `FeynRules` [59] and then feed the necessary files into `micrOMEGAs(v4.3)` [60] and perform a scan over the model parameters relevant for the dark sector, as listed in equation 2.23. The package `micrOMEGAs` evaluate $\Omega_S h^2$ and $\sigma_{\text{DD}}^{\text{SI}}$ for each benchmark point.

It is well known that the Planck collaboration measured the DM relic abundance to be 0.120 ± 0.001 , which we take into cognizance in our DM analysis. On the other hand, the most stringent bounds on $\sigma_{\text{DD}}^{\text{SI}}$ are provided by the latest XENON-1T [56] and PANDA-4T [57] results. While imposing these upper limits on $\sigma_{\text{DD}}^{\text{SI}}$ we take into account a scale factor (ξ_{DM}), which is the ratio of the computed relic density for the DM particle of the model and the observed DM relic density of the Universe, i.e., $\xi_{\text{DM}} = \frac{\Omega_S h^2}{0.120} \cdot \xi_{\text{DM}}$ alleviates the strong bounds on $\sigma_{\text{DD}}^{\text{SI}}$ for a significant fraction of our scanned points. More details about how the above DM relic density and direct detection constraints are incorporated in our numerical analysis are discussed in Section 5.1.

The indirect search of DM followed from the experiments such as Fermi-LAT and MAGIC also put a constraint on the individual thermal average annihilation cross-section of DM into SM charge pairs as $\xi_{\text{DM}}^2 \langle \sigma v \rangle_{SS \rightarrow \psi \bar{\psi}}$ where $\psi := \{\mu^-, \tau^-, b, W^-\}$ [58]. When the density of DM is under-abundant, the scale factor ξ_{DM} further reduces the effective indirect search cross-section and alleviates bounds on the corresponding annihilation process. Like the direct search, same portal coupling, λ_{SH} is also involved in the indirect search cross-section. The direct search of DM puts a strong constraint on the portal coupling, λ_{SH} , which leads to a small indirect search cross-section well below the existing upper bound of the corresponding process. Therefore in our discussion of available DM parameter space in Section 5.1, we ignore the indirect search constraints, which are automatically satisfied once direct search constraints take into account.

3.2.5 LHC constraints

Finally, we discuss the phenomenology of the Higgs sector at the LHC in this subsection. The production of the triplet scalars at the LHC via s -channel exchange of Z/γ^* and W^\pm lead to various final states of the SM particles from their prompt decays. The wide array of phenomenological consequences of type-II seesaw at the LHC has been thoroughly studied in the literature [124, 127, 130–171]. Numerous collider searches have been carried out by the CMS and ATLAS collaborations to hunt for the same at the LHC [172–181]. However, there

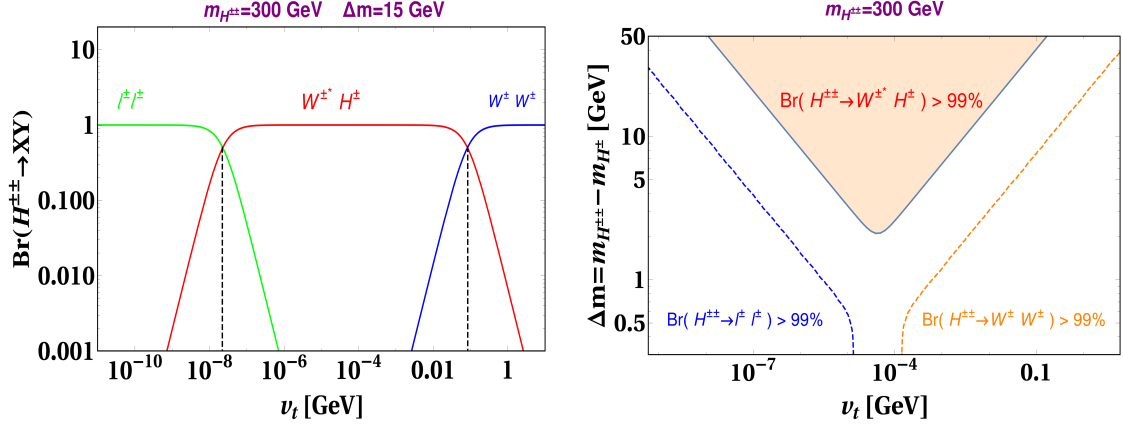


Figure 2. [Left] Branching ratios of doubly charged scalar, $H^{\pm\pm}$ as a function of v_t for $m_{H^{\pm\pm}} = 300$ GeV and $\Delta m = 15$ GeV. [Right] Phase diagram for $H^{\pm\pm}$ decays to different modes is shown in $\Delta m - v_t$ plane by different contour lines: the leptonic decay mode by blue dotted line, the gauge boson decay mode by orange dotted line and the cascade decay mode by the blue line. Each contour line corresponds to 99% of the branching ratio for the corresponding decay channel. The mass of $H^{\pm\pm}$ is kept fixed as $m_{H^{\pm\pm}} = 300$ GeV. The cascade dominated region ($Br(H^{\pm\pm} \rightarrow W^\pm H^\pm) > 99\%$), which we are interested in our discussion is shown by the shaded orange region.

has not been any evidence of an excess over the SM background expectations so far. Thus, these searches strongly constrain the parameter space relevant to the type-II seesaw model.

The most tantalizing collider signature of a type-II seesaw motivated model is the production and decay of $H^{\pm\pm}$. It is well known that $H^{\pm\pm}$ can decay to $\ell^\pm \ell^\pm$ ($W^\pm W^\pm$) for low (relatively large) values of v_t , when the triplet scalars are degenerate in mass. If one introduces a mass-splitting between the triplet scalars, additionally, the $H^{\pm\pm} \rightarrow H^\pm W^\pm$ decay channel opens up for $\Delta m > 0$ scenarios. However, as we have seen in Section 3.2.3, the EW precision observables limit the mass-splitting, Δm , to be less than 40 GeV. Hence, this restricts $H^{\pm\pm}$ to decay to either $H^\pm \ell^\pm \nu$ and $H^\pm q \bar{q}'$ via an off-shell $W^{\pm*}$. For $\Delta m \lesssim \mathcal{O}(2)$ GeV, when quarks cease to remain as free particles, then $H^{\pm\pm}$ decay to $H^\pm \pi^\pm$ has to be considered also. Similar behavior can be observed for decays of H^\pm as well, again for $\Delta m > 0$, leading to a cascade decay of $H^{\pm\pm}$ in turn. In fact, for $v_t \sim 10^{-3} - 10^{-6}$ GeV, the $H^{\pm\pm}(H^\pm) \rightarrow H^\pm(H^0/A^0)W^{\pm*}$ decay becomes the dominant decay channel for $\Delta m \gtrsim 10$ GeV. For a detailed discussion on the various decay channels of $H^{\pm\pm}(H^\pm)$ we refer interested readers to references [137, 182]. To illustrate the above points we show BF's of $H^{\pm\pm}$ to $\ell^\pm \ell^\pm$ ($W^\pm W^\pm$), and the cascade channel ($H^\pm W^{\pm*}$) for $m_{H^{\pm\pm}} = 300$ GeV with $\Delta m = 15$ GeV in the left panel of figure 2. In contrast, we display the $Br(H^{\pm\pm} \rightarrow H^\pm W^{\pm*}) > 99\%$ region by the shaded area in the right panel of figure 2 as a function of v_t as well as Δm .

In the $\Delta m = 0$ case, the ATLAS collaboration places the most stringent bound of $m_{H^{\pm\pm}} \gtrsim 870$ GeV, assuming $Br(H^{\pm\pm} \rightarrow \mu^\pm \mu^\pm)$ to be 100% [178], and using 36.1 fb^{-1} data at $\sqrt{s} = 13$ TeV. On the other hand, ATLAS again excludes $m_{H^{\pm\pm}} \gtrsim 350$ GeV in the $W^{\pm\pm}$ final state with 139 fb^{-1} of data [181]. The first bound is applicable in the small v_t regime, while the second is for relatively large v_t values. It is clear from the discussion in the previous

paragraph that the above limits are not applicable to the whole $\Delta m - m_{H^{\pm\pm}}$ plane for the range of v_t , where the cascade decay have a significant BF.

Let us first consider $\Delta m < 0$ scenarios. For a large mass-splitting ($\mathcal{O}(10)$ GeV) and a moderate v_t , cascade decays of $H^0/A^0 \rightarrow H^\pm W^{\mp*}$ and $H^\pm \rightarrow H^{\pm\pm} W^{\mp*}$, dominate over other decays. In this regime, $H^{\pm\pm}$ is the lightest triplet scalar, and decays to either $\ell^\pm \ell^\pm$ or $W^\pm W^\pm$ depending on the choice of v_t . Hence, the effective pair production cross-section of $H^{\pm\pm}$ is augmented by cascade decays of H^0, A^0 and H^\pm . So, one can expect the bounds on $m_{H^{\pm\pm}}$ to be strong for $\Delta m < 0$ scenarios compared to the $\Delta m = 0$ case. In a recent analysis, reference [124] has shown by recasting various ATLAS and CMS analyses that for $\Delta m = -10$ (-30) GeV the present exclusion limit for $m_{H^{\pm\pm}}$ is 1115 (1076) GeV with $v_t \sim 10^{-5} - 10^{-6}$ GeV. In the same paper, the authors have improved the bound on $m_{H^{\pm\pm}}$ for $\Delta m = 0$ to 955 GeV (420 GeV) for small (relatively large) v_t .

On the other hand, in $\Delta m > 0$ scenarios, $H^{\pm\pm}$ is the heaviest triplet member, and again for a mass-splitting of $\mathcal{O}(10)$ GeV and a moderate v_t , $H^{\pm\pm}$ will mostly undergo the cascade decay, $H^{\pm\pm} \rightarrow W^{\pm*} H^\pm \rightarrow W^{\pm*} W^{\pm*} H^0/A^0$. H^0 and A^0 mostly decay to invisible neutrinos for $v_t < 10^{-4}$ GeV. H^0 can also decay to $b\bar{b}$ or $\tau^+\tau^-$ if its mixing angle with the SM Higgs is sufficiently large. The EW precision bound of $\Delta m < 40$ GeV ensures that the leptons and jets arising from $H^{\pm\pm}$ cascade decay will be soft and may not cross the $p_T^{\ell/j}$ thresholds required in canonical $\ell^\pm \ell^\pm$ and $W^\pm W^\pm$ searches for $H^{\pm\pm}$. Reference [124] shows that even with 3 ab^{-1} of integrated luminosity data, the LHC will be unable to constrain $m_{H^{\pm\pm}} \gtrsim 200$ GeV for $\Delta m = 10$ GeV (30 GeV), with v_t around 10^{-3} GeV to 10^{-5} GeV (10^{-3} GeV to 10^{-6} GeV). This scenario is akin to compressed supersymmetry spectra and a dedicated search strategy is required to develop to probe this region [183–186].

In addition, the measurement of the properties of the observed 125 GeV Higgs boson can also restrict some of our model parameters. As the observed Higgs boson's couplings to the SM particles are found to be almost SM-like, it will not allow a significant mixing between the neutral CP -even components of the triplet and the SM doublet. In order to satisfy the Higgs signal strength bounds, the mixing angle $\sin \theta_t$, defined in equation 2.7, should be below 0.1 [187, 188]. The observed Higgs can decay to a pair of DM scalars if $m_S < m_{h^0}/2$. Hence, we impose the limit $\text{Br}(h^0 \rightarrow \text{invisible}) < 0.15$ on our model parameters [189].

Furthermore, the decay width of the SM Higgs into a photon pair can be affected by the presence of H^\pm and $H^{\pm\pm}$ in the loops. $\Gamma(h^0 \rightarrow \gamma\gamma)$ can both be enhanced or reduced compared to the SM value depending on the sign of quartic couplings λ_1 and λ_4 . Since the partial decay width of the SM into photons is tiny, the total decay width of h^0 barely changes. The signal strength parameter of $h^0 \rightarrow \gamma\gamma$ channel is defined as,

$$\mu_{\gamma\gamma} = \frac{\Gamma^{\text{NP}}[h^0 \rightarrow \gamma\gamma]}{\Gamma^{\text{SM}}[h^0 \rightarrow \gamma\gamma]} \quad (3.7)$$

where $\Gamma^{\text{SM (NP)}}[h^0 \rightarrow \gamma\gamma]$ denotes the decay rate without (with) the inclusion of new physics. We consider that the production cross-section of h^0 will remain the same when the effect of NP is included since $\cos \theta_t \rightarrow 1$. For more details on $\Gamma(h^0 \rightarrow \gamma\gamma)$ within the type-II seesaw

model we refer the reader to references [190, 191]. The current limits on $\mu_{\gamma\gamma}$ from ATLAS and CMS are $1.04^{+0.10}_{-0.09}$ [192] and 1.12 ± 0.09 [193], respectively.

4 Choice of parameter space

4.1 Implications from Higgs searches

As discussed in subsection 3.2.5, LHC direct searches for $H^{\pm\pm}$ will not be able to limit the triplet-like scalar masses even at 200 GeV for a moderate v_t and relatively large Δm (> 10 GeV) [124]. Depending on the value of v_t and mixing with h^0 , in this scenario, H^0/A^0 either decays into $\nu\nu/b\bar{b}/\tau^+\tau^-$ or $h^0h^0, ZZ/h^0Z$. Henceforth, in this work, we focus on $10 \text{ GeV} < \Delta m < 40 \text{ GeV}$ and $10^{-3} \text{ GeV} < v_t < 10^{-6} \text{ GeV}$ region of parameter space of the type-II seesaw part of the model. On the other hand, the rich scalar sector of this model can generate stochastic GW signals from FOPT in the early Universe. As the LHC fails to constrain this region from the direct searches of triplet-like scalars, we try to probe this region of parameter space from GW experiments.

For $\Delta m > 0$, λ_4 needs to be $-ve$ (see equation 2.13). Thus, we consider $\lambda_4 < 0$ region of parameter space in our analysis. For successful FOPT to take place in the Higgs sector, the two most important quartic couplings are λ_1 and λ_4 . They are responsible for mixing the doublet and the triplet fields (see equation 2.28). We vary the absolute value of these couplings from 0 to 4. Other quartic couplings of the triplet-sector λ_2 and λ_3 do not significantly affect FOPT. Thus, we set them to fixed values for the rest of our study. Since we focus on light triplet-like scalars, we require $m_{H^{\pm\pm}}$ within 200 GeV to 600 GeV, and for that purpose, we vary M_Δ from 100 GeV to 800 GeV. In addition, for the above choice of our v_t and $m_{H^{\pm\pm}}$ values, our benchmark points pass the flavour constraints discussed in subsection 3.2.2 as well.

The precision measurements of h^0 couplings at the LHC restrict the mixing between the doublet-like and the triplet-like CP -even neutral scalars to small values. Therefore, we limit our scan to tiny $\sin\theta_t$ values to allow minimum mixing and maintain the SM-like nature of h^0 . However, loop-induced h^0 decays, such as $h^0 \rightarrow \gamma\gamma$, can deviate significantly from the observed limits even at small $\sin\theta_t$ values. We discuss the variation of the signal strength, $\mu_{\gamma\gamma}$ of the $h^0 \rightarrow \gamma\gamma$ channel in the above-discussed region of parameter space below.

At the one-loop level, the top quark, along with the charged weak gauge bosons and the charged triplet-like Higgs states contribute to the decay of $h^0 \rightarrow \gamma\gamma$. The deviation of the signal strength of this decay channel $\mu_{\gamma\gamma}$, defined in equation 3.7, from 1 can become a signature of new physics beyond the SM. We present that the variation of $\mu_{\gamma\gamma}$ for $\lambda_1 > 0$, $\lambda_4 < 0$, $M_\Delta = 300 \text{ GeV}$ and $v_t = 10^{-4} \text{ GeV}$ in figure 3. The variation of λ_1 and λ_4 are presented in the x -axis and y -axis, respectively, whereas the variation of $\mu_{\gamma\gamma}$ is indicated by palette colors. The figure also takes into consideration the theoretical constraints. Due to constraints from vacuum stability that are discussed in section 3.1.1,⁵ the white empty

⁵Particularly from the inequality relations: $(\lambda_1 + \lambda_4) + 2\sqrt{\lambda_H(\lambda_2 + \lambda_3)} \geq 0$ and $(2\lambda_1 + \lambda_4) + 4\sqrt{\lambda_H(\lambda_2 + \frac{\lambda_3}{2})} \geq 0$

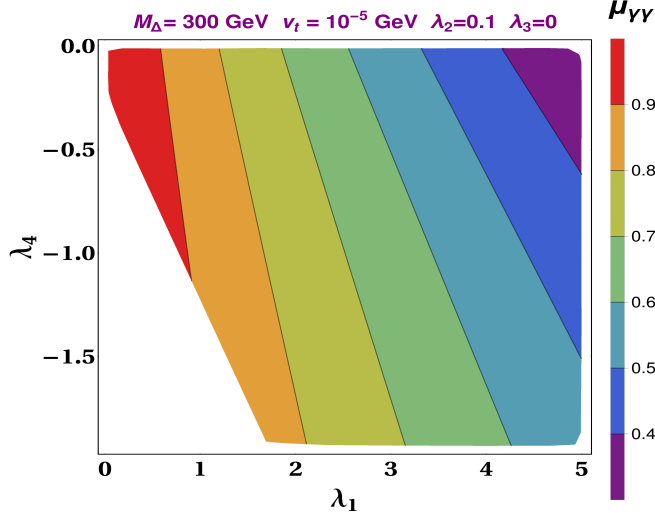


Figure 3. Variation of the signal strength $\mu_{\gamma\gamma}$ in the $\lambda_1 - \lambda_4$ plane. The other two parameters, M_Δ and v_t , of the triplet sector that can alter the signal strength are fixed at 300 GeV and 10^{-5} GeV, respectively.

section of figure 3 is excluded. We note that due to a destructive interference between the SM and BSM contributions to $\mu_{\gamma\gamma}$, it is mostly less than 1 for $\lambda_4 < 0$. The deviation of $\mu_{\gamma\gamma}$ from 1 increases with the increase of the absolute values of λ_1 and λ_4 . Thus the precision study of $\mu_{\gamma\gamma}$ at the LHC and other proposed collider experiments can exclude a significant amount of the parameter space of our interest in this paper. We shall discuss this issue further in section 5.

4.2 Implications from DM searches

In contrast to the Higgs sector discussed above, in the dark sector, we vary m_S , λ_{SH} , and $\lambda_{S\Delta}$ within a certain range to satisfy all DM constraints. λ_{SH} coupling has a significant impact on FOPT as it mixes the singlet h_s field with the h_d -field (see equation 2.28). Thus, the possibility of a strong FOPT is expected to increase with a large λ_{SH} . However, as we have already discussed in section 2.2, increasing the same coupling increases $\sigma_{\text{DD}}^{\text{SI}}$ as well. Hence, large λ_{SH} values are ruled out by DM direct detection limits. We shall discuss this issue in more detail in section 5.3. Another dark sector parameter, μ_3 , also impacts both DM and the FOPT. This coupling not only can produce the necessary barrier for FOPT but also contributes to DM semi-annihilation processes. We vary this parameter in our study satisfying the constraints $\mu_3/m_S \lesssim 2\sqrt{\lambda_S}$ from the stability of the global minimum, which is discussed in subsection 3.1.1.

To summarize, the ranges of input parameters of the model we consider for the scan are listed in table 2. The other parameters are fixed at $\lambda_H = 0.129$, $\lambda_2 = 0.1$, $\lambda_3 = 0$, $\lambda_S = 0.1$.

Varying parameters	λ_1	λ_4	M_Δ (GeV)	v_t (GeV)	m_S (GeV)	$ \lambda_{SH} $	$ \lambda_{S\Delta} $	μ_3 (GeV)	$ \lambda_S $
Ranges	0 – 4	-4 – 0	100 – 800	$10^{-6} - 10^{-3}$	0 – 1000	< 4	< 6	< 1000	< 6

Table 2. Ranges of various model parameters employed for scanning the present model parameter space.

5 Results

In this section, we investigate the DM phenomenology, the thermal history regarding a FOEWPT, the associated production of stochastic GW and the interplay among the DM, GW and the collider physics in this model. In the subsection 5.1, we analyse the dependencies of the DM phenomenology in terms of both DM relic density and DMDDSI cross-section on the triplet-sector scalar masses. We study the variation of various model parameters of the dark sector in the estimation of relic density and DMDDSI cross-section. Implications of the various model parameters on FOEWPT have been studied in two parts. The impact of the triplet-sector parameters on the FOEWPT, the production of GW and the interplay with LHC have been studied in the subsection 5.2. Two benchmark scenarios are presented to illustrate the effect of the triplet-sector parameters on the FOEWPT. In the subsection 5.3, we study the possibilities of FOEWPT by altering the shape of the SM Higgs potential mainly from the dark sector. The connection between the DM observables and a FOPT has been discussed. A benchmark scenario that exhibits a two-step phase transition in the early Universe has been presented to illustrate such a scenario.

5.1 DM Parameter space

In this section, we discuss the DM parameter space in terms of model parameters which is consistent with DM relic density observed by the PLANCK experiment and the upper bound on DM-nucleon spin-independent cross-section provided by XENON-1T and PANDA-4T experiments. Before going to the details of the parameter space scan, we attempt to comprehend the variation of DM relic density with DM mass, m_S ($\equiv m_{\text{DM}}$) and other relevant parameters of the model such as scalar portal couplings λ_{SH} , $\lambda_{S\Delta}$ and trilinear coupling μ_3 . The abundance of DM also significantly depends on the masses of triplet scalar, i.e., m_{H^0} , m_{A^0} , m_{H^\pm} and $m_{H^{\pm\pm}}$ which can be expressed as the independent parameters as mentioned in equation 2.12. It is difficult to establish the significance of all the relevant parameters that vary simultaneously. Therefore, we fix the triplet sector parameters (in equation 2.12), which simplifies the setup and allows us to investigate DM phenomenology. For DM discussion, we consider one benchmark point from the cascade region of the triplet sector (as discussed in section 4.2) which is given by:

$$\{M_\Delta = 367.7 \text{ GeV}, v_t = 3.3 \times 10^{-4} \text{ GeV}, \lambda_1 = 3.92, \lambda_2 = 0.1, \lambda_3 = 0, \lambda_4 = -0.989\} \quad (5.1)$$

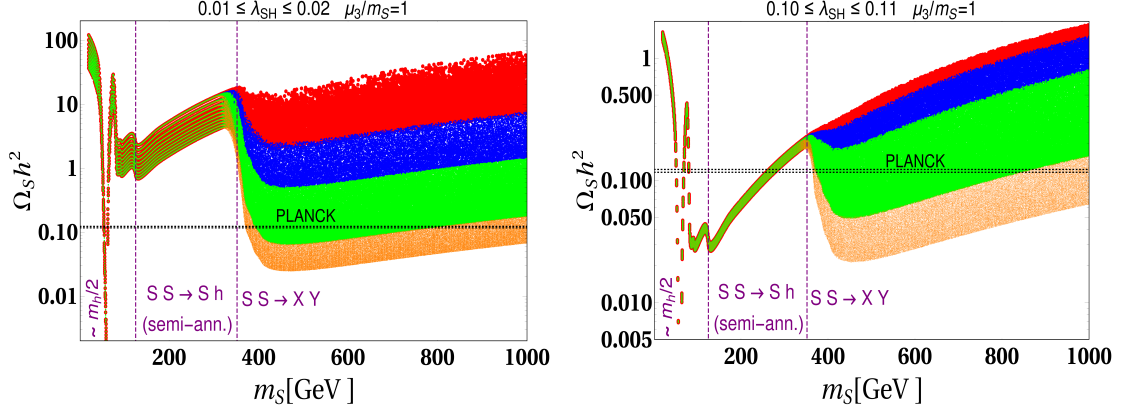


Figure 4. Variation of relic density as a function of DM mass for different ranges $\lambda_{S\Delta}$: $0.01 \leq \lambda_{S\Delta} \leq 0.04$ (red), $0.04 < \lambda_{S\Delta} \leq 0.1$ (blue), $0.1 < \lambda_{S\Delta} \leq 0.3$ (green) and $0.3 < \lambda_{S\Delta} \leq 0.5$ (orange). We illustrate two different choices of λ_{SH} : $\{0.01 - 0.02\}$ (left) and $\{0.10 - 0.11\}$ (right).

which corresponds to the physical masses and mixing angle followed from equations 2.8, 2.9, 2.10 and 2.11 as:

$$\{m_{H^0} = 367.7, m_{A^0} = 367.7, m_{H^\pm} = 387.5, m_{H^{\pm\pm}} = 406.4 \text{ GeV}, \\ \mu = 0.00104, \sin \theta_t = -1.03 \times 10^{-6} \} \quad (5.2)$$

It is worth mentioning here that one can also consider another set of parameters as mentioned above, for which the underlying physics remains the same. The only thing that will change is the allowed region of DM mass depending on the triplet scalar mass. Therefore the phenomenology of DM depends on the following independent parameters in the dark sector along with the above-fixed parameters

$$\{m_S, \mu_3/m_S = 1, \lambda_{SH}, \lambda_{S\Delta}\}. \quad (5.3)$$

Note that for DM discussion we consider here $\mu_3/m_S = 1$ which is responsible for the semi-annihilation process, $S S \rightarrow S h^0$. The larger values of μ_3/m_S lead to a larger semi-annihilation contribution to DM abundance. However, a stable EW vacuum sets an upper bound on the trilinear coupling, $\mu_3 \leq 2m_S$ as discussed earlier.

In Fig.4, we show the variation of DM abundance ($\Omega_S h^2$) as a function of m_S for two different choices of λ_{SH} : $0.01 \leq \lambda_{SH} \leq 0.02$ (left) and $0.10 \leq \lambda_{SH} \leq 0.11$ (right). Different colored patches indicate different ranges of DM portal coupling with triplet, $\lambda_{S\Delta}$: $0.01 \leq \lambda_{S\Delta} \leq 0.04$ (red), $0.04 < \lambda_{S\Delta} \leq 0.1$ (blue), $0.1 < \lambda_{S\Delta} \leq 0.3$ (green) and $0.3 < \lambda_{S\Delta} \leq 0.5$ (orange) are considered for each plot. The black dotted horizontal lines indicate the observed DM relic density from the PLANCK data [10], i.e., $\Omega_{\text{DM}} h^2 = 0.120$. With the increase in DM mass, different number-changing processes open up after crossing some threshold values resulting in a drop in relic density.

- $m_S < m_{h^0}$: When DM mass, $m_S < m_{h^0}$, the DM abundance is mostly dominated by the $S S \rightarrow \text{SM SM}$ number changing process which is mediated by both the CP even Higgses,

h^0 and H^0 . And the density of DM varies as:

$$\Omega_S h^2 \propto \frac{1}{\langle \sigma v \rangle_{SS \rightarrow \text{SM SM}}} \quad (5.4)$$

where for the small $\sin \theta_t$ limit, $\langle \sigma v \rangle_{SS \rightarrow \text{SM SM}} \propto \lambda_{SH}^2 / m_S^2$ and almost independent of $\lambda_{S\Delta}$ which is shown from the above Figs.4. The annihilation contribution will get suppressed with the increase of DM mass and hence relic density increases. For a fixed DM mass, with an increase of $\lambda_{\phi H}$, relic density decreases as it is shown in the right panel figure. A sharp drop in DM density due to the SM Higgs, h^0 resonance near $m_S \sim m_{h^0}/2$. Beyond the Higgs(h^0) pole, $m_S > m_W, m_Z$, DM annihilates into a pair gauge final states resulting in a large enhancement in $\langle \sigma v \rangle$, which leads to less density.

- $m_{h^0} \leq m_S < m_{H^0}$: A new annihilation channel, $S S \rightarrow S h^0$ (semi-annihilation) starts contributing when the DM mass becomes heavier than Higgs mass ($m_S > m_{h^0}$) thanks to the trilinear coupling, μ_3 present in this scenario. Therefore the relic density of DM in this region is followed as:

$$\Omega_S h^2 \propto \frac{1}{\langle \sigma v \rangle_{SS \rightarrow \text{SM SM}} + \langle \sigma v \rangle_{SS \rightarrow S h^0}} \quad (5.5)$$

The second term in the above equation depends on μ_3 and λ_{SH} whereas the first term only depends on λ_{SH} . The semi-annihilation contributions dominate over the standard annihilation to SM for a larger value of μ_3 which will help to evade the direct search bound on λ_{SH} . With the increase of λ_{SH} , both standard annihilation and semi-annihilation contributions are significantly enhanced and hence relic density decreases as it is depicted from the left and right panel of Fig.4. Note here that the effect of semi-annihilation becomes pronounced where the propagator suppression is minimal near $m_S \gtrsim m_{h^0}$. There is no variation of relic density with $\lambda_{S\Delta}$ because both the contributions are almost insensitive to the change of $\lambda_{S\Delta}$ for the small $\sin \theta_t$ limit. There is no drop in relic density near $m_S \sim m_{H^0}/2$ due to the second heavy Higgs, H^0 . This is because of the heavy Higgs mediated diagrams, $S S \rightarrow \text{SM SM}$, are strongly suppressed by small $\sin \theta_t$ and v_t .

- $m_S \gtrsim m_{H^0}$: The new annihilation processes start to contribute to DM relic when DM mass is larger than the masses of the triplet states i.e. $2m_S > m_X + m_Y$ and the relic density of DM turns out to be

$$\Omega_S h^2 \propto \frac{1}{\langle \sigma v \rangle_{SS \rightarrow \text{SM SM}} + \langle \sigma v \rangle_{SS \rightarrow S h^0} + \langle \sigma v \rangle_{SS \rightarrow X Y}}, \quad \{X, Y\} := \{H^0, A^0, H^\pm, H^{\pm\pm}\}. \quad (5.6)$$

The Higgs mediated s and t channel diagrams for $SS \rightarrow XY$ process are suppressed by a small mixing angle, $\sin \theta_t$ and small v_t . But the four-point contact diagrams for the $SS \rightarrow XY$ process enhance the cross-section significantly with the increase of $\lambda_{S\Delta}$. Therefore the effect of new annihilation to DM relic density becomes more prominent with the increase of $\lambda_{S\Delta}$. Since this coupling is almost insensitive to $\sigma_{\text{DD}}^{\text{SI}}$ for the small mixing angle, one can play with it to satisfy observed DM density. For the smaller values of λ_{SH} and $\mu_3 (= m_S)$, the most

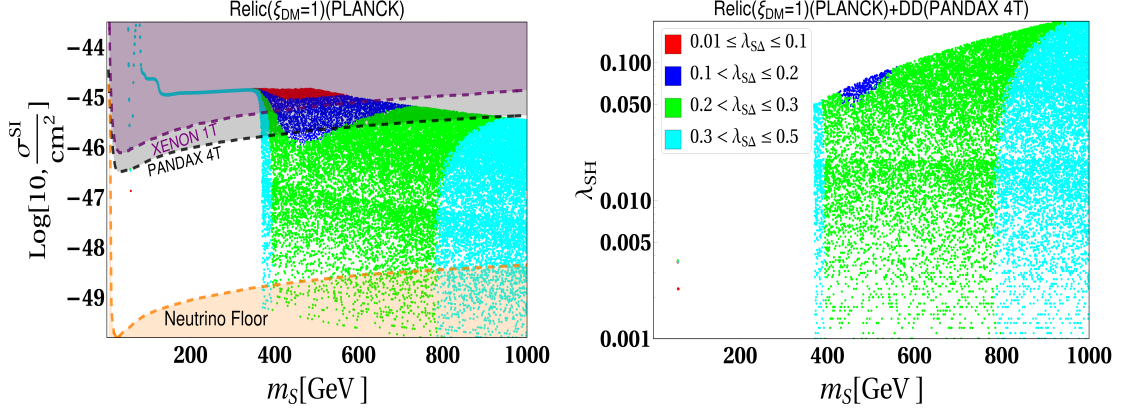


Figure 5. [Left] SI spin-independent DM-nucleon scattering cross-section, (σ_{DD}^{SI}) for relic density allowed(PLANCK) parameter space as a function of DM mass(m_S). For comparison, the current upper bound on the SI DM-nucleon cross-section from XENON 1T [56] and PANDAX 4T [57] data are shown in the same plane. The Neutrino Floor is represented by a shaded orange region. [Right] Relic(PLANCK)+DD(PANDAX-4T) allowed parameter space is shown in $m_S - \lambda_{SH}$ plane for different ranges of $\lambda_{S\Delta}$ shown by different color patches. Note that the relic density of DM, S considered here 100% ($\xi_{DM} = 1$) of observed DM density.

dominant contribution to DM relic is coming from the new annihilation channels, $S S \rightarrow X Y$ whereas the other two contributions, $S S \rightarrow SM, SM$ and $S S \rightarrow S h^0$ are sub-dominant. With the increase of $\lambda_{S\Delta}$, $\langle\sigma v\rangle_{S S \rightarrow X, Y}$ increases and hence relic density decreases which are shown from the left panel of Fig.4 for fixed choices of $\lambda_{SH} : \{0.01 - 0.02\}$ and $\mu_3/m_S = 1$. In the right panel of Fig.4, we considered comparably large values of $\lambda_{SH} : \{0.10 - 0.11\}$ which further increases the $S S \rightarrow SM, SM$ and $S S \rightarrow S h^0$ contributions and hence total effective annihilation cross-section increases. As a result, relic density decreases compared with the left panel figure. Note that a new DM semi-annihilation, $SS \rightarrow SH^0$ is kinematically allowed here but it has almost negligible contribution to relic density as the cross-section is suppressed by the small mixing angle, $\sin \theta_t$ and small v_t .

We shall now move to the parameter space scan. To get the allowed region of parameter space, we perform a three-dimensional random scan over the following parameters keeping other parameters fixed as discussed above.

$$\{m_S : \{30 - 1000\} \text{GeV}, \lambda_{SH} : \{0.001 - 0.3\}, \lambda_{S\Delta} : \{0.01 - 0.5\}\}. \quad (5.7)$$

In the left panel of Fig.5, we show the relic density allowed parameter space (with $\xi_{DM} = 1$) emerging from the random scan in the plane of σ_{DD}^{SI} versus DM mass, m_S . As discussed in section 2.2, for a small mixing limit ($\sin \theta_t \rightarrow 0$), the DD cross-section is proportional to λ_{SH}^2 and almost independent of $\lambda_{S\Delta}$. Therefore with an increase of λ_{SH} , the DD cross-section increases. The latest upper bounds on σ_{DD}^{SI} against DM mass from XENON 1T (purple dashed line) and PANDAX 4T (black dashed line) are shown in the same plane. The parameter space above the dashed line can be disfavoured from the non-observation of the DM signal of the

corresponding direct search experiments. We find that DM mass below the mass of the lightest triplet state ($m_S < m_{H^0}$), the DM-SM Higgs portal coupling, λ_{SH} is required comparably large to satisfy observed relic density which corresponds to large DD cross-section lies above the experimental upper limit. As a result, most of the region ($m_S < m_{H^0}$) is excluded from non-observation of DM signal apart from Higgs poles, $m_S \sim m_{h^0}/2$. Once the triplet final states open up, the DM portal coupling with a triplet, $\lambda_{S\Delta}$ takes up the major role in controlling DM relic density. With the help of $\lambda_{S\Delta}$ which is insensitive to DD-cross-section, the pressure on λ_{SH} can be reduced to produce correct relic density which can evade the direct search bound. This phenomenon can be observed from the right panel of Fig.5. As a result, the region above the DM mass, $m_S > m_{H^0}$ is allowed from both relic and direct search constraints with the help of large $\lambda_{S\Delta} (\gtrsim 0.1)$.

5.2 Implications of the triplet sector parameters on SFOEWPT

We have already discussed how the discovery of a 125 GeV Higgs mass in the SM demonstrates that electroweak breaking occurs through a smooth cross-over transition. However, it can be a FOPT in the presence of additional scalars, going Beyond-the SM. A further benefit of FOEWPT is that it can supply one of the necessary conditions for the explanations of BAU. In this section, we illustrate the possibility of FOPT in the electroweak sector in our choice of parameter region of the current model. To explain the observed matter-antimatter asymmetry via the mechanism of EWBG, the FOPT in the electroweak sector needs to satisfy another additional condition, i.e.,

$$\xi_n = \frac{v_n}{T_n} > 1. \quad (5.8)$$

v_n is the vev in the electroweak minimum at the nucleation temperature T_n . The strength of the FOPT is quantified via ξ_n . This criterion is required to prevent the wash-out of the generated baryon asymmetry after the EWPT. We present four plots of the FOPT-allowed scan results in figure 6 to illustrate the correlations among the model parameters of the triplet-sector in connection with the FOPT and its strength, ξ_n . Here, We fix the various couplings of dark sectors to small values to ensure that their impact on the FOPT is minimal and we vary λ_1 , λ_4 , v_t and M_Δ only in the range as described in table 2. Thus, here we want to study the impact of the triplet-sector parameters on the FOPT in the h_d -field direction. In our scan results $v_n \sim v_h$, since the triplet vev always remains very small.

The plot on top, left of figure 6 shows the FOPT allowed region of λ_1 and λ_4 with the M_Δ being indicated by the palette-color. It shows that FOPT prefers relatively larger λ_1 . We have already discussed that in our choice of parameter region ($\Delta m > 0$), λ_4 has to be $-ve$ and from the theoretical constraints (particularly constraints from the stability) that we have discussed in section 3.1, the absolute value of λ_4 can not be too large compared with λ_1 . As a result, the permitted range of λ_4 rises with larger λ_1 . Color variation reveals that M_Δ needs to be on the smaller side at the relatively smaller values of λ_1 . From equation 2.11, $m_{H^{\pm\pm}} \sim M_\Delta$ at smaller λ_4 . Thus, FOPT demands relatively light triplet-like scalars at smaller quartic coupling λ_1 . At the relatively larger triplet-like scalar masses (larger M_Δ),

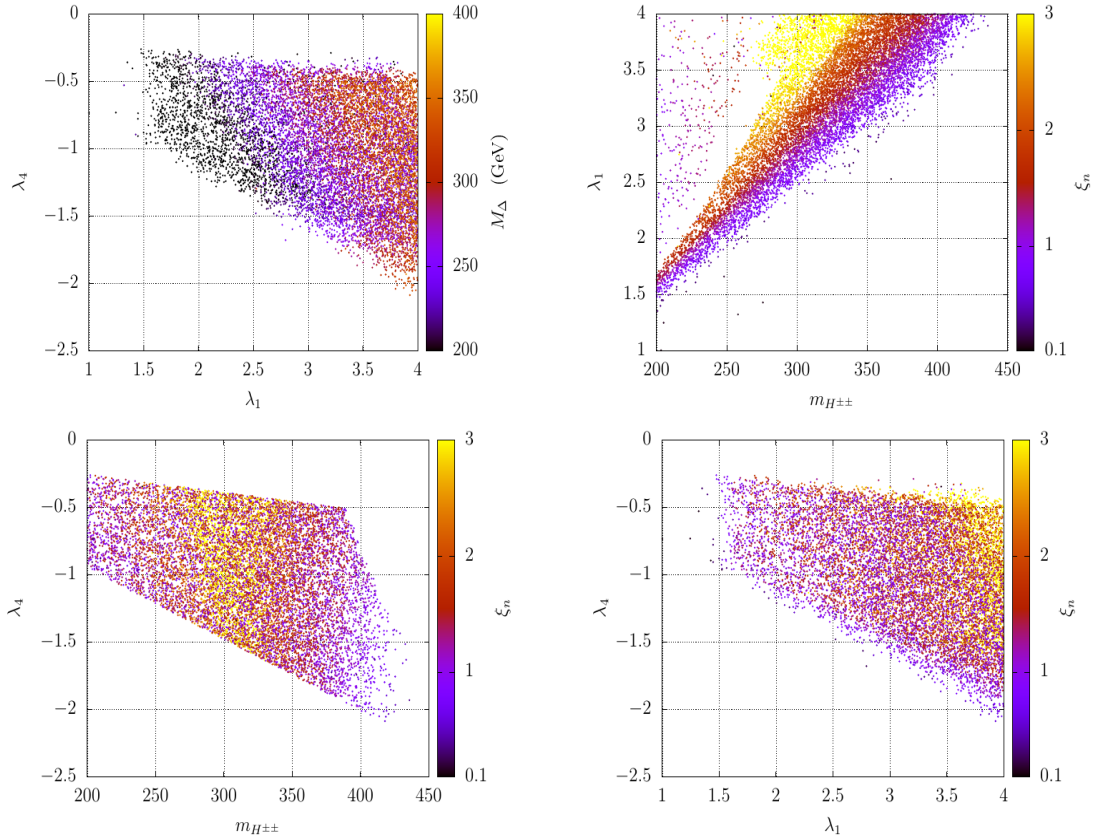


Figure 6. Scattered points that exhibits FOPT along the h_d -field direction in the $\lambda_1 - \lambda_4$ plane with M_Δ (strength of the phase transition, ξ_n) indicated by the palette in the top left (bottom right) plot. The variation of the same points in the $m_{H^{\pm\pm}} - \lambda_1$ ($m_{H^{\pm\pm}} - \lambda_4$) plane with the palette indicating the strength of the phase transition ξ_n is shown in the top right (bottom left) plot.

FOPT demands larger λ_1 . On the other hand, for a given λ_1 , the decrease of the absolute value of λ_4 demands increasing M_Δ for FOPT.

The shape of the SM Higgs potential gets modification from the quartic terms that are proportional with λ_1 and λ_4 in equation 2.28. Thus, the phase transition pattern in the Higgs sector strongly depends on these quartic couplings λ_1 and λ_4 . In the plot on top, right and bottom, left of figure 6, we present the variation of $m_{H^{\pm\pm}}$ with λ_1 and λ_4 , respectively, from our scanned points that satisfy FOPT. The palette-color indicates the associated strength of the FOPT, ξ_n , values. For a fixed $m_{H^{\pm\pm}}$, color variation shows that the strength of the FOPT increases with λ_1 . Thus, larger λ_1 is favoured for SFOEWPT, which is required for EWBG. In addition, for a fixed value of the quartic coupling λ_1 , lighter $m_{H^{\pm\pm}}$ is preferred for SFOEWPT. Thus, larger quartic coupling λ_1 and lower triplet-like scalars increase the strength of the FOPT. The other plot indicates that for a given $m_{H^{\pm\pm}}$, the strength of the FOPT increases with the decrease of the absolute value of λ_4 . The dependence of λ_1 and λ_4 on ξ_n can clearly be understood from the bottom and the right plot of figure 6. It shows that the increase of λ_1 and the decrease of the absolute value of λ_4 increases the strength of the

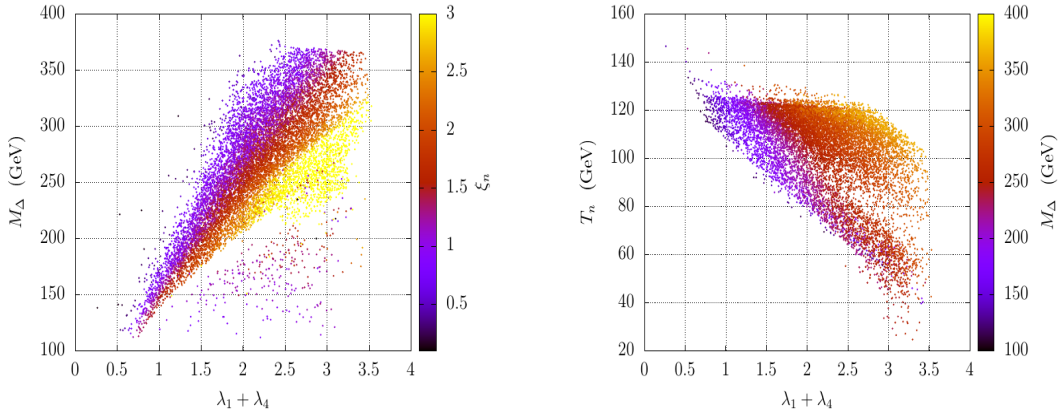


Figure 7. Left: Scatter points in the $(\lambda_1 + \lambda_4) - M_\Delta$ plane that satisfies FOPT along the h_d -field direction with the palettes indicating the strength of the phase transition, ξ_n . Right: Similar to the scatter spots on the left plot but in the $(\lambda_1 + \lambda_4) - T_n$ plane with showing the variation of M_Δ via the palette.

phase transition.

The effective dependence of these quartic couplings on the phase transition pattern can be quantified in terms of the sum of these two quartic couplings, i.e., $\lambda_1 + \lambda_4$. We present the variation of $\lambda_1 + \lambda_4$ with M_Δ with ξ_n being indicated by the palette-color in the left plot of figure 7. The variation of colors indicates that the strength of FOPT increases with the increase of the effective quartic coupling ($\lambda_1 + \lambda_4$) and decrease of M_Δ (or, the triplet-like scalar masses).

Another very important quantity of the FOPT is the temperature at which the PT starts to occur, i.e., the nucleation temperature (T_n). We have discussed in section 2.3.2 that the production of GW peak amplitude and the peak frequency from a FOPT depend on T_n . Thus, studying the variations of T_n with the various model parameters is important to identify the region of parameter space for a strong GW signal from FOPT. Keeping this in mind, We show the variation of T_n with respect to the effective quartic coupling ($\lambda_1 + \lambda_4$) in the right plot of figure 7. The variation of M_Δ is presented in palette color. It can be seen that at relatively small effective quartic coupling, T_n is relatively large. Also, low effective quartic coupling demands relatively low M_Δ . On the other hand, at relatively larger effective quartic coupling, T_n can go down to even below 50 GeV at moderate values of M_Δ .

Finally, after studying all these plots in figures 6 and 7, we can point out that stronger FOEWPT demands relatively larger effective quartic couplings in the potential and relatively low triplet-like scalars in the parameter space. However, various Higgs searches at the LHC can constrain this parameter space. In the following subsection, we discuss the connection between the strength of the FOPT and the production of GW signals and the interplay between the detection of GW and the LHC searches in this region of parameter space.

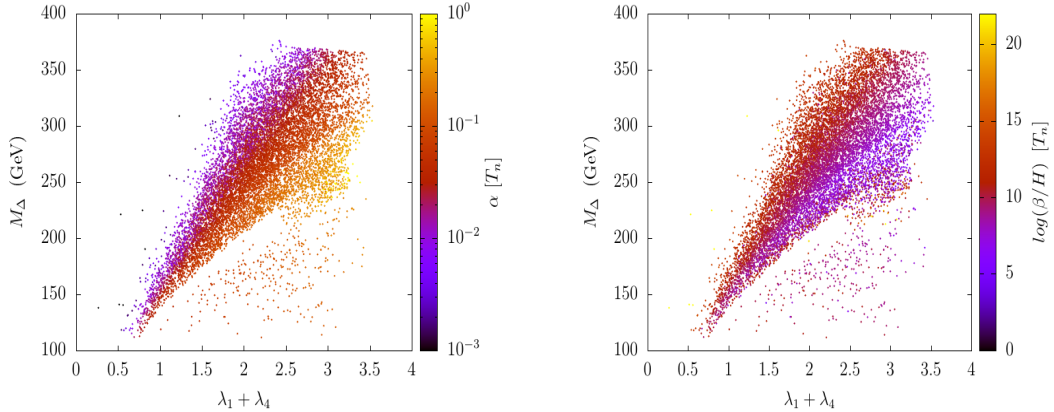


Figure 8. Scatter points in the $(\lambda_1 + \lambda_4) - M_\Delta$ plane that exhibits FOPT along the h_d -field direction. The variation of α ($\log(\beta/H_n)$) is shown in the left (right) plot via the palette.

5.2.1 Production of GW and the interplay with LHC

In section 2.3.2, we have discussed the possibility of producing stochastic GW background from the cosmological FOPT in the early Universe. This can be detected in the various future proposed GW space/ground-based detectors. The important portal parameters that control the GW intensity are α , β/H_n , T_n and v_w . We set $v_w = 1$ for this work. We have already discussed the variation of T_n in the the bottom, right plot of figure 6. In this subsection, we discuss the variation of the other two main portal parameters α and β/H_n , which control the GW spectrum.

In figure 8, we present two plots to show the variation of α (top, left) and β/H_n (top, right) at $T = T_n$ in colors in the $(\lambda_1 + \lambda_4) - M_\Delta$ plane. α (β/H_n) increases (decreases) with increasing $(\lambda_1 + \lambda_4)$ and decreasing M_Δ . These variations have a direct connection with ξ_n . Stronger FOPT corresponds to larger α and lower β/H_n at $T = T_n$. From the discussion in section 2.3.2, it can be found that the magnitude of the peak of the GW intensity is proportional to α and inversely proportional to β/H_n for fixed v_w and T_n (see equations 2.43 and 2.47). These dependencies can be understood from their physical definitions. A larger α corresponds to the more energy transfer from the plasma to the form of GW and a smaller β/H_n implies a longer phase transition period. Thus larger α and small β/H_n enhance the GW intensity. Therefore, one can expect an increase in the GW intensity with ξ_n . As a result, the parameter space with larger effective quartic coupling and smaller triplet-like scalars would produce stronger GW spectrum intensity. In addition to this, as we discuss in section 2.3.2, it can be found that the value of β/H_n is crucial to set the peak frequency range (see equations 2.44 and 2.48) which is also important for the detection purpose at the various future proposed GW experiments.

Therefore, in the left plot of figure 9, we present the variation of α and $\log(\beta/H_n)$ at $T = T_n$. T_n is presented in palette color. The color variation shows that relatively lower T_n corresponds to higher α . On the other hand, β/H_n measures the inverse duration of the phase transition. In some situations, the phase transition takes longer to start, corresponding

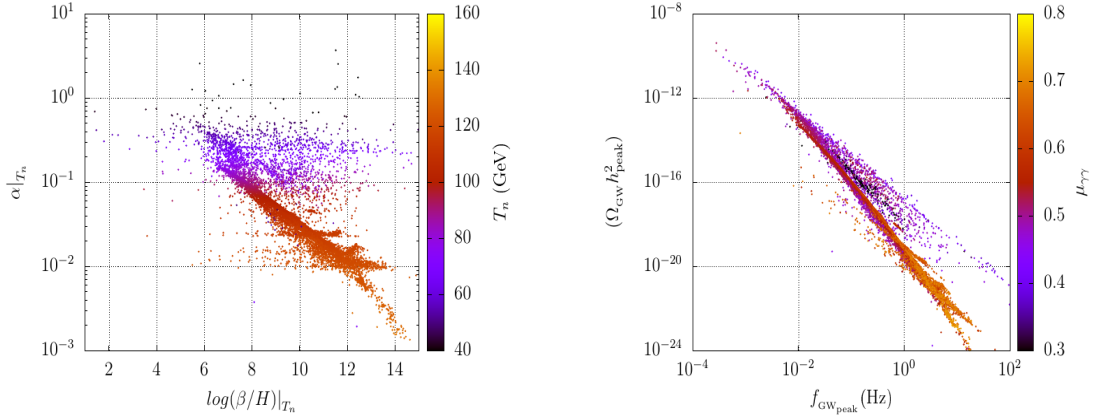


Figure 9. Left: Parameter points of the scan in the $\log(\beta/H_n) - \alpha$ plane with T_n indicating via the palette. Right: Scatter plots of GW peak amplitude ($\Omega_{\text{GW}}h^2$) vs the peak frequency (f_{peak}) in the unit of Hz considering only the contribution coming from the sound waves mechanism. Variation of the signal strength, $\mu_{\gamma\gamma}$, is indicated via the palette.

to relatively lower T_n and a larger gap between T_c and T_n . These scenarios correspond to lower β/H_n . On the contrary, even at relatively low temperatures, the phase transition can happen quickly, corresponding to higher β/H_n . In the plot, the purple points (lower T_n) is across the wide range of β/H_n .

Variations of these portal parameters α , β/H_n , T_n correspond to a wide range of GW peak amplitude and peak frequency. We have already discussed in section 2.3.2 that the sound wave contribution mainly dominates the GW peak amplitude and the peak frequency (see equations 2.44 and 2.43). In the right plot of figure 9, we present the peak amplitude ($\Omega_{\text{GW}}h^2$) vs the peak frequency (f_{peak}) in the unit of Hz considering only the contribution coming from the sound waves mechanism. The future proposed GW experiments have different sensitive regions in the intensity amplitude and the frequency range. Thus, studying the variation of the peak frequency and the peak amplitude of the produced GW is crucial for detecting the spectrum in future proposed experiments. The projected sensitivity of those experiments is presented in figures 11 and 15.

We have already discussed that the regions of parameter space with lower triplet-like scalar masses and correspondingly higher effective quartic couplings can generate larger GW intensity signals. In section 4.2, we show the variation of $\mu_{\gamma\gamma}$ with the various parameters of the model like λ_1, λ_4 . It is expected that at relatively larger effective quartic couplings and light charged triplet-like scalars, $\mu_{\gamma\gamma}$ deviates significantly from 1. Therefore, we present the variation of $\mu_{\gamma\gamma}$ in the palette-color in the bottom, right plot of figure 9. The plot shows that the $\mu_{\gamma\gamma}$ significantly diverges from 1 for larger GW peak amplitudes. We find that most of the region of parameter space of FOPT, which can be probed via the GW experiments, $\mu_{\gamma\gamma}$ is more than 3σ away from the current ATLAS and CMS limits, whereas few points lie within the 3σ limit from the latest observations. Therefore, most of the region of parameter space of this scenario that lies within the sensitivity of various GW detectors are already excluded

Input/Observables	BP1	BP2
λ_1	3.92	3.59
λ_4	-0.989	-0.56
M_Δ	367.7	366.0
v_t (GeV)	3.3×10^{-4}	6.1×10^{-4}
μ_3 (GeV)	-540.9	441.1
λ_{SH}	0.0053	0.0013
λ_{ST}	0.913	0.02
m_{DM}	432.2	420.0
$m_{H^{++}}$ (GeV)	406.4	388.3
m_{H^+} (GeV)	387.5	377.3
$m_{H^0 \sim A^0}$ (GeV)	367.7	365.9
m_h (GeV)	125	125
$\sin \theta_t$ (GeV)	-1.03×10^{-6}	5.69×10^{-7}
Ωh^2	0.008	0.120
$\xi_{DM} \sigma_{DD}^{SI}$ (cm ²)	(9.17)9.31 $\times 10^{-50}$	8.81(8.99) $\times 10^{-50}$
SNR (LISA)	16.7	$\ll 1$

Table 3. Set-I benchmark scenarios with relatively larger (smaller) portal couplings between the triplet (singlet) and the SM Higgs doublet that exhibit a FOEWPT. Shown are the various model input parameters, relevant masses, mixing, DM relic density, DMDDSI cross-section and the signal-to-noise ratio of the produced GW as a result of a FOEWPT in the LISA experiment. The details of the EWPT of these benchmark scenarios are presented in tables 4 and 5.

from the latest precision study of SM-like Higgs boson, particularly $h^0 \rightarrow \gamma\gamma$ decays channel. The region that lies within the 3σ -limit entire region is expected to be tested from the precision study of SM-like Higgs boson in the HL-LHC and/or future colliders. This scenario has an interesting interplay between LHC physics and various GW detectors regarding the possibility of FOPT in the present model. The possibilities of detecting GW at the future proposed GW detectors due to FOPT from the current model would be severely limited in the absence of new physics at the HL-LHC.

In the above discussions, we talk about the phase transition that always happens in the h_d -field direction. We have only discussed how different model parameters from the triplet sector of this model affect the phase transition quantities and the correlations the production of stochastic GW signals and the LHC searches. We find that such correlations excluded most of the regions of the triplet sector that can produce GW as a result of a FOEWPT. On the other hand, the model parameters from the dark sector, particularly λ_{SH} and m_S , can play a crucial role in altering the SM Higgs potential in favour of FOEWPT. Before looking at the influence of the dark sector parameters on the FOPT in the next section, we first provide two benchmark points from the above scan results to illustrate the effect of the triplet-sector parameters on FOEWPT where the dark sector couplings are small. The implications of the dark sector parameters on the FOPT and the relationships between the generated GW and other DM experimental, observational constraints are then discussed in section 5.3.

5.2.2 Benchmark scenarios (Set-I)

In this subsection, we present two benchmark points, BP1 and BP2, in table 3 to illustrate the effect of the triplet-sector parameters on the FOEWPT. In the triplet-sector, v_t is around

BM No	T_i (GeV)	$\{h_d, h_t, h_s\}_{\text{false}}$	Transition type	$\{h_d, h_t, h_s\}_{\text{true}}$ (GeV)	γ_{EW}	
BP1	T_c	76.9	{0, 0, 0}	FO	{230.1, 0, 0}	4.15
	T_n	58.1	{0, 0, 0}	,,	{241.3, 0, 0}	
BP2	T_c	115.0	{0, 0, 0}	,,	{120.9, 0, 0}	1.14
	T_n	114.4	{0, 0, 0}	,,	{130.4, 0, 0}	

Table 4. Phase transition characteristics of the benchmark scenarios BP1 and BP2 presented in table 3. Values of T_c , T_n , the corresponding field values at the false and true phases and the strength of the phase transition, (γ_{EW}), along the $SU(2)$ -direction are presented for each benchmark scenario. ‘FO’ corresponds that the phase transition is first-order type.

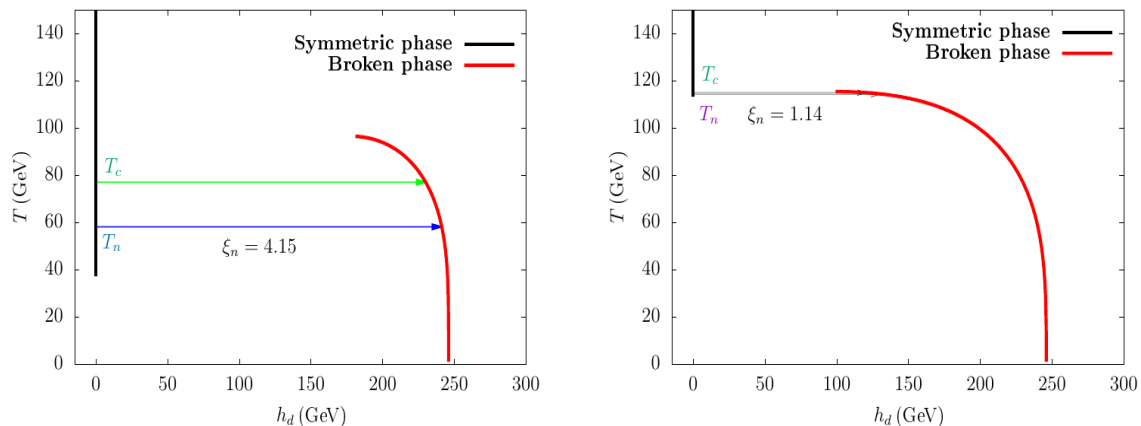


Figure 10. Phase flows in benchmark scenarios BP1 and BP2. Individual color corresponds to a specific minimum of the potential (phase) while each line indicates the evolution of the phase in the h_d -field direction as a function of temperature. The arrows reflect the direction of transition from a false vacuum to a true vacuum, as calculated at T_c and T_n along the h_d -field. See the text for the details.

10^{-4} GeV, $H^{\pm\pm}$ around 400 GeV and for BP1 (BP2) Δm is around 20 GeV (10 GeV). In the dark sectors, $m_s > m_{H^0, A^0, H^\pm, H^{\pm\pm}}$ and the DM annihilation cross-section was large at the early Universe as a result of the opening of the various annihilation channels of the triple-sector. Since $\lambda_{S\Delta}$ is smaller in BP2 than in BP1, the DM relic density is lower in BP1. Lower values of λ_{SH} in BP2 result in a substantially low $\sigma_{\text{DD}}^{\text{SI}}$ compared to BP1. However, relic density scaling sets $\sigma_{\text{DD}}^{\text{SI}}$ value at the same range. For both BP1 and BP2, $\sigma_{\text{DD}}^{\text{SI}}$ is below the neutrino floor. Therefore, it is difficult to probe from the DMDD experiments. However, a significant amount of parameter space left will be probed (corresponds to relatively larger λ_{SH}) from the future DMDD experiments.

The values of T_c and T_n , the strength of the phase transition ξ_n and the field values of the phases at T_c and T_n are presented in Table 4. The calculation of T_c and T_n indicates that these EWPTs are a one-step transition. In BP1, large supercooling is possible since T_n and T_c have a significant difference. This makes the strength of the transition relatively large.

BM No.	T_n (GeV)	α	β/H_n
BP1	58.1	0.325	33.58
BP2	114.4	0.021	26689.5

Table 5. Values of the parameters T_n , α and β/H_n (that control the GW intensity) for the benchmark points BP1 and BP2, presented in table 3.

On the other hand, for BP2, the T_n and T_c are very close to each other. Also, T_n in BP1 is much smaller than in BP2.

We present the evolution of the symmetric and broken phases with temperature in figure 10 for these two benchmark points. Each line (red and black color) shows the field values at a particular minimum as a function of temperature. The black line represents the symmetric phase, whereas the red line indicates the broken phase. In addition, the green arrow indicates that a FOPT may happen in the direction of the arrow since at that temperature and the two phases connected by the arrow are degenerate. The blue color arrow shows the transition direction at the nucleation temperature along which phase transition actually starts. In contrast to BP2, where T_c and T_n are pretty near, BP1 exhibits a significant separation between them, resulting in a stronger phase transition than BP2. The evolution of the broken phase for both benchmark points indicates that the h_d value (red line) finally evolves to 246 GeV at $T = 0$. Thus, the Universe finally evolves to the correct EW minima, i.e., $v = \sqrt{v_d^2 + v_t^2} = 246$ GeV. Note that the contribution of the triplet vev to v is minimal as $v_t \sim 10^{-4}$ GeV at $T = 0$.

Various key parameter values (α , β) pertaining to the GW spectra generated from the FOPTs for these two benchmark scenarios (BP1 and BP2) are presented in table 5. The corresponding GW (frequency) spectra are presented in figure 11 using equations 2.42 to 2.49. For each phase transition process, the contributions from sound waves and turbulence are shown in different colors with broken lines. The GW peak amplitude and the peak frequency are mostly dominated by sound contributions. These GW spectra are further compared with the projected sensitivity of some ground- and space-based GW detectors, viz., LISA [40], ALIA [41], Taiji [42], TianQin [43], aLigo+ [44], SKA [194–196], NANOGrav [197], Big Bang Observer (BBO) [45] and Ultimate(U)-DECIGO [46] in Fig. 11. Note that, a significant amount of supercooling happens in BP1 and the corresponding nucleation temperature is relatively low compared with BP2. This also enhances the α value for BP1 compared with BP2. Also, the nucleation takes a much longer time for BP1 compared with BP2. The β parameter, which indicates the inverse of the duration of the phase transition, is smaller in BP1 than in BP2. Thus, as the FOPT happens much stronger in BP1, the GW spectrum peak is expected to be much larger in BP1 than in BP2. This behaviour can be observed in Fig. 11. Note that the GW intensity obtained for BP1 lies within the sensitivities of LISA, Taiji, ALIA, BBO and UDECIGO, while BP2 lies only within the sensitivity of UDECIGO and marginally touches the BBO sensitivity.

The quantity known as the signal-to-noise ratio (SNR) is used to measure the detection

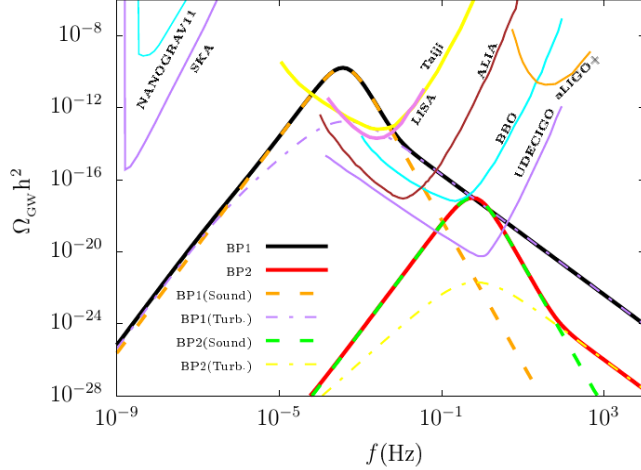


Figure 11. GW energy density spectrum with respect to frequency for the benchmark scenarios BP1 and BP2 illustrated against the experimental sensitivity curves of the future proposed GW detectors such as LISA, SKA, TianQin, Taiji, aLigo+, BBO, NANOGrav, and U-DECIGO. The solid lines indicate the overall GW energy density produced for the specific benchmark scenario, while the broken lines in various colours reflect the individual contributions from sound waves and turbulence. See the text for details.

of the GW signal in different experiments. It is defined as [83]

$$\text{SNR} = \sqrt{\delta \times \mathcal{T} \int_{f_{\min}}^{f_{\max}} df \left[\frac{h^2 \Omega_{\text{GW}}(f)}{h^2 \Omega_{\text{exp}}(f)} \right]^2}, \quad (5.9)$$

where δ corresponds to the number of independent channels for cross-correlated detectors (to determine the stochastic origin of GW). It is 2 for BBO, U-DECIGO and 1 for LISA. The duration of the experimental mission in years is defined by \mathcal{T} . In this work, we consider $\mathcal{T} = 5$. The effective power spectral density of the experiment's strain noise is indicated by $\Omega_{\text{exp}}(f) h^2$. For the detection prospects of these experiments, the SNR values need to cross the threshold value which depends on the configuration details of the experiment. Such as, the recommended threshold number is around 50 for a four-link LISA setup, however, a six-link design allows for a much lower value of around 10 [83]. In this work, we calculate the SNR value only for LISA for these two benchmark points. For BP1, it is 16.7 and for BP2, the SNR value is way below 1. It is expected that the SNR value of BP2 will be substantially lower because its GW signal power spectrum does not fall within the LISA sensitivity curves. However, other experiments like U-DECIGO can detect this type of benchmark scenario.

Note that in both the benchmark scenarios, $\mu_{\gamma\gamma}$ is more than the 3σ away from the latest LHC limits. Thus, as we discussed in the description of the right plot of figure 9, FOEWPT preferred region of parameter space of the triplet sector is mostly excluded from the precision study of the SM Higgs boson di-photon decay modes. Since the FOEWPT is crucial for the EWBG, we investigate its viability in the current model by changing the parameters of the dark sector. In the next section, we will examine such possibilities and

determine the consequences of the dark sector parameters on the FOEWPT as well as the establishing connections between the produced GW and other DM experimental constraints.

5.3 FOPT from the dark sector

In the previous discussions of this article, we set the dark sector portal couplings λ_{SH} and $\lambda_{S\Delta}$ at smaller values and the phase transition along the h_d -field direction is mostly controlled by the triplet sector parameters of the model, i.e., λ_1 , λ_4 and M_Δ . However, larger DM Higgs portal coupling, particularly λ_{SH} as the h_d -field couples with the h_s -field through this portal coupling in the dark sector, can alter the Higgs potential in such a way that FOEWPT occurs. In addition to this, another intriguing possibility is the FOPT in the dark sector. In this case, h_s -field changes from zero vev at high temperature to non-zero vev at the electroweak temperature scale, and then it evolves to zero vev at $T = 0$. Moreover, a two-step FOPT in the scalar potential is even another intriguing possibility. In this category, the h_s -field acquires non-zero vev at a certain temperature in the early Universe through a FOPT and subsequently, relatively at a lower temperature another phase transition occurs where the h_d -field develops a non-zero vev whereas the vev of the h_s -field goes from a non-zero value to a zero value. It is crucial to remember that among these three forms of phase transitions, the one-step phase transition along the h_s -direction is capable of generating GW signal but is ineffective for the electroweak baryogenesis.

To study the phase transition along the h_s -field direction, we first fix the triplet sector parameters the same as the benchmark scenario BP1 and vary the dark sector parameters m_s , λ_{SH} , $\lambda_{S\Delta}$, λ_S and μ_3 . The DM phenomenology due to the variation of these dark matter input parameters for the same triplet-sector input parameters has already been discussed in section 5.1. In figure 12, we present the variation of m_s and λ_{SH} ($\lambda_{S\Delta}$) in the left (right) plot that exhibits FOPT along the h_s -field direction. The strength of the phase transition along the h_s -field direction, i.e., $\xi_s = \frac{\langle h_s \rangle}{T_n}$ where $\langle h_s \rangle$ is the vev of the h_s field at the broken phase at $T = T_n$, is presented via the palette color.

In the left plot, the variation of m_s and λ_{SH} reveals that for the phase transition along the h_s -field direction, λ_{SH} must be large for larger m_s and lower for smaller m_s . The region of parameter space with $m_s \gtrsim 425$ GeV is almost disfavoured for FOPT for $\lambda_{SH} \lesssim 6.0$. On the other hand, the right plot indicates that the phase transition does not have a preferential bias over the choice of $\lambda_{S\Delta}$. Equation 2.19 elucidates such connection between m_s and λ_{SH} . The phase transition along the singlet direction generally prefers relatively low bare mass squared term (μ_s^2) in the potential [198]. Therefore, the parameter space that corresponds to a FOPT along the h_s direction, the maximum possible value of m_s is mainly controlled by the term $\lambda_{SH}v_d^2$ and it is almost independent of $\lambda_{S\Delta}$ as $v_t \ll 1$. The color variation in the left plot reveals that the strength of the phase transition is maximum at the outer edge, corresponding to the parameter space consisting of very small bare mass μ_s .

The variations of these parameters will also have effects on the observables of the dark sector, such as the $\Omega_S h^2$ and $\sigma_{\text{DD}}^{\text{SI}}$, and make these scenarios more sensitive to the various DM experiments. It is therefore anticipated that the production of GW as a result of this type of FOPT in the dark sector will be connected with DM observables. In the following

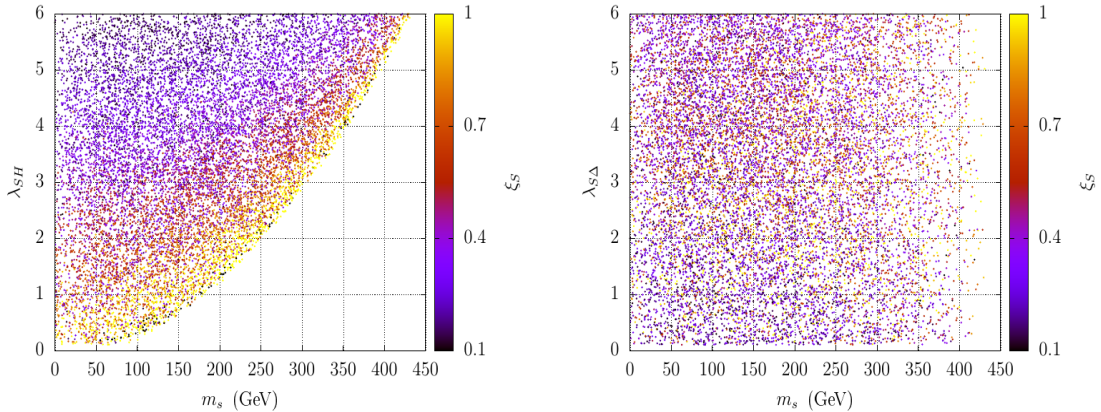


Figure 12. Scatter plots in the $m_S - \lambda_{SH}$ ($m_S - \lambda_{S\Delta}$) plane in the left (right) plot that exhibits FOPT along the h_s -field direction. The variation of the strength of the phase transition ξ_S is shown via the palette.

subsection, we discuss the relationship between the DM phenomenology and FOPT along the h_s -field direction. Note that, in the previous discussion, we found a similar type of correlation between the FOEWPT-induced GW intensity and the precision measurement of the signal strength, $\mu_{\gamma\gamma}$ of the $h^0 \rightarrow \gamma\gamma$ channel at the LHC.

5.3.1 Correlations among the DM observables and a FOPT

In this section, we now turn our attention to the link between the DM observables and FOPT along the h_s -field direction. There is an effect on the various DM observables from the parameter space that exhibits such a phase transition.

The left plot figure 13 is otherwise similar with the left plot of figure 12 but here the points satisfy the Planck experimental constraints on the relic density, i.e., $\Omega_s h^2 \leq 0.120$. The relic density of the singlet scalar field is indicated by the palette color in the plot. Note that, as we described earlier $m_s < h^0$, λ_{SH} mostly controls the $\Omega_s h^2$ whereas for $m_s > h^0$, the μ_3 proportional semi-annihilation process starts to contribute to DM density. $\lambda_{S\Delta}$ starts to contribute significantly when m_s is larger than the triplet-like scalar masses which is in this case around ~ 400 GeV.

The CP -even scalars h^0 and H^0 contribute $\sigma_{\text{DD}}^{\text{SI}}$. It has been discussed in section 2.2 that for smaller values of v_t and $\sin \theta_t$, $\sigma_{\text{DD}}^{\text{SI}}$ mostly depends on the SM-like Higgs boson mediated process and it increases with λ_{SH} . Such enhancement of $\sigma_{\text{DD}}^{\text{SI}}$ with λ_{SH} excludes a significant amount of parameter space from the latest constraints from XENON-1T and PANDA-4T. On the other hand, if the DM mass is larger than the triple-like scalars then larger $\lambda_{S\Delta}$ decreases the relic density without affecting the $\sigma_{\text{DD}}^{\text{SI}}$. With this, at a relatively larger $\lambda_{S\Delta}$ value, the DM could be underabundant. The small scaling factor due to the low relic density actually reduces the effective $\sigma_{\text{DD}}^{\text{SI}}$ value. Such scenarios allow the parameter space with larger λ_{SH} which is otherwise excluded from the latest constraints.

In the right plot of figure 13, we present the points of the left plot that pass the latest $\sigma_{\text{DD}}^{\text{SI}}$ constraint from the XENON-1T and PANDA-4T experiment. The effective $\sigma_{\text{DD}}^{\text{SI}}$ is

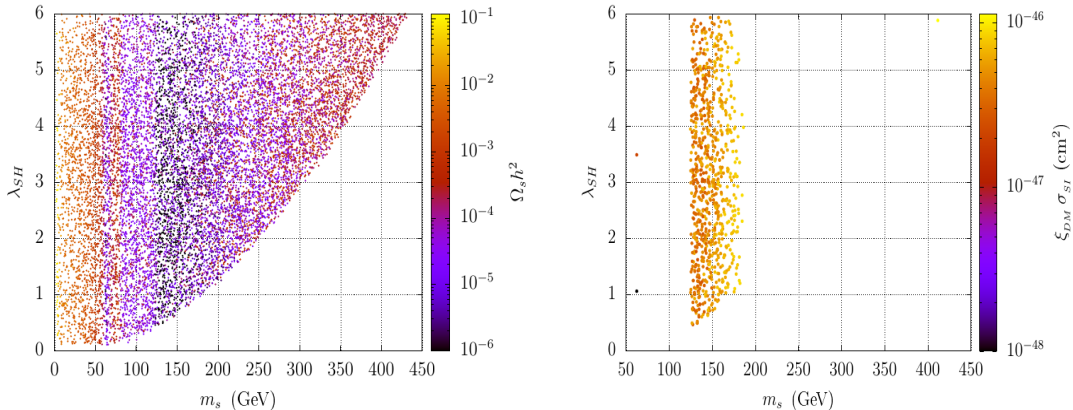


Figure 13. Left: Scatter points that exhibits FOPT along the h_s -field direction and $\Omega_S h^2 < 0.120$ in the $m_S - \lambda_{SH}$ plane. Right: Similar to the scatter spots on the left figure, but comply with the latest DMDDSI experimental limits. The variation of $\Omega_S h^2$ ($\sigma_{\text{DD}}^{\text{SI}}$) is shown via the palette in the left (right) plot.

presented by the palette color. Note that due to the requirement of larger λ_{SH} for the FOPT a significant amount of the parameter space is excluded from the $\sigma_{\text{DD}}^{\text{SI}}$ constraints. Note that for $m_s > h^0$, the μ_3 dependent semi-annihilation process starts to contribute and because of that the relic density drops significantly which helps the effective $\sigma_{\text{DD}}^{\text{SI}}$ rates to remain within the exclusion limit result of a significant downward scaling. Because of that, we find some parameter space for m_s after the SM-like Higgs Boson threshold value. Therefore, it is important to note that the term μ_3 has an important role in the dark sector and the FOPT sector. As it generates the semi-annihilation processes for the DM annihilation, also it can alter the potential shape and generate a barrier between the minima which is necessary for a FOPT. In the scenario for m_s larger than the triplet-like scalars, the term proportional to $\lambda_{S\Delta}$ starts to contribute to the DM annihilation, which can drastically reduce the relic density. However, in this scenario, as the triplet-like scalar masses are relatively large ~ 400 GeV, this effect does not start to occur significantly in the FOPT preferred allowed parameter space as m_s is bounded up to ~ 425 GeV for $\lambda_{SH} \lesssim 6.0$.

The discussion of this subsection points out the strong correlations between the FOPT-favoured parameter space and the DM observables. Such correlations rule out a significant amount of parameter space of having a FOPT along the h_s -field direction. In this case, as we consider the triplet-like scalars a bit heavier, approximately ~ 400 GeV, the contribution from the $\lambda_{S\Delta} h_d^2 h_s^2$ interaction term in the potential on the relic density estimation significantly start to contribute for comparatively higher m_s . In the scenario with relatively smaller triplet-like scalars, the same interaction becomes significant at relatively small m_s that can open up much more allowed parameter points satisfying the latest DMDDSI cross-section limits from the XENON-1T and PANDA-4T experiments due to downward scaling of the underabundant DM. In the next subsection, we choose a benchmark scenario from that category where the triplet-like scalars are relatively low, around ~ 200 GeV, and exhibit FOEWPT in the early

Input/Observables	BP3
λ_1	0.17
λ_4	-0.30
M_Δ	193.2
v_t (GeV)	4.5×10^{-4}
μ_3 (GeV)	-100.8
λ_{SH}	1.2
λ_{ST}	6.9
λ_{ST}	2.17
m_{DM}	252.2
$m_{H^{++}}$ (GeV)	215.3
m_{H^+} (GeV)	204.5
$m_{H^0 \sim A^0}$ (GeV)	193.2
m_h (GeV)	125
$\sin \theta_t$ (GeV)	8.0×10^{-6}
Ωh^2	4.3×10^{-5}
$\xi_{DM} \sigma_{DD}^{SI}$ (cm ²)	7.1×10^{-47}
SNR (LISA)	$\ll 1$

Table 6. Set-II benchmark scenario with relatively smaller (larger) portal couplings between the triplet (singlet) and the SM Higgs doublet that exhibits a two-step EWPT in the early Universe. Similar to table 3, various model input parameters, masses, mixing, DM relic density, DMDDSI cross-section and the signal-to-noise ratio of the produced stochastic GW signal in the LISA experiment are shown. The details of the phase transition are shown in tables 7 and 8.

Universe and discuss the such correlation between the FOPT, production of GW and the DM observables is also discussed.

5.3.2 Benchmark scenario (Set-II)

In this section, we present a benchmark point (BP3) exhibiting a two-step FOPT in the early Universe. We consider a relatively light triplet-like scalar of around 200 GeV and much smaller λ_1 and $|\lambda_4|$ values such that $\mu_{\gamma\gamma}$ is within the 1σ (2σ)-limit of ATLAS (CMS) latest results. Scenarios like this demand larger quartic couplings (particularly λ_{SH}) in the dark sector and smaller DM mass for a FOPT in the early Universe. In the discussion in section 5.2, we consider very low quartic couplings of the dark sector, i.e., much smaller λ_{SH} and $\lambda_{S\Delta}$. This can be seen in BP1 and BP2 in table 6. Because of such consideration, we do not find points with smaller quartic coupling points in the triplet-sector, i.e., parameter points with smaller λ_1 and $|\lambda_4|$, in section 5.2 that can generate a FOEWPT in the early Universe.

Compared to the scenarios discussed in section 5.2, in the BP3 λ_{SH} is relatively large ~ 1.2 , which facilitates successful FOPT in the scalar potential. However, σ_{DD}^{SI} is expected to be much larger as a result of a large coupling. To comply with the latest experimental constraints from XENON-1T and PANDA-4T we consider m_s larger than the triplet-like scalar masses and much larger $\lambda_{S\Delta} \sim 6.9$, such that the $S S^* \rightarrow X Y$; $\{X, Y\} = \{H, A^0, H^\pm, H^{\pm\pm}\}$ annihilation processes open up and contribute significantly to the annihilation cross-section so that DM becomes underabundant. Such a lower relic density corresponds to a much smaller scaling fraction ξ_{DM} which helps the computed σ_{DD}^{SI} rate to comply with the latest experimental stringent limits.

BM No	T_i (GeV)	$\{h_d, h_t, h_s\}_{\text{false}}$	Transition type	$\{h_d, h_t, h_s\}_{\text{true}}$ (GeV)	γ_{EW}	
BP3	T_c	163.2	{0, 0, 0}	FO	{0, 0, 14.8}	1.7
		145.7	{0, 0, 63.6}	,,	{78.9, 0, 0}	
	T_n	163.1	{0, 0, 0}	,,	{0, 0, 15.1}	
		116.3	{0, 0, 86.7}	,,	{197.3, 0, 0}	

Table 7. Phase transition characteristics of the benchmark point BP3 presented in table 6. Values of T_c , T_n , the corresponding field values at the false and true phases and the strength of the phase transition, (γ_{EW}), along the $SU(2)$ -direction are presented. ‘FO’ denotes to FOPT.

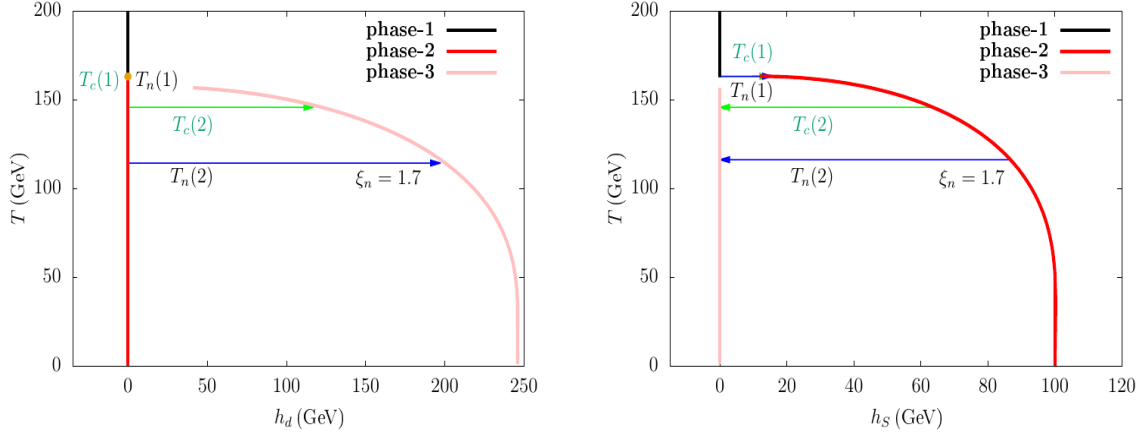


Figure 14. Phase flows in benchmark point BP3. Individual color corresponds to a specific minimum of the potential (phase) while the each line indicates the evolution of the phase in the h_d -field direction in the left and h_s -field direction in the right as a function of temperature. The arrows reflect the direction of transition from a false vacuum to a true vacuum, as calculated at T_c and T_n along the h_d -field, whereas an orange bullet indicates that the corresponding field value does not change much throughout that transition. See the text for the details.

Note that the value of m_S is also crucial for the FOPT and can not be too large. Due to the comparatively smaller triplet-like scalar masses ~ 200 GeV in this benchmark point, we can keep m_S within the range of ~ 250 GeV and also take the benefit of the downward relic density scaling factor on the DMDDSI experimental constraints. This aids in keeping the DMDDSI cross-section of BP3 below the most recent constraints from the XENON-1T and PANDA-4T experiments. In contrast with BP1 and BP2, the phase transition pattern is quite different in BP3. The values of T_c and T_n for the BP3 benchmark scenario are presented in table 7 and it suggests that the transition is a two-step FOPT. The evolution of the field and the various phases with temperature are presented in figure 14. Note that three types of phase exist. ‘phase-I’ denotes the trivial phase, i.e., all the field values are always zero. On the other hand, ‘phase-II’ corresponds to the minimum where only the h_s -field acquires a non-zero vev and other field $vevs$ remain zero. ‘phase-III’ corresponds to that minimum of the potential where only h_d -field obtains a non-zero vev and all other field $vevs$ remain

BM No.	T_n (GeV)	α	β/H_n
BP3	163.1	2.3×10^{-4}	4.8×10^6
	116.3	0.027	312.7

Table 8. Values of the parameters T_n , α and β/H_n (that control the GW intensity) for the benchmark point BP3, shown in table 6.

at zero. In the right and left plots of figure 14, the trivial minimum $\{0, 0, 0\}$ at the high temperature is denoted by the black line (phase-I) where the broken phases in the direction of h_s and h_d are presented in the red color (phase-II) and magenta color (phase-III). These lines correspond to the field values of a particular minimum as a function of temperature. The arrows in green color correspond to the temperature and field values of two phases where they degenerate and a possible FOPT can happen along the direction of the arrow. The phase at the end of the arrow indicates that it has a deeper minimum than the other phase for $T < T_c$. The transitions finally start to occur when a bubble of the true minimum finally successfully nucleates, i.e., at $T = T_n$. The arrows in blue color represent the direction of the FOPT at $T = T_n$ in the field space. The small circle in yellow color represents that a FOPT happens in the scalar potential at that temperature but its field values do not change.

Note that, first, a broken phase $\{0, 0, 14.8\}$ appears only along the h_s -field direction at $T_c = 163.2$ GeV with a possibility of a FOPT. The successful nucleation occurs at $T_n = 163.1$ GeV. It has been shown in the right plot of figure 14. The small difference between T_c and T_n makes the two arrows overlap each other. In the left plot of figure 14, a yellow circle has been shown at $T = 163.1$ GeV as during this FOPT the h_d -field does not acquire any non-zero vev , i.e., EW symmetry remains unbroken. Thus, the first FOPT occurs from $\{h_d = 0, h_t = 0, h_s = 0\} \rightarrow \{h_d = 0, h_t = 0, h_s \neq 0\}$ phase direction. Subsequently, later stage, another minimum form (phase-III), designated by the notation $\{h_d \neq 0, h_t = 0, h_s = 0\}$. At $T = 145.2$ GeV phase-II ($\{0, 0, 63.6\}$) and phase-III ($\{78.9, 0, 0\}$) become degenerate and for $T < 145.2$ GeV phase-III becomes the global minimum of the scalar potential. The corresponding nucleation occurs at $T = 116.3$ GeV. During this transition both h_d - and h_s -fields undergo a change, with the former acquiring a non-zero vev from zero and the latter developing a zero vev from a non-zero vev value. Note that, at $T = 0$, h_d field in the phase-III evolves to the value of 246 GeV and h_s remains at zero in this phase. During these phase transitions, the triplet field always remains very small. Therefore, the system finally evolves to the correct EW minimum. Note that in this benchmark scenario, the minimum phase-II is still present at $T = 0$ where $\langle h_s \rangle \sim 100$ GeV and all other fields $vevs$ are almost zero. But, the global potential minimum of the potential is the phase-III, not the phase-II.

The values of the key parameters (α , β), which are related to the computation of GW spectra generated from the FOPTs for the benchmark scenarios BP3, are presented in table 8. The GW frequency spectrum of BP3 is presented in figure 15 using equations 2.42 to 2.49. Note that the first FOPT along the h_s -field direction happens very quickly (much larger β/H_n value) and also the phase transition is not strong enough which corresponds to a much

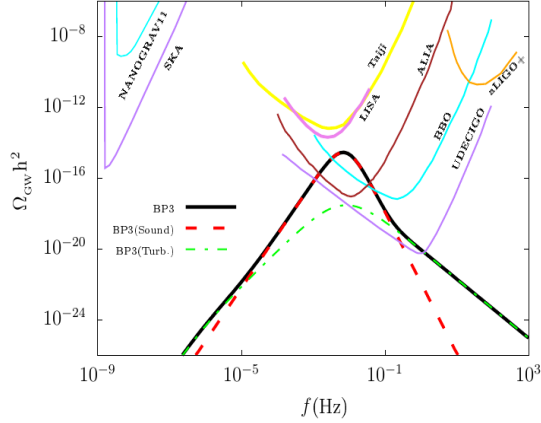


Figure 15. GW energy density spectrum with respect to frequency for the benchmark point BP3 illustrated against the experimental sensitivity curves of the future proposed GW detectors such as LISA, SKA, TianQin, Taiji, aLigo+, BBO, NANOGrav, and U-DECIGO. The black line denotes the total GW energy density whereas the red (green) broken line represents the contributions from sound waves (turbulence). Note that in this benchmark scenario the contribution from the first phase transition along the h_s -field direction does not appear in these plots as its contribution is too small.

lower α value. Thus, the contributions of the first FOPT in the h_s -field direction to the total GW spectrum are very small compared to the ones coming from the second FOPT which happens along the h_d and h_s field directions simultaneously. Therefore, a spectral peak due to the first phase transition in this two-step phase transition does not appear in the plot.

Similar to figure 11, here also each phase transition process, the contributions from sound waves and turbulence are shown in different colors with broken lines. The GW peak amplitude and the peak frequency are mostly dominated by sound contributions. This GW spectrum is further compared with the projected sensitivity of some ground- and space-based GW detectors, viz., LISA, Taiji, TianQin, aLigo+, SKA, NANOGrav, Big Bang Observer (BBO) and Ultimate(U)-DECIGO in Fig. 15. The GW intensity obtained for BP3 lies within the sensitivities of ALIA, BBO and UDECIGO. As expected, the SNR for LISA is very low for detection. Although the experiments like ALIA, BBO and UDECIGO can detect such a GW signal.

Therefore, the FOPT along the singlet-direction permissible parameter space we address in this section is either excluded from the most recent limits from the various DMDD experiments or will be investigated in the near future. The parameter space that is still allowed corresponds to a significantly underabundant DM. It is projected that the HL-LHC will not be able to limit a substantial portion of the parameter space. Focusing on this model, the observation of any signal at future DM and GW experiments but nothing at the HL-LHC would indicate that DM is severely underabundant.

6 Summary and conclusion

In spite of many successes of the SM, it can not explain neutrino masses and the observed baryon asymmetry of the Universe and does not have a DM candidate. In this article, we examine the Z_3 -symmetric singlet scalar extended type-II seesaw model as a potential contender for simultaneously providing solutions to these three shortcomings within a single framework. The type-II seesaw scenario generates small neutrino masses from the vacuum expectation value of the triplet field, and it can permit large neutrino Yukawa couplings via a tiny triplet vacuum expectation value concurrently with a light seesaw scale even below the TeV scale. The complex scalar field, S , of the model can be a stable WIMP-like dark matter particle under the so-called freeze-out mechanism due to the discrete Z_3 -invariance in the dark sector potential. In addition, new interactions among the SM Higgs doublet, the complex triplet and the complex singlet can induce a FOEWPT in the early Universe, which is necessary for the solution of the BAU problem via the EWBG mechanism. Such a FOEWPT can generate stochastic gravitational wave signals that can be detected in future proposed GW detectors. In this work, we investigate the interplay among the production of gravitational waves, the dark matter phenomenology and the LHC physics within this model.

In this article, we first discuss the phenomenology of the scalar DM in the present model in detail. The DM can annihilate mainly in three ways to freeze out at the early Universe and those processes are given by: DM annihilation (a) $S S^* \rightarrow \text{SM SM}$, (b) $S S^* \rightarrow X Y$; $\{X, Y\} = \{H^0, A^0, H^\pm, H^{\pm\pm}\}$ and DM semi-annihilation (c) $S S \rightarrow S U$; $\{U\} = \{h^0, H^0\}$. The DM Higgs portal coupling $\lambda_{SH}(S^*S)(H^\dagger H)$ and $\lambda_{S\Delta}(S^*S)\text{Tr}[\Delta^\dagger\Delta]$ controls the DM-annihilation processes (a) and (b), respectively whereas the DM semi-annihilation processes are initiated via the cubic term $\mu_3(S^3 + S^{*3})$ in the scalar potential. Such semi-annihilation processes are initiated because of the Z_3 -discrete symmetry of the model that settles the singlet as a DM particle. On the other hand, such cubic terms might form a barrier at the tree level of the scalar potential that can become significant for the FOPT. At a fixed m_s , the spin-independent DMDD cross-section mostly depends on the λ_{SH} portal coupling and it is restricted to an upper value from the latest DMDD constraints. In scenario $m_s < m_{h^0}$, the same portal coupling λ_{SH} mostly controls the DM relic density. Such dependencies on λ_{SH} significantly restrict the DM parameter space for $m_s < m_{h^0}$ and only at the resonance region around m_{h^0} is still allowed after complying with DM relic density and the latest DMDD constraints. The cubic interaction based on μ_3 expands the parameter space for $m_s \gtrsim m_{h^0}$. In addition to this, DM and the triplet sector interaction through the portal coupling $\lambda_{S\Delta}$ opens up a wide range of DM allowed region of parameter space if $m_s \gtrsim m_{H^0, A^0, H^\pm, H^{\pm\pm}}$. Therefore, the allowed region of DM parameter space is dependent on the triplet-like scalar masses, which are constrained by the most recent restrictions from the direct searches of the heavy scalar at the LHC. Such phenomena show some correlations between DM phenomenology and the LHC physics.

Despite the fact that such direct searches at the LHC will be unable to restrict the triplet-like scalar masses even at 200 GeV with 3 ab^{-1} data for moderate v_t and reasonably large $\Delta m (> 10 \text{ GeV})$ values, which corresponds to $\lambda_4 < 0$. At this point, we focus on

this part of the parameter space in order to investigate the feasibility of FOPT in the scalar potential at finite temperatures. In order to investigate the effect of the SFOEWPT on the triplet-sector parameters, we fix dark sector parameters at minimal values. The strength of the SFOEWPT along the h_d -field direction increases with the larger $(\lambda_1 + \lambda_4)$ and smaller $m_{H^{\pm\pm}}$. For $\lambda_1 \lesssim 4.0$, $m_{H^{\pm\pm}}$ greater than 420 GeV is disfavored since the triplet becomes decoupled from the SM Higgs potential, rendering an SFOEWPT impossible.

Such FOEWPT can generate stochastic GW in the early Universe from the bubble wall collisions, long-standing sound waves in the plasma and MHD turbulence. We have thoroughly studied the stochastic GW (background) spectra that might carry the imprints of FOPT from new physics beyond the SM. We study the variation of three important quantities (i) related to the energy released during the phase transition ‘ α ’, (ii) the inverse duration of the phase transition ‘ β ’ and (iii) the temperature at which phase transition finally starts to occur ‘ T_n ’ that control the GW spectrum over the parameter space of the triplet-sector. The regions of parameter space with lower triplet-like scalar masses and correspondingly higher effective quartic couplings $(\lambda_1 + \lambda_4)$ can generate larger GW intensity signals that can fall within the projected sensitivity of some ground- and space-based GW detectors, viz., LISA, Taiji, TianQin, BBO and U-DECIGO. We show that the decay rate of $h^0 \rightarrow \gamma\gamma$ is significantly affected by the SFOEWPT-favored region of parameter space, deviating significantly from the SM-predicted value for larger effective quartic couplings and smaller triplet-like scalars. The correlation between the produced GW peak amplitude, peak frequency and the signal strength $\mu_{\gamma\gamma}$ of that decay channel has been pointed out. LHC precision study of SM Higgs di-photon decay channel has already excluded most of the parameter space that can generate stochastic GW signal in the future GW detectors. No new signal at HL-LHC will completely exclude the possibility of FOEWPT caused by the modification of the shape of the SM Higgs potential as a consequence of large interactions with the triplet sector in the present model.

Another intriguing possibility of SFOEWPT in this model can occur due to the new interaction of the complex singlet dark matter and the SM-like Higgs doublet. The singlet scalar is employed in this context to serve dual roles as a dark matter particle and to offer a favourable condition for the electroweak phase transition to be firmly first-order. Such modification in the scalar potential can further generate a possibility of a two-step FOPT, with the first transition happening in the singlet direction and the second in the h_d -field direction. The scenario of FOPT along the singlet direction prefers relatively larger λ_{SH} . By imposing such criteria for the FOPT, we have shown that a significant amount of parameter space is already excluded from the latest constraints on the spin-independent direct detection cross-section from the various DM experiments. Our results show that this model can generate a FOPT in the h_s -field direction, but only for a tiny fraction of the DM relic density observed by the Planck experiment. Having such a low relic density allows the effective $\sigma_{\text{DD}}^{\text{SI}}$ rates to stay below the exclusion limit owing to considering scaling down. Such a situation only starts to be possible for $m_s \gtrsim h^0$ where due to the μ_3 dependent DM semi-annihilation process can significantly contribute to a drop in the relic density. Scaling down is also conceivable for $m_s \gtrsim m_{H^0, A^0, H^\pm, H^{\pm\pm}}$ by increasing $\lambda_{S\Delta}$. On the other hand, significantly larger m_s is disfavoured for the FOPT. Thus, the μ_3 term in the potential plays a unique role since it

still permits a specific region of parameter space that can comply with DMDDSI rates and also because it can generate a barrier in the tree-level potential in favour of FOPT along the h_s -field direction.

The Higgs potential can be modified by these changes in the dark sector parameters in such a manner that a FOPT also takes place in the h_d -field direction, which is crucial for the EWBG. We explore this prospect by analysing a representative scenario where $\mu_{\gamma\gamma}$ remains very close to 1 since the various triplet sectors couplings are fixed at tiny values. We find that such FOPT demands relatively larger λ_{SH} and as a consequence, future DMDD studies will investigate the feasibility of generating GW as a result of a FOPT in this region of parameter space.

In summary, in this article, we systematically study the interplay among DM phenomenology, LHC physics, and the production of gravitational waves from the FOPT around the electroweak scale in the scalar potential. We discuss the correlations between the DM phenomenology and the LHC constraints from the Higgs searches. Then, we focus on the region of parameter space of the triplet sector that can modify the Higgs potential in such a way that it can produce a FOEWPT as a consequence of large interactions with the triplet sector, but which is not constrained by the direct heavy Higgs searches at the LHC. Most of the region that generates FOEWPT is almost excluded, particularly the measurement of the Higgs di-photon decay rate at the LHC. Therefore, such correlation severely limited the possibility of detecting GW at the future proposed GW detectors due to FOEWPT from a certain region of parameter space of the present model. On the other hand, the FOPT along the singlet-direction permissible parameter space that we address in this work is either excluded from the most recent DMDDSI cross-section limits from the various DMDD experiments or will be investigated in the near future. The parameter space that is still allowed corresponds to a significantly underabundant DM. In this case, HL-LHC will not be able to constrain a significant fraction of the parameter space since the signal intensity of the Higgs di-photon decay rate, $\mu_{\gamma\gamma}$, stays near 1. Focusing on this model, observing any signal at future DM and GW experiments but nothing at the HL-LHC would indicate that DM is severely underabundant. The absence of new physics at the HL-LHC and various DM experiments in future would severely limit the prospects of detecting GW at future proposed GW experiments and exclude the possibility of EWBG in the current model.

Acknowledgments

PG would like to acknowledge Indian Association for the Cultivation of Science, Kolkata for the financial support. The work of TG and SR is supported by the funding available from the Department of Atomic Energy (DAE), Government of India for the Regional Centre for Accelerator-based Particle Physics (RECAPP) at Harish-Chandra Research Institute (HRI). SR is also supported by the Infosys award for excellence in research. SR also acknowledge the High-Performance Scientific Computing facility at RECAPP and HRI.

Appendix

A Tree-level tadpole relations

The mass parameters μ_H^2 , μ_Δ^2 and μ are determined via the minimization conditions (the tadpoles) of V_0 of equation 2.28 and are given by

$$\begin{aligned}\mu_H^2 &= \frac{1}{2}(\lambda_1 + \lambda_4)v_t^2 + \lambda_H v_d^2 - \sqrt{2}\mu v_t, \\ \mu_\Delta^2 &= -(\lambda_2 + \lambda_3)v_t^2 - \frac{1}{2}(\lambda_1 + \lambda_4)v_d^2 + \frac{\mu v_d^2}{\sqrt{2}v_t}. \\ \mu &= \frac{v_t}{\sqrt{2}v_d} \frac{-(\lambda_2 + \lambda_3)\sin 2\theta_t v_t^2 - (\lambda_1 + \lambda_4)v_d v_t \cos 2\theta_t + \lambda_H v_d^2 \sin 2\theta_t}{v_d \sin \theta_t \cos \theta_t - 2v_t \cos^2 \theta_t + 2v_t \sin^2 \theta_t}.\end{aligned}\tag{A.1}$$

B Set of UV-finite counterterm coefficients

The various coefficients of the counterterm potential, defined in equation 2.31 are given by,

$$\delta\lambda_{s\Delta} = -\frac{1}{4v_d v_t} DV_{12}, \tag{B.1a}$$

$$\delta\lambda_H = -\frac{1}{8v_d^3} DV_1 - \frac{1}{8v_d^2} DV_{11}, \tag{B.2a}$$

$$\delta\mu_H^2 = -\frac{3}{4v_d} DV_1 + \frac{1}{4} DV_{11} + \frac{v_t}{4v_d} DV_{12}, \tag{B.3a}$$

$$\delta\mu_\Delta^2 = -\frac{3}{4v_t} DV_2 + \frac{1}{4} DV_{22} + \frac{v_d}{4v_t} DV_{12}, \tag{B.4a}$$

$$\delta\lambda_2 = \frac{1}{8v_t^3} DV_2 - \frac{1}{8v_t^2} DV_{22}, \tag{B.5a}$$

$$\delta\lambda_{sH} = -\frac{1}{2v_t^2} DV_{33}. \tag{B.6a}$$

$DV_i = \frac{\partial V_{\text{CW}}}{\partial \phi_i}$ and $DV_{ij} = \frac{\partial^2 V_{\text{CW}}}{\partial \phi_i \partial \phi_j}$ where $\phi_i, \phi_j = \{h_d, h_t, h_s\}$. All the derivatives are taken at the true EW minima, i.e., $h_d = v_d$, $h_t = v_t$ and $h_s = 0$.

C Daisy resummation improved thermal field-dependent masses

From the high-temperature expansion of the thermal one-loop potential V_T (of equation 2.33 for bosons), the daisy coefficients can be found from the following relation:

$$c_{ij} = \frac{1}{T^2} \left. \frac{\partial^2 V_T}{\partial \phi_i \partial \phi_j} \right|_{T^2 \gg m^2}. \tag{C.1}$$

The eigenvalues of the thermally improved mass-squared matrices for the Higgs and the gauge bosons, i.e., $M^2(h_d, h_t, h_s, T) = \text{eigenvalues}[m^2(h_d, h_t, h_s) + \Pi(T^2)]$ where $\Pi(T^2) = c_{ij}T^2$ and

c_{ij} 's are the above described daisy coefficients. The daisy resummation is particularly significant for a FOPT because it affects the all-important cubic term of the potential at a finite temperature. Only the longitudinal modes of the vectors and scalars get thermal mass corrections. Due to gauge symmetry, thermal effects to the transverse modes are suppressed [69]. With these in mind, the various daisy coefficients are as follows [199–201]:

$$c_H = \frac{1}{16}(g_1^2 + 3g_2^2) + \frac{1}{4}y_t^2 + \frac{1}{24}(6\lambda_1 + 3\lambda_4 + 12\lambda_H + 12\lambda_{SH}), \quad (\text{C.2a})$$

$$c_\Delta = \frac{1}{4}(g_1^2 + 2g_2^2) + \frac{1}{12}(2\lambda_1 + 8\lambda_2 + 6\lambda_3 + \lambda_4 + \lambda_{S\Delta}), \quad (\text{C.2b})$$

$$c_S = \frac{1}{12}4\lambda_S + 2\lambda_{SH} + 3\lambda_{S\Delta}. \quad (\text{C.2c})$$

The field-dependent thermally mass-improved mass-squared matrices for the 2×2 , symmetric matrix (\mathcal{M}_H^2) for the CP -even scalars, in the basis $\{h_d, h_t\}$, is given by

$$M_{H_{11}}^2 = \frac{1}{2}(\lambda_1 + \lambda_4)h_t^2 + 3\lambda_H h_d^2 + \frac{1}{2}\lambda_{SH}h_s^2 - \sqrt{2}\mu h_t - \mu_{SH}^2 + c_H T^2, \quad (\text{C.3a})$$

$$M_{H_{22}}^2 = \frac{1}{2}(\lambda_1 + \lambda_4)h_d^2 + 3(\lambda_2 + \lambda_3)h_t^2 + \frac{1}{2}\lambda_{ST}h_s^2 + \mu_\Delta^2 + c_\Delta T^2, \quad (\text{C.3b})$$

$$M_{H_{12}}^2 = M_{H_{21}}^2 = (\lambda_1 + \lambda_4)h_d h_t - \sqrt{2}\mu h_d. \quad (\text{C.3c})$$

The field-dependent thermally mass-improved mass-squared matrices for the 2×2 , symmetric matrix (\mathcal{M}_H^2) for the CP -odd scalars, in the basis $\{a_d, a_t\}$, is given by

$$M_{A_{11}}^2 = \frac{1}{2}(\lambda_1 + \lambda_4)h_t^2 + \lambda_H h_d^2 + \frac{1}{2}\lambda_{SH}h_s^2 + c_H T^2 + \sqrt{2}\mu h_t - \mu_{SH}^2, \quad (\text{C.4a})$$

$$M_{A_{22}}^2 = \frac{1}{2}(\lambda_1 + \lambda_4)h_d^2 + (\lambda_2 + \lambda_3)h_t^2 + \frac{1}{2}\lambda_{ST}h_s^2 + \mu_\Delta^2 + c_\Delta T^2, \quad (\text{C.4b})$$

$$M_{A_{12}}^2 = M_{A_{21}}^2 = -\sqrt{2}\mu h_d. \quad (\text{C.4c})$$

The field-dependent thermally mass-improved mass-squared matrices for the 2×2 , diagonal matrix (\mathcal{M}_H^2) for the dark sector, in the basis $\{h_s, a_s\}$, is given by

$$M_{DM_{11}}^2 = 3\lambda_S h_s^2 + \frac{1}{2}\lambda_{SH}h_d^2 + \frac{1}{2}\lambda_{S\Delta}h_t^2 + \frac{1}{\sqrt{2}}\mu_3 h_s + \mu_S^2 + c_S T^2, \quad (\text{C.5a})$$

$$M_{DM_{22}}^2 = \lambda_S h_s^2 + \frac{1}{2}\lambda_{SH}h_d^2 + \frac{1}{2}\lambda_{S\Delta}h_t^2 - \frac{1}{\sqrt{2}}\mu_3 h_s + \mu_S^2 + c_S T^2, \quad (\text{C.5b})$$

$$M_{DM_{12}}^2 = M_{DM_{21}}^2 = 0. \quad (\text{C.5c})$$

The field-dependent thermally mass-improved mass-squared matrices for the 2×2 , symmetric matrix ($\mathcal{M}_{H^\pm}^2$) for the CP -even singly charged Higgs bosons, in the basis $\{h_d, h_t\}$, is given by

$$M_{H^\pm_{11}}^2 = \frac{1}{2}\lambda_1 h_t^2 + \lambda_H h_d^2 + \frac{1}{2}\lambda_{SH}h_s^2 - \mu_H^2 + c_H T^2, \quad (\text{C.6a})$$

$$M_{H^\pm_{22}}^2 = \frac{1}{2}\lambda_1 h_d^2 + (\lambda_2 + \lambda_3)h_t^2 + \frac{1}{4}\lambda_4 h_d^2 + \frac{1}{2}\lambda_{S\Delta}h_s^2 + \mu_\Delta^2 + c_\Delta T^2, \quad (\text{C.6b})$$

$$M_{H^\pm_{12}}^2 = M_{H^\pm_{21}}^2 = \frac{1}{2\sqrt{2}}\lambda_4 h_d h_t - \mu h_d. \quad (\text{C.6c})$$

The thermally mass-improved field-dependent mass-squared doubly-charged Higgs mass is given by

$$M_{\Delta^{\pm\pm}}^2 = \frac{1}{2}\lambda_1 h_d^2 + \lambda_2 h_t^2 + \frac{1}{2}\lambda_{S\Delta}h_s^2 + \mu_\Delta^2 + c_\Delta T^2, \quad (\text{C.7})$$

In the fermionic sector, we only consider the top quark degrees of freedom and its field-dependent mass is given by

$$m_t = \frac{1}{\sqrt{2}} y_t h_u \quad . \quad (\text{C.8})$$

The field-dependent Daisy resummation improved thermal mass squared of the charged gauge boson (only the longitudinal modes get thermal mass corrections) field W^\pm and the neutral electroweak gauge boson fields W^3 of $SU(2)$ and the B of $U(1)$ group are given by,

$$\begin{aligned} m_{W_T^\pm}^2 &= \frac{1}{4} g_2^2 (h_d^2 + 2h_t^2), \\ m_{W_L^\pm}^2 &= \frac{1}{4} g_2^2 \left(h_d^2 + 2h_t^2 + \frac{5}{2} g_2^2 T^2 \right), \\ m_{W_T^3}^2 &= \frac{1}{4} g_2^2 (h_d^2 + 4h_t^2), \\ m_{B_T}^2 &= \frac{1}{4} g_1^2 (h_d^2 + 4h_t^2), \\ m_{W_T^3 B_T}^2 &= -\frac{1}{4} g_1 g_2 (h_d^2 + 4h_t^2) \\ m_{W_L^3}^2 &= m_{W_T^3}^2 + \frac{5}{2} g_2^2 T^2, \\ m_{B_L}^2 &= m_{B_T}^2 + \frac{17}{6} g_1^2 T^2, \\ m_{W_L^3 B_L}^2 &= m_{W_T^3 B_T}^2 \end{aligned} \quad (\text{C.9})$$

The physical masses of the gauge bosons can be found after diagonalizing the above matrices. Note that the photon field also acquires non-zero mass at finite temperatures. The zero-temperature field-dependent mass relations can be found by putting $T = 0$ in the above mass relations.

D Feynman diagrams for DM annihilation

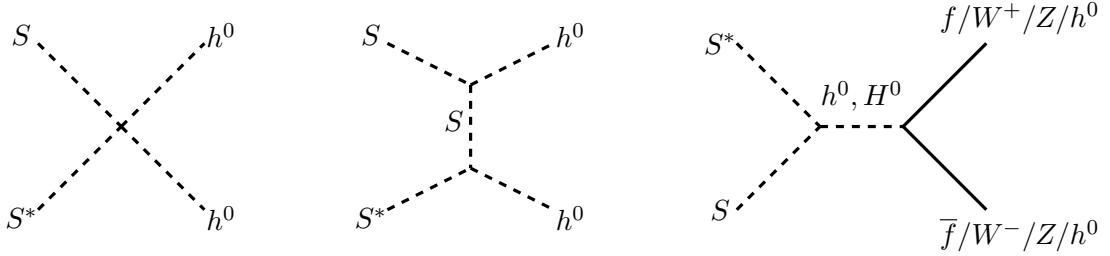


Figure 16. Feynman diagrams for DM annihilate to the SM particles: $S S^* \rightarrow \text{SM SM}$.

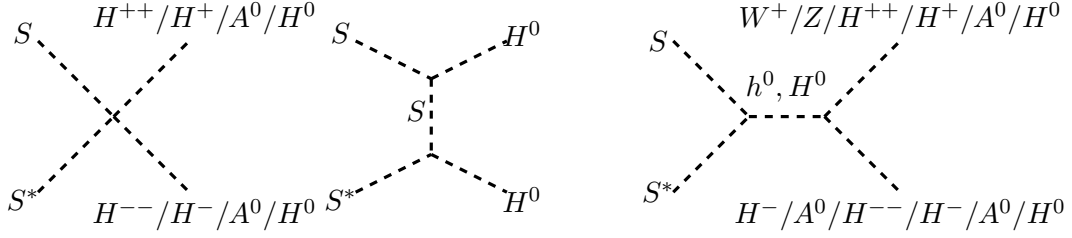


Figure 17. Feynman diagrams for DM annihilate to scalar triplet(s): $S S^* \rightarrow W^+ H^-, Z A^0, XY$. Here $\{X, Y\} = \{H^{\pm\pm}, H^\pm, A^0, H^0\}$.

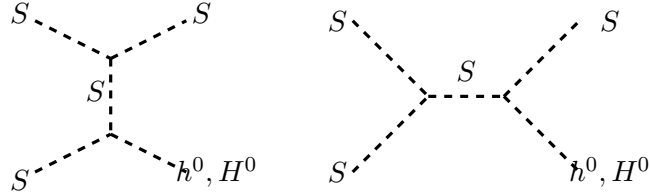


Figure 18. Feynman diagrams for DM semi-annihilation processes: $S S \rightarrow S h^0, S H^0$.

References

- [1] G. Aad *et al.* [ATLAS], Phys. Lett. B **716** (2012), 1-29 doi:10.1016/j.physletb.2012.08.020 [arXiv:1207.7214 [hep-ex]].
- [2] S. Chatrchyan *et al.* [CMS], Phys. Lett. B **716** (2012), 30-61 doi:10.1016/j.physletb.2012.08.021 [arXiv:1207.7235 [hep-ex]].
- [3] A. D. Sakharov, Pisma Zh. Eksp. Teor. Fiz. **5** (1967), 32-35 doi:10.1070/PU1991v034n05ABEH002497
- [4] M. Trodden, Rev. Mod. Phys. **71** (1999), 1463-1500 doi:10.1103/RevModPhys.71.1463 [arXiv:hep-ph/9803479 [hep-ph]].
- [5] G. W. Anderson and L. J. Hall, Phys. Rev. D **45** (1992), 2685-2698 doi:10.1103/PhysRevD.45.2685
- [6] P. Huet and A. E. Nelson, Phys. Rev. D **53** (1996), 4578-4597 doi:10.1103/PhysRevD.53.4578 [arXiv:hep-ph/9506477 [hep-ph]].
- [7] D. E. Morrissey and M. J. Ramsey-Musolf, New J. Phys. **14** (2012), 125003 doi:10.1088/1367-2630/14/12/125003 [arXiv:1206.2942 [hep-ph]].
- [8] W. Hu and S. Dodelson, Ann. Rev. Astron. Astrophys. **40** (2002), 171-216 doi:10.1146/annurev.astro.40.060401.093926 [arXiv:astro-ph/0110414 [astro-ph]].
- [9] D. N. Spergel *et al.* [WMAP], Astrophys. J. Suppl. **170** (2007), 377 doi:10.1086/513700 [arXiv:astro-ph/0603449 [astro-ph]].
- [10] N. Aghanim *et al.* [Planck], Astron. Astrophys. **641** (2020), A6 [erratum: Astron. Astrophys. **652** (2021), C4] doi:10.1051/0004-6361/201833910 [arXiv:1807.06209 [astro-ph.CO]].

- [11] T. Kajita, Rev. Mod. Phys. **88** (2016) no.3, 030501 doi:10.1103/RevModPhys.88.030501
- [12] A. B. McDonald, Rev. Mod. Phys. **88** (2016) no.3, 030502 doi:10.1103/RevModPhys.88.030502
- [13] P. Minkowski, Phys. Lett. B **67** (1977), 421-428 doi:10.1016/0370-2693(77)90435-X
- [14] O. Sawada and A. Sugamoto, KEK-79-18.
- [15] R. N. Mohapatra and G. Senjanovic, Phys. Rev. Lett. **44** (1980), 912 doi:10.1103/PhysRevLett.44.912
- [16] M. Magg and C. Wetterich, Phys. Lett. B **94** (1980), 61-64 doi:10.1016/0370-2693(80)90825-4
- [17] G. Lazarides, Q. Shafi and C. Wetterich, Nucl. Phys. B **181** (1981), 287-300 doi:10.1016/0550-3213(81)90354-0
- [18] D. Ashery, I. Navon, G. Azuelos, H. K. Walter, H. J. Pfeiffer and F. W. Schleputz, Phys. Rev. C **23** (1981), 2173-2185 doi:10.1103/PhysRevC.23.2173
- [19] E. Ma and U. Sarkar, Phys. Rev. Lett. **80** (1998), 5716-5719 doi:10.1103/PhysRevLett.80.5716 [arXiv:hep-ph/9802445 [hep-ph]].
- [20] W. Konetschny and W. Kummer, Phys. Lett. B **70** (1977), 433-435 doi:10.1016/0370-2693(77)90407-5
- [21] J. Schechter and J. W. F. Valle, Phys. Rev. D **22** (1980), 2227 doi:10.1103/PhysRevD.22.2227
- [22] T. P. Cheng and L. F. Li, Phys. Rev. D **22** (1980), 2860 doi:10.1103/PhysRevD.22.2860
- [23] S. M. Bilenky, J. Hosek and S. T. Petcov, Phys. Lett. B **94** (1980), 495-498 doi:10.1016/0370-2693(80)90927-2
- [24] S. Weinberg, Phys. Rev. Lett. **43** (1979), 1566-1570 doi:10.1103/PhysRevLett.43.1566
- [25] R. Zhou, L. Bian and Y. Du, JHEP **08** (2022), 205 doi:10.1007/JHEP08(2022)205 [arXiv:2203.01561 [hep-ph]].
- [26] J. A. Casas, D. G. Cerdeño, J. M. Moreno and J. Quilis, JHEP **05** (2017), 036 doi:10.1007/JHEP05(2017)036 [arXiv:1701.08134 [hep-ph]].
- [27] S. Bhattacharya, P. Ghosh, T. N. Maity and T. S. Ray, JHEP **10** (2017), 088 doi:10.1007/JHEP10(2017)088 [arXiv:1706.04699 [hep-ph]].
- [28] M. Aguilar *et al.* [AMS], Phys. Rev. Lett. **113** (2014), 121102 doi:10.1103/PhysRevLett.113.121102
- [29] G. Ambrosi *et al.* [DAMPE], Nature **552** (2017), 63-66 doi:10.1038/nature24475 [arXiv:1711.10981 [astro-ph.HE]].
- [30] S. Abdollahi *et al.* [Fermi-LAT], Phys. Rev. D **95** (2017) no.8, 082007 doi:10.1103/PhysRevD.95.082007 [arXiv:1704.07195 [astro-ph.HE]].
- [31] A. Yang and H. Sun, [arXiv:2104.01045 [hep-ph]].
- [32] R. Apreda, M. Maggiore, A. Nicolis and A. Riotto, Nucl. Phys. B **631** (2002), 342-368 doi:10.1016/S0550-3213(02)00264-X [arXiv:gr-qc/0107033 [gr-qc]].
- [33] C. Grojean, G. Servant and J. D. Wells, Phys. Rev. D **71** (2005), 036001 doi:10.1103/PhysRevD.71.036001 [arXiv:hep-ph/0407019 [hep-ph]].
- [34] D. J. Weir, Phil. Trans. Roy. Soc. Lond. A **376** (2018) no.2114, 20170126 doi:10.1098/rsta.2017.0126 [arXiv:1705.01783 [hep-ph]].

- [35] C. Caprini, M. Chala, G. C. Dorsch, M. Hindmarsh, S. J. Huber, T. Konstandin, J. Kozaczuk, G. Nardini, J. M. No and K. Rummukainen, *et al.* JCAP **03** (2020), 024 doi:10.1088/1475-7516/2020/03/024 [arXiv:1910.13125 [astro-ph.CO]].
- [36] E. Witten, Phys. Rev. D **30** (1984), 272-285 doi:10.1103/PhysRevD.30.272
- [37] C. J. Hogan, Mon. Not. Roy. Astron. Soc. **218** (1986), 629-636
- [38] J. Ellis, M. Lewicki and J. M. No, JCAP **04** (2019), 003 doi:10.1088/1475-7516/2019/04/003 [arXiv:1809.08242 [hep-ph]].
- [39] T. Alanne, T. Hugle, M. Platscher and K. Schmitz, JHEP **03** (2020), 004 doi:10.1007/JHEP03(2020)004 [arXiv:1909.11356 [hep-ph]].
- [40] P. Amaro-Seoane *et al.* [LISA], [arXiv:1702.00786 [astro-ph.IM]].
- [41] X. Gong, Y. K. Lau, S. Xu, P. Amaro-Seoane, S. Bai, X. Bian, Z. Cao, G. Chen, X. Chen and Y. Ding, *et al.* J. Phys. Conf. Ser. **610** (2015) no.1, 012011 doi:10.1088/1742-6596/610/1/012011 [arXiv:1410.7296 [gr-qc]].
- [42] W. R. Hu and Y. L. Wu, Natl. Sci. Rev. **4** (2017) no.5, 685-686 doi:10.1093/nsr/nwx116
- [43] J. Luo *et al.* [TianQin], Class. Quant. Grav. **33** (2016) no.3, 035010 doi:10.1088/0264-9381/33/3/035010 [arXiv:1512.02076 [astro-ph.IM]].
- [44] G. M. Harry [LIGO Scientific], Class. Quant. Grav. **27** (2010), 084006 doi:10.1088/0264-9381/27/8/084006
- [45] V. Corbin and N. J. Cornish, Class. Quant. Grav. **23** (2006), 2435-2446 doi:10.1088/0264-9381/23/7/014 [arXiv:gr-qc/0512039 [gr-qc]].
- [46] H. Kudoh, A. Taruya, T. Hiramatsu and Y. Himemoto, Phys. Rev. D **73** (2006), 064006 doi:10.1103/PhysRevD.73.064006 [arXiv:gr-qc/0511145 [gr-qc]].
- [47] B. P. Abbott *et al.* [LIGO Scientific and Virgo], Phys. Rev. Lett. **116** (2016) no.6, 061102 doi:10.1103/PhysRevLett.116.061102 [arXiv:1602.03837 [gr-qc]].
- [48] B. P. Abbott *et al.* [LIGO Scientific and Virgo], Phys. Rev. Lett. **119** (2017) no.16, 161101 doi:10.1103/PhysRevLett.119.161101 [arXiv:1710.05832 [gr-qc]].
- [49] B. P. Abbott *et al.* [LIGO Scientific and Virgo], Phys. Rev. X **9** (2019) no.3, 031040 doi:10.1103/PhysRevX.9.031040 [arXiv:1811.12907 [astro-ph.HE]].
- [50] R. Abbott *et al.* [LIGO Scientific and Virgo], Phys. Rev. X **11** (2021), 021053 doi:10.1103/PhysRevX.11.021053 [arXiv:2010.14527 [gr-qc]].
- [51] A. Arhrib, R. Benbrik, M. Chabab, G. Moultaqa, M. C. Peyranere, L. Rahili and J. Ramadan, Phys. Rev. D **84** (2011), 095005 doi:10.1103/PhysRevD.84.095005 [arXiv:1105.1925 [hep-ph]].
- [52] P. Fileviez Perez, T. Han, G. y. Huang, T. Li and K. Wang, Phys. Rev. D **78** (2008), 015018 doi:10.1103/PhysRevD.78.015018 [arXiv:0805.3536 [hep-ph]].
- [53] E. W. Kolb and M. S. Turner, Front. Phys. **69** (1990), 1-547 doi:10.1201/9780429492860
- [54] A. Hektor, A. Hryczuk and K. Kannike, JHEP **03** (2019), 204 doi:10.1007/JHEP03(2019)204 [arXiv:1901.08074 [hep-ph]].
- [55] J. M. Alarcon, L. S. Geng, J. Martin Camalich and J. A. Oller, Phys. Lett. B **730** (2014), 342-346 doi:10.1016/j.physletb.2014.01.065 [arXiv:1209.2870 [hep-ph]].

- [56] E. Aprile *et al.* [XENON], Phys. Rev. Lett. **121** (2018) no.11, 111302
doi:10.1103/PhysRevLett.121.111302 [arXiv:1805.12562 [astro-ph.CO]].
- [57] Y. Meng *et al.* [PandaX-4T], Phys. Rev. Lett. **127** (2021) no.26, 261802
doi:10.1103/PhysRevLett.127.261802 [arXiv:2107.13438 [hep-ex]].
- [58] M. L. Ahnen *et al.* [MAGIC and Fermi-LAT], JCAP **02** (2016), 039
doi:10.1088/1475-7516/2016/02/039 [arXiv:1601.06590 [astro-ph.HE]].
- [59] A. Alloul, N. D. Christensen, C. Degrande, C. Duhr and B. Fuks, Comput. Phys. Commun. **185** (2014), 2250-2300 doi:10.1016/j.cpc.2014.04.012 [arXiv:1310.1921 [hep-ph]].
- [60] G. Belanger, F. Boudjema, A. Pukhov and A. Semenov, Comput. Phys. Commun. **176** (2007), 367-382 doi:10.1016/j.cpc.2006.11.008 [arXiv:hep-ph/0607059 [hep-ph]].
- [61] S. R. Coleman and E. J. Weinberg, Phys. Rev. D **7** (1973), 1888-1910
doi:10.1103/PhysRevD.7.1888
- [62] S. P. Martin, Phys. Rev. D **90** (2014) no.1, 016013 doi:10.1103/PhysRevD.90.016013
[arXiv:1406.2355 [hep-ph]].
- [63] J. Elias-Miro, J. R. Espinosa and T. Konstandin, JHEP **08** (2014), 034
doi:10.1007/JHEP08(2014)034 [arXiv:1406.2652 [hep-ph]].
- [64] S. Baum, M. Carena, N. R. Shah, C. E. M. Wagner and Y. Wang, JHEP **03** (2021), 055
doi:10.1007/JHEP03(2021)055 [arXiv:2009.10743 [hep-ph]].
- [65] A. Chatterjee, A. Datta and S. Roy, JHEP **06** (2022), 108 doi:10.1007/JHEP06(2022)108
[arXiv:2202.12476 [hep-ph]].
- [66] L. Dolan and R. Jackiw, Phys. Rev. D **9** (1974), 3320-3341 doi:10.1103/PhysRevD.9.3320
- [67] S. Weinberg, Phys. Rev. D **9** (1974), 3357-3378 doi:10.1103/PhysRevD.9.3357
- [68] D. A. Kirzhnits and A. D. Linde, Annals Phys. **101** (1976), 195-238
doi:10.1016/0003-4916(76)90279-7
- [69] J. R. Espinosa, M. Quiros and F. Zwirner, Phys. Lett. B **314** (1993), 206-216
doi:10.1016/0370-2693(93)90450-V [arXiv:hep-ph/9212248 [hep-ph]].
- [70] R. R. Parwani, Phys. Rev. D **45** (1992), 4695 [erratum: Phys. Rev. D **48** (1993), 5965]
doi:10.1103/PhysRevD.45.4695 [arXiv:hep-ph/9204216 [hep-ph]].
- [71] N. K. Nielsen, Nucl. Phys. B **101** (1975), 173-188 doi:10.1016/0550-3213(75)90301-6
- [72] R. Fukuda and T. Kugo, Phys. Rev. D **13** (1976), 3469 doi:10.1103/PhysRevD.13.3469
- [73] M. Laine, Phys. Rev. D **51** (1995), 4525-4532 doi:10.1103/PhysRevD.51.4525
[arXiv:hep-ph/9411252 [hep-ph]].
- [74] J. Baacke and S. Junker, Phys. Rev. D **49** (1994), 2055-2073 doi:10.1103/PhysRevD.49.2055
[arXiv:hep-ph/9308310 [hep-ph]].
- [75] J. Baacke and S. Junker, Phys. Rev. D **50** (1994), 4227-4228 doi:10.1103/PhysRevD.50.4227
[arXiv:hep-th/9402078 [hep-th]].
- [76] M. Garny and T. Konstandin, JHEP **07** (2012), 189 doi:10.1007/JHEP07(2012)189
[arXiv:1205.3392 [hep-ph]].

- [77] J. R. Espinosa, M. Garny, T. Konstandin and A. Riotto, *Phys. Rev. D* **95** (2017) no.5, 056004 doi:10.1103/PhysRevD.95.056004 [arXiv:1608.06765 [hep-ph]].
- [78] H. H. Patel and M. J. Ramsey-Musolf, *JHEP* **07** (2011), 029 doi:10.1007/JHEP07(2011)029 [arXiv:1101.4665 [hep-ph]].
- [79] S. Arunasalam and M. J. Ramsey-Musolf, *JHEP* **08** (2022), 138 doi:10.1007/JHEP08(2022)138 [arXiv:2105.07588 [hep-ph]].
- [80] J. Löfgren, M. J. Ramsey-Musolf, P. Schicho and T. V. I. Tenkanen, [arXiv:2112.05472 [hep-ph]].
- [81] M. Laine, M. Meyer and G. Nardini, *Nucl. Phys. B* **920** (2017), 565-600 doi:10.1016/j.nuclphysb.2017.04.023 [arXiv:1702.07479 [hep-ph]].
- [82] B. Allen and J. D. Romano, *Phys. Rev. D* **59** (1999), 102001 doi:10.1103/PhysRevD.59.102001 [arXiv:gr-qc/9710117 [gr-qc]].
- [83] C. Caprini, M. Hindmarsh, S. Huber, T. Konstandin, J. Kozaczuk, G. Nardini, J. M. No, A. Petiteau, P. Schwaller and G. Servant, *et al. JCAP* **04** (2016), 001 doi:10.1088/1475-7516/2016/04/001 [arXiv:1512.06239 [astro-ph.CO]].
- [84] R. G. Cai, Z. Cao, Z. K. Guo, S. J. Wang and T. Yang, *Natl. Sci. Rev.* **4** (2017) no.5, 687-706 doi:10.1093/nsr/nwx029 [arXiv:1703.00187 [gr-qc]].
- [85] C. Caprini and D. G. Figueroa, *Class. Quant. Grav.* **35** (2018) no.16, 163001 doi:10.1088/1361-6382/aac608 [arXiv:1801.04268 [astro-ph.CO]].
- [86] J. D. Romano and N. J. Cornish, *Living Rev. Rel.* **20** (2017) no.1, 2 doi:10.1007/s41114-017-0004-1 [arXiv:1608.06889 [gr-qc]].
- [87] N. Christensen, *Rept. Prog. Phys.* **82** (2019) no.1, 016903 doi:10.1088/1361-6633/aae6b5 [arXiv:1811.08797 [gr-qc]].
- [88] J. R. Espinosa, T. Konstandin, J. M. No and G. Servant, *JCAP* **06** (2010), 028 doi:10.1088/1475-7516/2010/06/028 [arXiv:1004.4187 [hep-ph]].
- [89] M. S. Turner, E. J. Weinberg and L. M. Widrow, *Phys. Rev. D* **46** (1992), 2384-2403 doi:10.1103/PhysRevD.46.2384
- [90] C. L. Wainwright, *Comput. Phys. Commun.* **183** (2012), 2006-2013 doi:10.1016/j.cpc.2012.04.004 [arXiv:1109.4189 [hep-ph]].
- [91] C. W. Chiang and B. Q. Lu, *JHEP* **07** (2020), 082 doi:10.1007/JHEP07(2020)082 [arXiv:1912.12634 [hep-ph]].
- [92] M. Hindmarsh, S. J. Huber, K. Rummukainen and D. J. Weir, *Phys. Rev. D* **92** (2015) no.12, 123009 doi:10.1103/PhysRevD.92.123009 [arXiv:1504.03291 [astro-ph.CO]].
- [93] A. Kosowsky, M. S. Turner and R. Watkins, *Phys. Rev. Lett.* **69** (1992), 2026-2029 doi:10.1103/PhysRevLett.69.2026
- [94] A. Kosowsky, M. S. Turner and R. Watkins, *Phys. Rev. D* **45** (1992), 4514-4535 doi:10.1103/PhysRevD.45.4514
- [95] A. Kosowsky and M. S. Turner, *Phys. Rev. D* **47** (1993), 4372-4391 doi:10.1103/PhysRevD.47.4372 [arXiv:astro-ph/9211004 [astro-ph]].

- [96] D. Bodeker and G. D. Moore, JCAP **05** (2017), 025 doi:10.1088/1475-7516/2017/05/025 [arXiv:1703.08215 [hep-ph]].
- [97] M. Hindmarsh, S. J. Huber, K. Rummukainen and D. J. Weir, Phys. Rev. Lett. **112** (2014), 041301 doi:10.1103/PhysRevLett.112.041301 [arXiv:1304.2433 [hep-ph]].
- [98] J. T. Giblin, Jr. and J. B. Mertens, JHEP **12** (2013), 042 doi:10.1007/JHEP12(2013)042 [arXiv:1310.2948 [hep-th]].
- [99] J. T. Giblin and J. B. Mertens, Phys. Rev. D **90** (2014) no.2, 023532 doi:10.1103/PhysRevD.90.023532 [arXiv:1405.4005 [astro-ph.CO]].
- [100] K. Schmitz, JHEP **01** (2021), 097 doi:10.1007/JHEP01(2021)097 [arXiv:2002.04615 [hep-ph]].
- [101] C. Caprini and R. Durrer, Phys. Rev. D **74** (2006), 063521 doi:10.1103/PhysRevD.74.063521 [arXiv:astro-ph/0603476 [astro-ph]].
- [102] T. Kahniashvili, A. Kosowsky, G. Gogoberidze and Y. Maravin, Phys. Rev. D **78** (2008), 043003 doi:10.1103/PhysRevD.78.043003 [arXiv:0806.0293 [astro-ph]].
- [103] T. Kahniashvili, L. Campanelli, G. Gogoberidze, Y. Maravin and B. Ratra, Phys. Rev. D **78** (2008), 123006 [erratum: Phys. Rev. D **79** (2009), 109901] doi:10.1103/PhysRevD.78.123006 [arXiv:0809.1899 [astro-ph]].
- [104] T. Kahniashvili, L. Kisslinger and T. Stevens, Phys. Rev. D **81** (2010), 023004 doi:10.1103/PhysRevD.81.023004 [arXiv:0905.0643 [astro-ph.CO]].
- [105] C. Caprini, R. Durrer and G. Servant, JCAP **12** (2009), 024 doi:10.1088/1475-7516/2009/12/024 [arXiv:0909.0622 [astro-ph.CO]].
- [106] L. Kisslinger and T. Kahniashvili, Phys. Rev. D **92** (2015) no.4, 043006 doi:10.1103/PhysRevD.92.043006 [arXiv:1505.03680 [astro-ph.CO]].
- [107] T. M. C. Abbott *et al.* [DES], Mon. Not. Roy. Astron. Soc. **480** (2018) no.3, 3879-3888 doi:10.1093/mnras/sty1939 [arXiv:1711.00403 [astro-ph.CO]].
- [108] H. K. Guo, K. Sinha, D. Vagie and G. White, JCAP **01** (2021), 001 doi:10.1088/1475-7516/2021/01/001 [arXiv:2007.08537 [hep-ph]].
- [109] M. B. Hindmarsh, M. Lüben, J. Lumma and M. Pauly, SciPost Phys. Lect. Notes **24** (2021), 1 doi:10.21468/SciPostPhysLectNotes.24 [arXiv:2008.09136 [astro-ph.CO]].
- [110] U. L. Pen and N. Turok, Phys. Rev. Lett. **117** (2016) no.13, 131301 doi:10.1103/PhysRevLett.117.131301 [arXiv:1510.02985 [astro-ph.CO]].
- [111] M. Hindmarsh, S. J. Huber, K. Rummukainen and D. J. Weir, Phys. Rev. D **96** (2017) no.10, 103520 [erratum: Phys. Rev. D **101** (2020) no.8, 089902] doi:10.1103/PhysRevD.96.103520 [arXiv:1704.05871 [astro-ph.CO]].
- [112] M. Hindmarsh and M. Hijazi, JCAP **12** (2019), 062 doi:10.1088/1475-7516/2019/12/062 [arXiv:1909.10040 [astro-ph.CO]].
- [113] J. M. No, Phys. Rev. D **84** (2011), 124025 doi:10.1103/PhysRevD.84.124025 [arXiv:1103.2159 [hep-ph]].
- [114] K. Kannike, Eur. Phys. J. C **72** (2012), 2093 doi:10.1140/epjc/s10052-012-2093-z [arXiv:1205.3781 [hep-ph]].

- [115] G. Belanger, K. Kannike, A. Pukhov and M. Raidal, JCAP **01** (2013), 022 doi:10.1088/1475-7516/2013/01/022 [arXiv:1211.1014 [hep-ph]].
- [116] R. N. Lerner and J. McDonald, Phys. Rev. D **80** (2009), 123507 doi:10.1103/PhysRevD.80.123507 [arXiv:0909.0520 [hep-ph]].
- [117] B. W. Lee, C. Quigg and H. B. Thacker, Phys. Rev. D **16** (1977), 1519 doi:10.1103/PhysRevD.16.1519
- [118] I. Esteban, M. C. Gonzalez-Garcia, M. Maltoni, T. Schwetz and A. Zhou, JHEP **09** (2020), 178 doi:10.1007/JHEP09(2020)178 [arXiv:2007.14792 [hep-ph]].
- [119] N. Aghanim *et al.* [Planck], Astron. Astrophys. **641** (2020), A6 [erratum: Astron. Astrophys. **652** (2021), C4] doi:10.1051/0004-6361/201833910 [arXiv:1807.06209 [astro-ph.CO]].
- [120] P. S. B. Dev, B. Dutta, T. Ghosh, T. Han, H. Qin and Y. Zhang, JHEP **03** (2022), 068 doi:10.1007/JHEP03(2022)068 [arXiv:2109.04490 [hep-ph]].
- [121] M. Kakizaki, Y. Ogura and F. Shima, Phys. Lett. B **566** (2003), 210-216 doi:10.1016/S0370-2693(03)00833-5 [arXiv:hep-ph/0304254 [hep-ph]].
- [122] A. G. Akeroyd, M. Aoki and H. Sugiyama, Phys. Rev. D **79** (2009), 113010 doi:10.1103/PhysRevD.79.113010 [arXiv:0904.3640 [hep-ph]].
- [123] D. N. Dinh, A. Ibarra, E. Molinaro and S. T. Petcov, JHEP **08** (2012), 125 [erratum: JHEP **09** (2013), 023] doi:10.1007/JHEP08(2012)125 [arXiv:1205.4671 [hep-ph]].
- [124] S. Ashanujjaman and K. Ghosh, JHEP **03** (2022), 195 doi:10.1007/JHEP03(2022)195 [arXiv:2108.10952 [hep-ph]].
- [125] U. Bellgardt *et al.* [SINDRUM], Nucl. Phys. B **299** (1988), 1-6 doi:10.1016/0550-3213(88)90462-2
- [126] A. M. Baldini *et al.* [MEG], Eur. Phys. J. C **76** (2016) no.8, 434 doi:10.1140/epjc/s10052-016-4271-x [arXiv:1605.05081 [hep-ex]].
- [127] E. J. Chun, H. M. Lee and P. Sharma, JHEP **11** (2012), 106 doi:10.1007/JHEP11(2012)106 [arXiv:1209.1303 [hep-ph]].
- [128] M. Aoki, S. Kanemura, M. Kikuchi and K. Yagyu, Phys. Rev. D **87** (2013) no.1, 015012 doi:10.1103/PhysRevD.87.015012 [arXiv:1211.6029 [hep-ph]].
- [129] P. A. Zyla *et al.* [Particle Data Group], PTEP **2020** (2020) no.8, 083C01 doi:10.1093/ptep/ptaa104
- [130] K. Huitu, J. Maalampi, A. Pietila and M. Raidal, Nucl. Phys. B **487** (1997), 27-42 doi:10.1016/S0550-3213(97)87466-4 [arXiv:hep-ph/9606311 [hep-ph]].
- [131] S. Chakrabarti, D. Choudhury, R. M. Godbole and B. Mukhopadhyaya, Phys. Lett. B **434** (1998), 347-353 doi:10.1016/S0370-2693(98)00743-6 [arXiv:hep-ph/9804297 [hep-ph]].
- [132] E. J. Chun, K. Y. Lee and S. C. Park, Phys. Lett. B **566** (2003), 142-151 doi:10.1016/S0370-2693(03)00770-6 [arXiv:hep-ph/0304069 [hep-ph]].
- [133] A. G. Akeroyd and M. Aoki, Phys. Rev. D **72** (2005), 035011 doi:10.1103/PhysRevD.72.035011 [arXiv:hep-ph/0506176 [hep-ph]].
- [134] J. Garayoa and T. Schwetz, JHEP **03** (2008), 009 doi:10.1088/1126-6708/2008/03/009 [arXiv:0712.1453 [hep-ph]].

- [135] M. Kadastik, M. Raidal and L. Rebane, *Phys. Rev. D* **77** (2008), 115023
doi:10.1103/PhysRevD.77.115023 [arXiv:0712.3912 [hep-ph]].
- [136] A. G. Akeroyd, M. Aoki and H. Sugiyama, *Phys. Rev. D* **77** (2008), 075010
doi:10.1103/PhysRevD.77.075010 [arXiv:0712.4019 [hep-ph]].
- [137] P. Fileviez Perez, T. Han, G. y. Huang, T. Li and K. Wang, *Phys. Rev. D* **78** (2008), 015018
doi:10.1103/PhysRevD.78.015018 [arXiv:0805.3536 [hep-ph]].
- [138] F. del Aguila and J. A. Aguilar-Saavedra, *Nucl. Phys. B* **813** (2009), 22-90
doi:10.1016/j.nuclphysb.2008.12.029 [arXiv:0808.2468 [hep-ph]].
- [139] A. G. Akeroyd and C. W. Chiang, *Phys. Rev. D* **80** (2009), 113010
doi:10.1103/PhysRevD.80.113010 [arXiv:0909.4419 [hep-ph]].
- [140] A. Melfo, M. Nemevsek, F. Nesti, G. Senjanovic and Y. Zhang, *Phys. Rev. D* **85** (2012), 055018
doi:10.1103/PhysRevD.85.055018 [arXiv:1108.4416 [hep-ph]].
- [141] M. Aoki, S. Kanemura and K. Yagyu, *Phys. Rev. D* **85** (2012), 055007
doi:10.1103/PhysRevD.85.055007 [arXiv:1110.4625 [hep-ph]].
- [142] A. G. Akeroyd and H. Sugiyama, *Phys. Rev. D* **84** (2011), 035010
doi:10.1103/PhysRevD.84.035010 [arXiv:1105.2209 [hep-ph]].
- [143] C. W. Chiang, T. Nomura and K. Tsumura, *Phys. Rev. D* **85** (2012), 095023
doi:10.1103/PhysRevD.85.095023 [arXiv:1202.2014 [hep-ph]].
- [144] A. G. Akeroyd, S. Moretti and H. Sugiyama, *Phys. Rev. D* **85** (2012), 055026
doi:10.1103/PhysRevD.85.055026 [arXiv:1201.5047 [hep-ph]].
- [145] E. J. Chun and P. Sharma, *JHEP* **08** (2012), 162 doi:10.1007/JHEP08(2012)162
[arXiv:1206.6278 [hep-ph]].
- [146] P. S. Bhupal Dev, D. K. Ghosh, N. Okada and I. Saha, *JHEP* **03** (2013), 150 [erratum: *JHEP* **05** (2013), 049] doi:10.1007/JHEP03(2013)150 [arXiv:1301.3453 [hep-ph]].
- [147] S. Banerjee, M. Frank and S. K. Rai, *Phys. Rev. D* **89** (2014) no.7, 075005
doi:10.1103/PhysRevD.89.075005 [arXiv:1312.4249 [hep-ph]].
- [148] F. del Águila and M. Chala, *JHEP* **03** (2014), 027 doi:10.1007/JHEP03(2014)027
[arXiv:1311.1510 [hep-ph]].
- [149] E. J. Chun and P. Sharma, *Phys. Lett. B* **728** (2014), 256-261
doi:10.1016/j.physletb.2013.11.056 [arXiv:1309.6888 [hep-ph]].
- [150] S. Kanemura, K. Yagyu and H. Yokoya, *Phys. Lett. B* **726** (2013), 316-319
doi:10.1016/j.physletb.2013.08.054 [arXiv:1305.2383 [hep-ph]].
- [151] S. Kanemura, M. Kikuchi, K. Yagyu and H. Yokoya, *Phys. Rev. D* **90** (2014) no.11, 115018
doi:10.1103/PhysRevD.90.115018 [arXiv:1407.6547 [hep-ph]].
- [152] S. Kanemura, M. Kikuchi, H. Yokoya and K. Yagyu, *PTEP* **2015** (2015), 051B02
doi:10.1093/ptep/ptv071 [arXiv:1412.7603 [hep-ph]].
- [153] Z. Kang, J. Li, T. Li, Y. Liu and G. Z. Ning, *Eur. Phys. J. C* **75** (2015) no.12, 574
doi:10.1140/epjc/s10052-015-3774-1 [arXiv:1404.5207 [hep-ph]].
- [154] Z. L. Han, R. Ding and Y. Liao, *Phys. Rev. D* **91** (2015), 093006
doi:10.1103/PhysRevD.91.093006 [arXiv:1502.05242 [hep-ph]].

- [155] Z. L. Han, R. Ding and Y. Liao, Phys. Rev. D **92** (2015) no.3, 033014 doi:10.1103/PhysRevD.92.033014 [arXiv:1506.08996 [hep-ph]].
- [156] D. Das and A. Santamaria, Phys. Rev. D **94** (2016) no.1, 015015 doi:10.1103/PhysRevD.94.015015 [arXiv:1604.08099 [hep-ph]].
- [157] K. S. Babu and S. Jana, Phys. Rev. D **95** (2017) no.5, 055020 doi:10.1103/PhysRevD.95.055020 [arXiv:1612.09224 [hep-ph]].
- [158] M. Mitra, S. Niyogi and M. Spannowsky, Phys. Rev. D **95** (2017) no.3, 035042 doi:10.1103/PhysRevD.95.035042 [arXiv:1611.09594 [hep-ph]].
- [159] Y. Cai, T. Han, T. Li and R. Ruiz, Front. in Phys. **6** (2018), 40 doi:10.3389/fphy.2018.00040 [arXiv:1711.02180 [hep-ph]].
- [160] D. K. Ghosh, N. Ghosh, I. Saha and A. Shaw, Phys. Rev. D **97** (2018) no.11, 115022 doi:10.1103/PhysRevD.97.115022 [arXiv:1711.06062 [hep-ph]].
- [161] A. Crivellin, M. Ghezzi, L. Panizzi, G. M. Pruna and A. Signer, Phys. Rev. D **99** (2019) no.3, 035004 doi:10.1103/PhysRevD.99.035004 [arXiv:1807.10224 [hep-ph]].
- [162] Y. Du, A. Dunbrack, M. J. Ramsey-Musolf and J. H. Yu, JHEP **01** (2019), 101 doi:10.1007/JHEP01(2019)101 [arXiv:1810.09450 [hep-ph]].
- [163] P. S. Bhupal Dev and Y. Zhang, JHEP **10** (2018), 199 doi:10.1007/JHEP10(2018)199 [arXiv:1808.00943 [hep-ph]].
- [164] S. Antusch, O. Fischer, A. Hammad and C. Scherb, JHEP **02** (2019), 157 doi:10.1007/JHEP02(2019)157 [arXiv:1811.03476 [hep-ph]].
- [165] A. Aboubrahim and P. Nath, Phys. Rev. D **98** (2018) no.9, 095024 doi:10.1103/PhysRevD.98.095024 [arXiv:1810.12868 [hep-ph]].
- [166] T. B. de Melo, F. S. Queiroz and Y. Villamizar, Int. J. Mod. Phys. A **34** (2019) no.27, 1950157 doi:10.1142/S0217751X19501574 [arXiv:1909.07429 [hep-ph]].
- [167] R. Primulando, J. Julio and P. Uttayarat, JHEP **08** (2019), 024 doi:10.1007/JHEP08(2019)024 [arXiv:1903.02493 [hep-ph]].
- [168] R. Padhan, D. Das, M. Mitra and A. Kumar Nayak, Phys. Rev. D **101** (2020) no.7, 075050 doi:10.1103/PhysRevD.101.075050 [arXiv:1909.10495 [hep-ph]].
- [169] E. J. Chun, S. Khan, S. Mandal, M. Mitra and S. Shil, Phys. Rev. D **101** (2020) no.7, 075008 doi:10.1103/PhysRevD.101.075008 [arXiv:1911.00971 [hep-ph]].
- [170] S. Mandal, O. G. Miranda, G. Sanchez Garcia, J. W. F. Valle and X. J. Xu, Phys. Rev. D **105** (2022) no.9, 095020 doi:10.1103/PhysRevD.105.095020 [arXiv:2203.06362 [hep-ph]].
- [171] B. Dutta, R. Eusebi, Y. Gao, T. Ghosh and T. Kamon, Phys. Rev. D **90** (2014), 055015 doi:10.1103/PhysRevD.90.055015 [arXiv:1404.0685 [hep-ph]].
- [172] G. Aad *et al.* [ATLAS], Eur. Phys. J. C **72** (2012), 2244 doi:10.1140/epjc/s10052-012-2244-2 [arXiv:1210.5070 [hep-ex]].
- [173] S. Chatrchyan *et al.* [CMS], Eur. Phys. J. C **72** (2012), 2189 doi:10.1140/epjc/s10052-012-2189-5 [arXiv:1207.2666 [hep-ex]].
- [174] G. Aad *et al.* [ATLAS], JHEP **03** (2015), 041 doi:10.1007/JHEP03(2015)041 [arXiv:1412.0237 [hep-ex]].

- [175] V. Khachatryan *et al.* [CMS], Phys. Rev. Lett. **114** (2015) no.5, 051801 doi:10.1103/PhysRevLett.114.051801 [arXiv:1410.6315 [hep-ex]].
- [176] [CMS], CMS-PAS-HIG-14-039.
- [177] [CMS], CMS-PAS-HIG-16-036.
- [178] M. Aaboud *et al.* [ATLAS], Eur. Phys. J. C **78** (2018) no.3, 199 doi:10.1140/epjc/s10052-018-5661-z [arXiv:1710.09748 [hep-ex]].
- [179] A. M. Sirunyan *et al.* [CMS], Phys. Rev. Lett. **120** (2018) no.8, 081801 doi:10.1103/PhysRevLett.120.081801 [arXiv:1709.05822 [hep-ex]].
- [180] M. Aaboud *et al.* [ATLAS], Eur. Phys. J. C **79** (2019) no.1, 58 doi:10.1140/epjc/s10052-018-6500-y [arXiv:1808.01899 [hep-ex]].
- [181] G. Aad *et al.* [ATLAS], JHEP **06** (2021), 146 doi:10.1007/JHEP06(2021)146 [arXiv:2101.11961 [hep-ex]].
- [182] T. Ghosh, S. Jana and S. Nandi, Phys. Rev. D **97** (2018) no.11, 115037 doi:10.1103/PhysRevD.97.115037 [arXiv:1802.09251 [hep-ph]].
- [183] H. Baer, A. Mustafayev and X. Tata, Phys. Rev. D **90** (2014) no.11, 115007 doi:10.1103/PhysRevD.90.115007 [arXiv:1409.7058 [hep-ph]].
- [184] B. Dutta, A. Gurrola, W. Johns, T. Kamon, P. Sheldon and K. Sinha, Phys. Rev. D **87** (2013) no.3, 035029 doi:10.1103/PhysRevD.87.035029 [arXiv:1210.0964 [hep-ph]].
- [185] B. Dutta, T. Ghosh, A. Gurrola, W. Johns, T. Kamon, P. Sheldon, K. Sinha, K. Wang and S. Wu, Phys. Rev. D **91** (2015) no.5, 055025 doi:10.1103/PhysRevD.91.055025 [arXiv:1411.6043 [hep-ph]].
- [186] B. Dutta, K. Fantahun, A. Fernando, T. Ghosh, J. Kumar, P. Sandick, P. Stengel and J. W. Walker, Phys. Rev. D **96** (2017) no.7, 075037 doi:10.1103/PhysRevD.96.075037 [arXiv:1706.05339 [hep-ph]].
- [187] G. Aad *et al.* [ATLAS and CMS], JHEP **08** (2016), 045 doi:10.1007/JHEP08(2016)045 [arXiv:1606.02266 [hep-ex]].
- [188] A. M. Sirunyan *et al.* [CMS], Eur. Phys. J. C **79** (2019) no.5, 421 doi:10.1140/epjc/s10052-019-6909-y [arXiv:1809.10733 [hep-ex]].
- [189] A. M. Sirunyan *et al.* [CMS], Phys. Lett. B **793** (2019), 520-551 doi:10.1016/j.physletb.2019.04.025 [arXiv:1809.05937 [hep-ex]].
- [190] A. Arhrib, R. Benbrik, M. Chabab, G. Moultaqa and L. Rahili, JHEP **04** (2012), 136 doi:10.1007/JHEP04(2012)136 [arXiv:1112.5453 [hep-ph]].
- [191] J. F. Gunion, H. E. Haber, G. L. Kane and S. Dawson, Front. Phys. **80** (2000), 1-404 SCIPP-89/13.
- [192] [ATLAS], [arXiv:2207.00348 [hep-ex]].
- [193] A. M. Sirunyan *et al.* [CMS], JHEP **07** (2021), 027 doi:10.1007/JHEP07(2021)027 [arXiv:2103.06956 [hep-ex]].
- [194] C. L. Carilli and S. Rawlings, New Astron. Rev. **48** (2004), 979 doi:10.1016/j.newar.2004.09.001 [arXiv:astro-ph/0409274 [astro-ph]].

- [195] G. Janssen, G. Hobbs, M. McLaughlin, C. Bassa, A. T. Deller, M. Kramer, K. Lee, C. Mingarelli, P. Rosado and S. Sanidas, *et al.* PoS **AASKA14** (2015), 037 doi:10.22323/1.215.0037 [arXiv:1501.00127 [astro-ph.IM]].
- [196] A. Weltman, P. Bull, S. Camera, K. Kelley, H. Padmanabhan, J. Pritchard, A. Raccanelli, S. Riemer-Sørensen, L. Shao and S. Andrianomena, *et al.* Publ. Astron. Soc. Austral. **37** (2020), e002 doi:10.1017/pasa.2019.42 [arXiv:1810.02680 [astro-ph.CO]].
- [197] M. A. McLaughlin, Class. Quant. Grav. **30** (2013), 224008 doi:10.1088/0264-9381/30/22/224008 [arXiv:1310.0758 [astro-ph.IM]].
- [198] K. Ghorbani and P. H. Ghorbani, J. Phys. G **47** (2020) no.1, 015201 doi:10.1088/1361-6471/ab4823 [arXiv:1804.05798 [hep-ph]].
- [199] D. Comelli and J. R. Espinosa, Phys. Rev. D **55** (1997), 6253-6263 doi:10.1103/PhysRevD.55.6253 [arXiv:hep-ph/9606438 [hep-ph]].
- [200] P. Basler and M. Mühlleitner, Comput. Phys. Commun. **237** (2019), 62-85 doi:10.1016/j.cpc.2018.11.006 [arXiv:1803.02846 [hep-ph]].
- [201] M. E. Carrington, Phys. Rev. D **45** (1992), 2933-2944 doi:10.1103/PhysRevD.45.2933